A.D. 1308

unipg

UNIVERSITÀ DEGLI STUDI
DI PERUGIA

Dipartimento di Fisica e Geologia
Corso di Dottorato in Fisica
XXXVIII ciclo

Thesis

Electron/proton discrimination in high-granularity space-borne calorimeters

Candidate
Claudio Brugnoni

Advisor
Doc. Matteo Duranti

Co-Advisor
Doc. Valerio Vagelli

Contents

Introduction

Our galaxy is populated by a broad spectrum of charged and neutral highly energetic particles that we call Cosmic Rays (CRs). The precision measurements of the composition and spectral properties of these particles, that are mostly accelerated in Supernova Remnants and other extreme astrophysical sites, not only provide unique insights on the composition and the properties of our galaxy, but could also unveil unsolved mysteries about the particle nature of Dark Matter and investigate the origin of the matter/antimatter asymmetry observed in the accessible Universe.

The energy distribution of CRs in the energy ranges of relevant interest for fundamental physics ($>$ tens of MeV) covers more than 12 orders of magnitudes. In order to study this broad energetic spectrum of radiation we employ two major families of detection techniques: ground based indirect detection and space-borne direct detection.

The most energetic events, while crossing the atmosphere, interact inelastically with air atoms nuclei and generate extensive cascade showers of secondary particles. Some of these particles eventually reach the ground where they can be observed by particle counters spread over large areas ($\mathcal{O}(\mathrm{km}^2)$). The spatial and temporal distribution of these signals is used to infer the properties of the primary particle. Using this kind of techniques we are able to observe particle up to 10^{20} eV, but we lose a lot of accuracy about the primary particle properties like direction and charge, and we have no way to observe events less energetic that about 10 TeV that are completely absorbed in the upper atmosphere.

In order to avoid the interaction with the atmosphere we need to rely on space-borne experimental facilities. By detecting directly the particles in space, we can precisely measure all the features of the CR components. The drawback of this methodology is due to the stringent requirements in terms of volume, weight, and power budgets of space infrastructures. Since the CR flux decreases with increasing energy, we're not able to collect significant statistics at higher energies.

The current generation of space-borne detectors (AMS-02, DAMPE, CALET) has now taken data for more than a decade and was able to describe with good accuracy the spectra of protons and helium nuclei up to rigidities of hundreds of TV, those of other more abundant nuclei up to the tens of TV scale, and even the spectra of suppressed components like phosphorus or lithium to the TV scale. Also, the spectrum of electrons and positrons was measured by space detectors up to few TeV. Ground detectors are not able to detect particles with a kinetic energy below the PeV scale. For this reason

there's currently a gap in the measured spectra of CR components.

The next generation of space-borne detectors (HERD, ALADInO, AMS-100) will be able to close this gap in the spectra extending to higher energies our capabilities in direct detection. The enabling improvement required to consistently improve the energy reach of space-borne detector while keeping compliance with the requirements in terms of mass and volume of space infrastructures will be the maximization of the gathering power of the experiments. Instruments that will manage to extend their gathering power as much as possible will significantly improve the statistics collected at higher energies. For this reason all the upcoming facilities, both in construction or only proposed, focus on wide field of view detectors and in particular they all rely on 3D imaging segmented calorimeters for both energy measurement and discrimination of electrons from protons. This last task is of fundamental relevance for direct detection of cosmic $e^{\pm}$ because protons represent an extremely more abundant background that cannot be removed by charge measurement. 3D imaging calorimeters offer the potentiality to perform strong e/p discrimination on events incoming from any direction.

This thesis describes the development of a strategy for the discrimination of electrons and positrons from protons and anti-protons that can be employed on such 3D segmented calorimeters. Isotropic shower events impinging on a spherical calorimeter cannot be studied using a conventional layer-based approach, this is way we implemented a Likelihood test based on the 3-dimensional shape of the showers.

The analysis was developed using as a case study the HERD experiment, and it heavily relies on the HERD geometry and the HERD collaboration software tools. The result that we obtain are meant to be a useful benchmark to apply the same approach to any other experiments that employ a similar 3D segmented calorimeter.

The first chapter introduces the basics of cosmic ray physics, from the main properties of the radiation, like composition and spectral shape, to the main accelerator sites, the relation with dark matter, the propagation mechanism and highlights from some recent measurements.

The second chapter moves on to describe the direct CRs detection techniques, comparing spectrometric and calorimetric approaches and describing the design of the upcoming experiments HERD, ALADInO and AMS-100.

The third chapter focuses on calorimetry. It starts from introducing the physics of particle showers, comparing the properties of electromagnetic and hadronic showers, and presents the basic concepts of shower-topology based particle ID and the novel features to be exploited through the analysis of the 3D-imaging isotropic capabilities of next-generation space-born calorimeters.

With the fourth chapter we present the first studies performed, for the PhD work, using the HERD detector design as a benchmark. In particular, we picture the elements necessary to perform a study of the flux of electrons and positrons. For this reason we perform a numerical estimation of the gathering power of the HERD instrument and use expected values of the flux to estimate the uncertainty that the experiment will achieve.

In the fifth chapter we describe in detail the construction of the discrimination parameters that is the main goal of the work. After introducing the statistical concepts we

describe in detail the whole process of simulation of events, reference frame definition, modelling of the statistical moments and probability density function approximation. All data analysis is performed on electrons and on protons in order to obtain statistical description of both the particle species to be used to build the different parameters that we elaborated.

In the sixth chapter we present the results obtained evaluating our discriminators on the simulated data, and we provide some figures of merit to measure the performances that we are able to achieve using these techniques. We also compare our results with the performances of a convolutional neural network that was developed to perform particle identification on our dataset.

Chapter 1

Theoretical Framework

In this first chapter we'll present the fundamental theoretical elements necessary to understand the scientific interest in the study of electrons and positrons in cosmic rays that motivates this work. The chapter is structured in three sections that introduce the reader respectively to cosmic ray physics, to dark matter and finally to the peculiarity of the study of the electrons and positrons cosmic flux.

1.1 Cosmic Rays

Cosmic Rays (CRs) are highly energetic particles originating from a wide variety of astrophysical and cosmological sources. They have been known since the early 20th century, when they were first identified as a form of environmental radioactivity that increases in intensity with altitude. Before the advent of particle accelerators, CRs played a crucial role in the development of particle physics, providing a natural source of high-energy collisions between subatomic particles. Notably, the study of CRs led to the discovery of the positron in 1932 by Anderson, followed by the identification of the muon, pion, and kaon. Until the 1950s, cosmic rays constituted the primary means of conducting experimental particle physics.

Although modern particle physics experiments are now mainly performed at accelerator facilities, which provide precise control over experimental conditions and collision luminosity, CRs physics still offers access to unique experimental conditions that particle colliders cannot yet reproduce. One over all is the availability of extremely energetic events up to 10^{20} eV. CRs also provide information on several hot topics of fundamental physics, such as the search for the origin of DM and of the mechanism behind the observed matter/antimatter asymmetry in the observed Universe in an approach that is complimentary to that pursued at ground-based accelerator facilities. Along with fundamental physics, the study of CRs also contributes on astrophysical goals providing information on the interstellar medium or the galactic magnetic field, but also nuclear physics contributions like constraints on the cross-section of high energy nuclear interactions.

The study of CRs primarily focuses on the measurement of their energy spectrum,

composition, and arrival direction. This information provides crucial insight into their sources' nature, acceleration mechanisms, and propagation processes in the InterStellar Medium (ISM).

The observed energy range of CRs is extremely broad, spanning from a few tens of MeV up to 10^{20} eV, with an intensity of approximately 10^4 events $\mathrm{m}^{-2}\,\mathrm{s}^{-1}\,\mathrm{sr}^{-1}$ above 1 GeV. The differential energy spectrum follows a steep power-law dependence, $E^{-\gamma}$, where the spectral index γ varies across the energy range: it changes from ~ 2.7 to ~ 3 around a few PeV (the first *knee*), then to ~ 3.3 at about 100 PeV (the second *knee*), and finally hardens to ~ 2.5 near a few EeV (the *ankle*), before dropping sharply above several tens of EeV.

Charged CRs consist predominantly of protons (approximately 98%), helium nuclei, and heavier nuclei (about 1%), with a small fraction of electrons (1%), positrons, and antiprotons (less than 1%).

The arrival directions of CRs are mostly isotropic because of the random diffusion by the galactic magnetic field. However, small dipole-like anisotropies of the order of 10^{-4} to 10^{-3} have been detected consistently in the TeV to PeV energy range at large angular scale by Tibet-ASγ[1, 2], ARGO-YBJ[3], Milagro[4], HAWC[5], and IceCube[6]. At even higher energies the observed anisotropy rise to 10^{-1}. Anisotropies in the range of 10^{-2}-10^{-1} have been observed at ultra-high energies ($> 10^{18}$ eV) by the Pierre Auger Observatory[7]. At these energies, the interstellar magnetic field plays the least significant role in bending the cosmic rays. Small angular scale anisotropy structures (angular width $< 60°$) were also observed by MILAGRO[8], ARGO-YBJ[9] and HAWC[10] discovering regions with excesses in the range 10^{-4}-10^{-3}.

The results of the last 20 years of precision measurement on CRs have depicted a more complex image of the galaxy that the one we were expecting in the past. Complex features in energy spectra, anisotropy in the flux excess in anti-matter abundance have pushed to the limits the theoretical models that we used, up to now, to describe the astrophysical object and processes that affect CRs. Theoretical and experimental efforts must now converge in a more complete description and modeling of the galaxy that can allow us to understand if some of the unexpected data that we are observing might lead to new physics or a better understanding of the cosmos.

1.1.1 Composition of Cosmic Rays

The observed abundance of nuclei in cosmic rays (CRs), compared with that measured in the Solar System, is shown in Figure 1.2. The overall similarity in the elemental abundances supports the idea that CRs originate from environments with a composition broadly similar to that of the Solar System. The observed deviations, however, can largely be attributed to the interactions of CRs with the ISM during their propagation.

Elements such as lithium, beryllium, and boron ($Z = 3 - 5$) are produced only as intermediate products in stellar nucleosynthesis and are consequently rare in the Solar System. Their relative abundance in CRs is instead enhanced, as they are generated through spallation processes, in which heavier nuclei fragment upon collision with the interstellar gas.

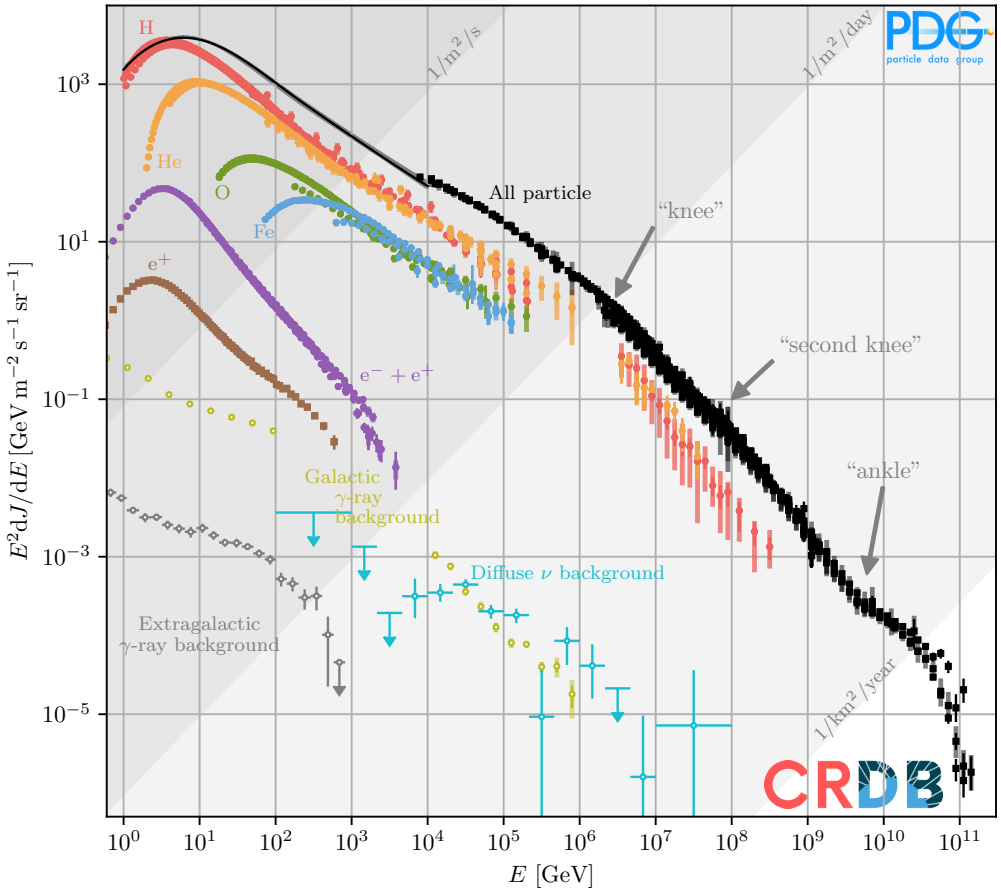

Figure 1.1: The plot shows the full observed spectrum of cosmic rays (CRs). The black dots depict the total intensity of charged and neutral CRs multiplied by kinetic energy squared, while different colors correspond to different components. For energies below 10^4 GeV, the all-particle spectrum is obtained as the sum of spline fits of the most abundant nuclear species. Data for charged CRs come from the Cosmic Ray Database (CRDB) [11].

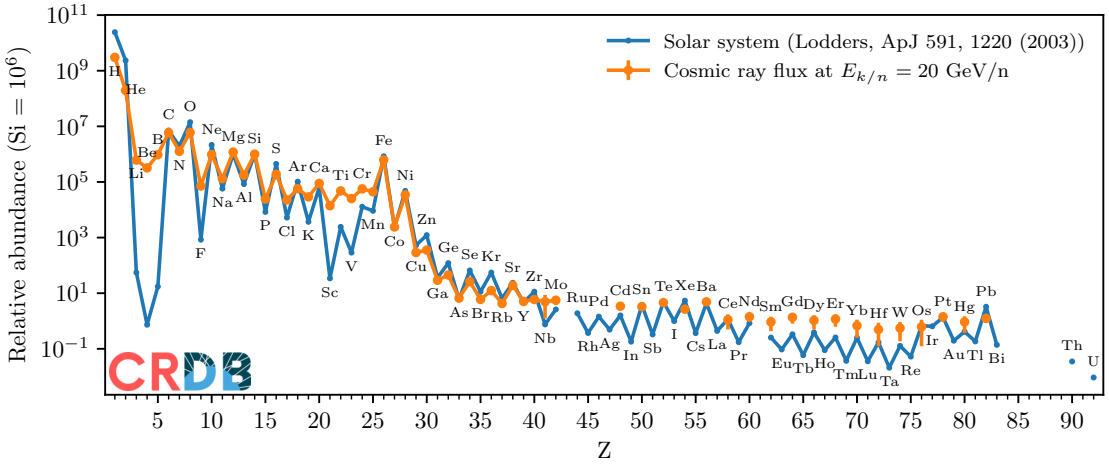

Figure 1.2: Cosmic ray components abundances in the solar system (blue) compared to solar system chemical abundances (orange). For both series the value are normalized to the abundance of Si=1000 [11]. A zig-zag pattern is evident due to the higher binding energy of the elements with an even number of nucleons

Elements with even atomic numbers (Z) are generally more abundant because they possess higher nuclear binding energies, making them less susceptible to fragmentation. This results in a characteristic zig-zag pattern in the elemental abundance distribution, with even-Z elements being more common than their odd-Z neighbors. In CRs, this effect is somewhat reduced: odd-Z elements are replenished through the spallation of more abundant even-Z nuclei, whereas the contribution to even-Z elements from odd-Z species is negligible. As a result, the CR elemental abundance pattern reflects both the nucleo-synthetic origin of the elements and the complex propagation processes that occur in the interstellar medium.

1.1.2 Origin of Cosmic Rays

The primary acceleration sites of Galactic cosmic rays (CRs) are generally identified with SuperNova Remnants (SNRs), which are regions of expanding hot gas produced by SuperNova (SN) explosions. These objects are capable of supplying the required energy input to sustain the observed CR flux in the Galaxy, while also accounting for their measured chemical composition. The acceleration of protons within SNRs has been confirmed through observations of γ-ray emission resulting from π^0 decay[12], and the spectra of both protons and electrons in these environments are actively studied through multi-wavelength observations.

Supernova explosions may arise from two principal mechanisms: thermonuclear explosions in mass-accreting white dwarfs, leading to Type Ia SNe, or the gravitational core collapse of massive stars, producing Type Ib/c and Type II SNe. Particle acceleration within these systems occurs through plasma shock processes, described by second-order

Fermi mechanisms. Physically, the system can be characterized as a blast wave, a shock front formed by the supersonic expansion of a hot gas bubble into the surrounding ISM. The typical observed expansion velocity of an SNR is of the order of 10^4 km/s, while the sound speed in the ISM is only 10-100 km/s. Consequently, a strong shock forms at the outer edge of the expanding shell, acting as a supersonic piston.

The energy released by SNe (Types Ib, Ic, and II) explosions originates from the gravitational collapse of the stellar core, which can be estimated as:

$$E = \frac{GM^2}{R_{NS}} - \frac{GM^2}{R_0} > 10^{51} \text{ erg}, \tag{1.1}$$

where R_0 is the radius of the core before the collapse, M is its mass, while R_{NS} is the radius of the collapsed core (neutron star). Only about 1% of this released energy is converted into the kinetic energy of accelerated particles, while the remainder is emitted as photons (99%) and neutrinos (0.01%). Assuming a supernova explosion occurs approximately every 30 years in our Galaxy, this can be considered effectively continuous compared with the CR escape time of $\sim 10^7$ years. The total power released in such events is approximately 10^{42} erg/s. To reproduce the observed Galactic CR power of $\sim 10^{41}$ erg/s, an energy conversion efficiency from SN explosions to CRs of about 1-10% is required, consistent with current SN acceleration models.

Supernova remnants are thus considered the main accelerators of Galactic CRs up to energies of 10^{15}-10^{17} eV. However, other astrophysical objects, such as pulsars, may also significantly contribute to the observed CR population and have been widely investigated as potential sources of high-energy $e^{\pm}$ pairs.

Pulsars are rapidly rotating neutron stars possessing extremely strong magnetic fields. They represent the compact remnants of supernova explosions, where the thermal pressure generated by nuclear reactions is no longer sufficient to counteract gravitational collapse. A new equilibrium is achieved through neutron degeneracy pressure, as β-decays are suppressed, leading to a stable, dense neutron core.

Following collapse, a young neutron star typically retains a mass of about $1.5\,M_\odot$, concentrated within a radius of only 10-15 km. Conservation of magnetic flux and angular momentum during collapse produces an intense magnetosphere with magnetic field strengths up to $\sim 10^8$ T and angular velocities $\omega \simeq 10^3 - 10^4$ s^{-1}. As illustrated in Figure 1.3, the misalignment between the rotational and magnetic axes generates a time-varying magnetic dipole moment, which radiates electromagnetic energy in close analogy to an oscillating electric dipole. The resulting radiation is highly anisotropic and confined within narrow emission cones, observable as periodic pulses whenever the beam crosses the Earth's line of sight, hence the name *pulsars*.

A conducting plasma surrounds the pulsar. The intense electric field induced by the rotating magnetic field is neutralized by a charge flow along the closed magnetic field lines, generating an electrostatic field sufficient to cancel the total electric field acting on the particles:

$$\vec{E}_{\text{in}} + \underbrace{[(\Omega \times R) \times \vec{B}_{\text{in}}]}_{\text{induced field}} = 0. \tag{1.2}$$

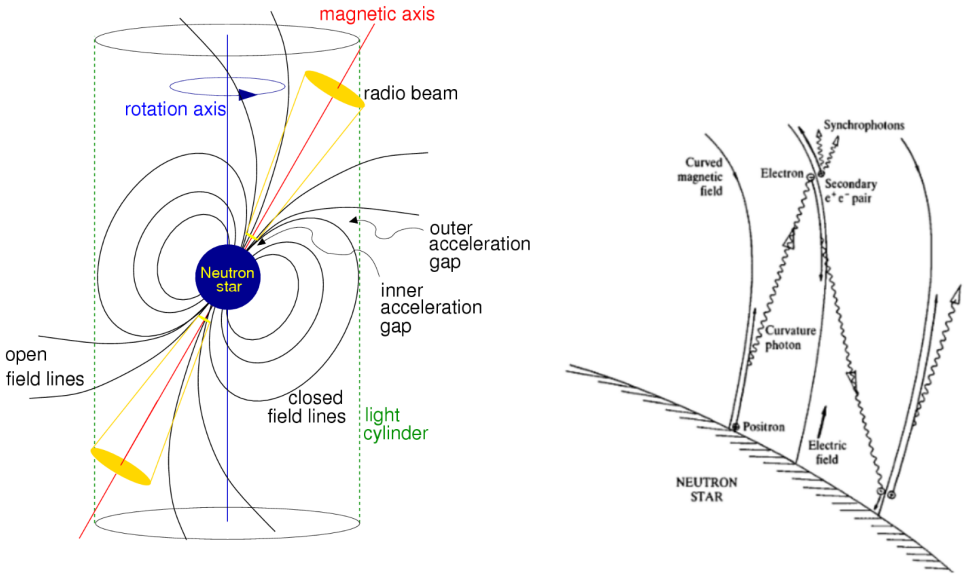

Figure 1.3: The picture on the left is a schematic representation of a tilted pulsar (from [13]). The cylinder centered on the pulsar and aligned to the rotation axis represents the so-called light cylinder at whose radius the co-rotating speed equals the speed of light. Different possible emission regions are shown: the inner gap, where a strong magnetic field prevents photon emission due to production of $e^{\pm}$ pairs and the outer gap, more distant from its surface, where the magnetic field is much smaller and could allow high energy photon emissions. On the right, a schematic view of a cascade generation in the pulsars magnetic field causing photon and $e^{\pm}$ emission/acceleration. (Figure from [14].)

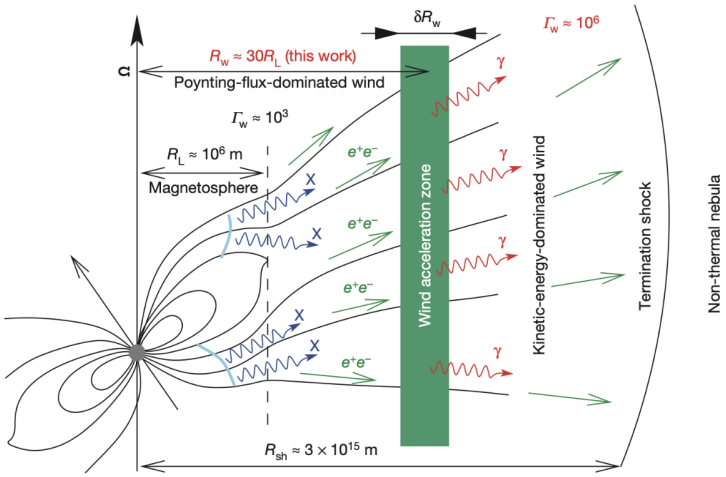

Figure 1.4: Schematic representation of the CRAB pulsar and its environment, highlighting the $e^{\pm}$ and γ production and acceleration processes [17]. Starting from the neutron star, at the radius of the light-cylinder, R_L, particles escape along the open field lines with a wind Lorentz factor $\Gamma_w \sim 10^3$. In the following region, up to $\sim 30R_L$ there is no significant acceleration, up to the wind acceleration zone where $\Gamma_w \sim 10^4$. The termination of the wind with a reverse shock at R_{sh} gives the final boost to the $e^{\pm}$.

At the so-called light-cylinder radius, R_L, where the co-rotation velocity reaches the speed of light, particles can escape the magnetosphere along the open field lines near the magnetic poles (see Figures 1.3 and 1.4). Electrons propagating away from the pulsar emit curvature radiation, and the resulting high-energy photons generate a flux of $e^{\pm}$ pairs (Figure 1.3, right). The surrounding pulsar wind nebula (PWN) is a region of hot, magnetized plasma that temporarily confines the particles before they escape into the interstellar medium, with typical confinement times of order 10^4 years [15, 16]. During this period, particles can undergo additional acceleration before being released.

Figure 1.4 provides a schematic view of a typical pulsar environment, from the magnetosphere to the termination shock. The $e^{\pm}$ pulsar wind interacts with the expanding SNR ejecta, producing both forward and reverse shocks. At the termination shock, part of the wind's bulk kinetic energy is converted into the acceleration of $e^{\pm}$ pairs, which subsequently emit radiation across a wide spectral range, from radio waves to TeV γ-rays, via synchrotron and inverse Compton processes.

1.1.3 Propagation of Cosmic Rays

Once accelerated, CRs propagate through the ISM, undergoing a complex set of processes that shape their observed energy spectra, composition, and angular distribution. The transport of CRs is governed by diffusion in the turbulent Galactic magnetic field, energy losses due to various interactions, and processes such as convection and reacceleration. A

detailed understanding of these mechanisms is essential for interpreting CR measurements and for constraining both source properties and the conditions of the ISM in order to clearly identify any variation of the flux from the expected one and explore any hypothesis of new physics.

The motion of charged CR particles in the Galaxy is primarily influenced by the Galactic magnetic field, whose mean strength is approximately a few µG. Because CRs are charged, they experience the Lorentz force and thus spiral around magnetic field lines with a characteristic Larmor radius given by:

$$r_{\mathrm{L}} = \frac{pc}{ZeB}, \tag{1.3}$$

where p is the particle momentum, Z its charge number, and B the local magnetic field strength. For typical Galactic values, this radius is much smaller than the characteristic size of the Galaxy, implying that CRs are effectively trapped and their propagation can be described as a diffusive process.

The common model used for the description of the CRs propagation in the galactic environment is based on diffusive propagation described by a Fokker-Planck type equation [18]:

$$\begin{aligned}\frac{\partial \psi_i(\vec{r},p,t)}{\partial t} &= Q_i^{\mathrm{tot}}(\vec{r},p,t) \\ &+ \vec{\nabla}\cdot\left(D_{xx}\vec{\nabla}\psi_i - \vec{V}\psi_i\right) \\ &+ \frac{\partial}{\partial p}p^2 D_{pp}\frac{\partial}{\partial p}\frac{1}{p^2}\psi_i - \frac{\partial}{\partial p}\left(\dot{p}\psi_i - \frac{p}{3}(\vec{\nabla}\cdot\vec{V})\psi_i\right) \\ &- \frac{\psi_i}{\tau_{if}} - \frac{\psi_i}{\tau_{ir}}\end{aligned} \tag{1.4}$$

where $\psi_i(\vec{r},p,t)$ represents the density per momentum units p at spacetime coordinates $(\vec{r},t)$ of a given species i.

In the first line of Eq. 1.4, the source term, $Q^{tot}(\vec{r},p,t)$, represents not only the production at astrophysical sources but also the contribution of other species either due to interactions with the ISM or their radiative decay:

$$Q_i^{tot}(\vec{r},p,t) = s_i(\vec{r},p,t) + n\sum_{j\neq i}\nu_j\sigma_{ji}\Psi_j + \sum_{j\neq i}\frac{\Psi_j}{\tau_{rji}} \tag{1.5}$$

The spatial distribution of CRs sources s_i is generally assumed to be correlated with the density of known pulsars or SNRs, with an energy injection spectrum described as a power law spectrum $\partial s/\partial p \propto p^{-\gamma}$.

The second term in Eq. 1.5 represents the contribution to species i from fragmentation of the other species j in the interaction with a density n of ISM particles. v_j and σ_{ji} represent the velocity and the fragmentation cross-section of the source particle j respectively. The last term in Eq. 1.5 represents the contribution to species i due to the decay of the other unstable species j with τ_{rji} that refers to the characteristic decay time.

The second line of Eq. 1.4 describes the spatial transport of CRs, being D_{xx} the spatial diffusion tensor and $\vec{V}$ the convection velocity, strictly related to the structure of the galactic magnetic field. The galactic magnetic field can be decomposed in a regular component, which follows the distribution of the arms of the Galaxy, and a turbulent component in the form of perturbations of the regular field. The diffusive process is due to the resonant scattering of charged cosmic rays with the random small fluctuations $\delta(B) \ll B$ (with $B \sim 6$ µG in our Galaxy [19]). Typical values of the diffusion coefficient found from fitting to CRs data are $D_{xx} \sim (3-5) \times 10^{28}$ cm^2 s^{-1} at energy ~ 1 GeV/n. In several empirical models, the diffusion coefficient varies with the magnetic rigidity as $D_{xx} \propto R^{\alpha}$, due to the turbulent nature of the perturbations. Strong fluctuations of the galactic magnetic field on large scales $L \sim 100$ pc, where the strength of the random field is several times higher than the average field strength, lead to the isotropization of global CRs diffusion in the Galaxy.

Although the most frequently considered mode of CRs transport is diffusion, the existence of galactic winds in many galaxies suggests that convective transport may be important [20]. Those winds are due to the escape of cosmic rays from the bulk of the Galaxy to its halo leading to a gradient in the cosmic ray pressure that acts as a force on the background plasma, in the direction opposite to the gravitational pull. If this force is large enough to win against gravity, a wind can be launched that removes gas from the Galaxy, thereby regulating several physical processes, including star formation [21]. The galactic winds are composed of a stream of charged particle moving out of the Galaxy bulk, with velocities that grow linearly with the distance from the galactic plane up to hundreds of km/s. The coupling to such a stream does not only induce a movement towards the external regions of the Galaxy, but it also induces adiabatic energy losses as the wind speed increases.

The third line of Eq. 1.4 describes energy losses and gains. In addition to the spatial diffusion, the scattering process of the charged CRs particles through the magnetic field irregularities leads to a stochastic acceleration, known as re-acceleration. This process is described by a diffusion in momentum space with a coefficient $D_{pp} \propto |\vec{V}|2/D_{xx}$, where the Alfvén velocity $\vec{V}$ is the characteristic velocity of the fluctuation propagation in the magnetic field. The $\dot{p}$ term is the momentum gain or loss rate due to interactions in the ISM. Nuclei mainly lose energy by ionization while synchrotron radiation and inverse Compton scattering dominate the energy loss of electrons and positrons, drastically changing their propagation as the energy increase.

Particle losses due to fragmentation and radioactive decay are described in the fourth line of Eq. 1.4, where τ_{ir} represents the characteristic decay time. The fragmentation term is related to the interaction probability with the ISM particle, i.e. is $\tau_{if} = 1/nv_i\sigma_i$ being n the ISM particle density, v_i the particle velocity and σ_i the cross-section.

Equation 1.4 is highly non-linear and depends both on a detailed description of particle interactions (e.g. nuclear cross-sections) and of the galaxy structure (e.g. diffusion tensors). Simplified steady state models, as the Leaky Box Model (LBM, [22]), have been used to describe CRs propagation with a reduced number of parameters and underline some of the propagation features.

In the Leaky Box Model, equation 1.4 is approached in a steady state solution ($\partial\psi/\partial = 0$). The Galaxy is the box where CRs are free to propagate in a volume with homogeneous distribution of matter and radiation. Particles leak out of the Galaxy with a characteristic escape time, $\tau_{\rm esc}$, the rate of escape being proportional to the number of particles itself and to the constant spatial diffusion coefficient $\tau_{\rm esc} \propto D^{-1}$. Second line of 1.4 simply becomes:

$$\vec{\nabla} \cdot \left(D_{xx} \vec{\nabla}\psi - \vec{V}\psi \right) = -\frac{\psi}{\tau_{\rm esc}} \tag{1.6}$$

and in the third line, ignoring all contributions due to magnetic field irregularities the only surviving term is related to ionization and radiation losses $\partial(\dot{p}\psi)/\partial p$. Under the LBM assumptions Equation 1.4 in the steady state condition leads to:

$$\bar{q} - \frac{\psi_{\rm esc}}{\tau_{\rm esc}} - \frac{\partial}{\partial p}\left(\dot{p}\,\psi\right) - \frac{\psi}{\tau_f} - \frac{\psi}{\tau_r} = 0 \tag{1.7}$$

where $\bar{q}$ is the time averaged source term. The LBM thus allows to describe the measured flux in terms of few astrophysical parameters, namely the escape time, the abundance at source and the mean matter density.

Historically this has been useful to describe the secondary to primary CRs flux measurements, giving an insight on the average amount of matter crossed by the CRs in their propagation and their characteristic residence times in the Galaxy. However, in the last decades, the number of experimental measurements of CRs species gradually increased, new results have been available in wider energy ranges and with higher and higher accuracy. Simplified models as LBM cannot describe coherently all the observed features and, thanks also to the increasing computing power availability, numerical approaches, as USINE [23], GALPROP [24] or DRAGON [25], replaced analytical solutions introducing many more details in the overall description. While the new experimental data push the theoretical models into taking into account more complex phenomena, the new complexity of models require experiments to outline with more accuracy the peculiarity of CRs spectra. A precise description of the knee region or of the most energetic end of the rarest components' spectra became fundamental to restrain the least known parameters of the acceleration and propagation of CRs.

1.1.4 Electrons and positrons propagation

When applying the general propagation equation (Eq. 1.4) to electrons and positrons, the first key aspect to consider is the nature of their source term. In the standard astrophysical scenario, electrons are primarily produced in SNRs alongside other CR species, whereas secondary positrons and electrons arise mainly from interactions of CR nuclei with the ISM. However, recent high-precision measurements of the $e^{\pm}$ fluxes have prompted the exploration of additional sources, such as dark matter annihilation or nearby pulsars, to account for observed excesses.

The propagation of $e^{\pm}$ in the ISM differs significantly from that of hadrons, as their comparatively small mass makes them highly susceptible to energy losses through synchrotron radiation and Inverse Compton (IC) scattering. These processes dominate their transport and largely determine the observable $e^{\pm}$ spectra at Earth.

Synchrotron radiation arises from relativistic $e^{\pm}$ gyrating around Galactic magnetic field lines. For a particle of mass m, velocity β, and Lorentz factor γ, the radiated power (in the Larmor approximation) is given by:

$$\frac{dE}{dt} = \frac{4}{3}\sigma_T \beta^2 \gamma^2 \varepsilon_B \propto m^{-4}, \tag{1.8}$$

where $\sigma_T = 6.65 \times 10^{-25}$ cm^2 is the Thomson cross-section and ε_B represents the magnetic field energy density. Because the proton-to-electron mass ratio is $m_p/m_e \simeq 2000$, synchrotron emission from protons is strongly suppressed compared to that from electrons. The emitted radiation spectrum peaks at the so-called critical synchrotron frequency, $\omega_s = \gamma^3 \omega_c$, where ω_c is the cyclotron angular frequency. Observations of synchrotron radiation in the radio and microwave bands therefore provide indirect but powerful constraints on CR $e^{\pm}$ populations across a wide energy range, from below 1 GeV to several hundred GeV.

Inverse Compton scattering occurs when relativistic $e^{\pm}$ transfer energy to low-energy photons, boosting them to X-ray or γ-ray energies. The target photons belong to the interstellar radiation field (ISRF), which comprises starlight, dust-emitted infrared radiation, and the cosmic microwave background (CMB). The energy-loss rate due to IC scattering has the same formal dependence as for synchrotron radiation:

$$\frac{dE}{dt} = \frac{4}{3}\sigma_T \beta^2 \gamma^2 \varepsilon_\gamma, \tag{1.9}$$

where ε_γ is the energy density of the target photon field. IC-produced photons constitute a major component of the diffuse Galactic γ-ray emission and serve as tracers of both the ISRF distribution and the spatial density of CR $e^{\pm}$.

Above $\sim$1 GeV, the evolution of the $e^{\pm}$ energy spectra is dominated by these radiative losses, as illustrated in Figure 1.5. Unlike nuclei, which can propagate over large distances, high-energy electrons and positrons rapidly lose energy through synchrotron and IC processes, resulting in much shorter effective propagation lengths. Consequently, the typical distance from which an electron of a given energy can reach the Earth decreases as the energy increases.

For electrons and positrons, the transport equation (Eq. 1.5) can be adapted as:

$$\frac{\partial \psi_{e^\pm}(\vec{r}, E, t)}{\partial t} = Q^{\mathrm{tot}}(\vec{r}, E, t) + D(E)\nabla^2 \psi_{e^\pm} - \frac{\partial}{\partial E}\left[b(E)\psi_{e^\pm}\right], \tag{1.10}$$

where $b(E) = dE/dt$ encapsulates the total energy-loss rate, including both synchrotron and IC contributions. The solutions to this equation show that the effective propagation length of CR $e^{\pm}$ with energies above $\sim$1 GeV is considerably smaller than the Galactic halo height. Therefore, high-energy electrons and positrons detected at Earth must originate from nearby Galactic sources.

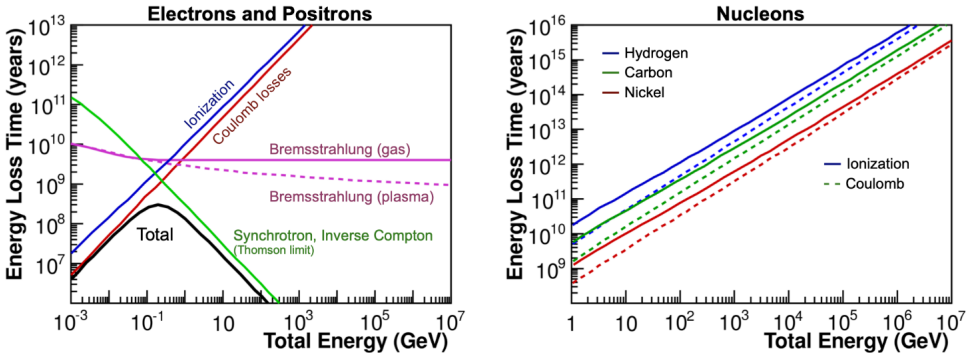

Figure 1.5: Energy loss processes for $e^{\pm}$ (left) and nuclei (right) during propagation in the ISM. The characteristic time required to lose a significant fraction of the particle energy is shown as a function of CR energy for representative ISM and propagation parameters typical of the Galactic environment [26].

In the local interstellar medium, a 100 GeV electron can typically travel no farther than about 1 kpc before losing most of its energy, whereas at 10 TeV, the maximum distance reduces to roughly 200 pc. This locality implies that the measured $e^{\pm}$ flux at high energies provides valuable information on the structure and composition of the Galactic neighborhood. Consequently, precision measurements of high-energy $e^{\pm}$ are essential for constraining nearby CR accelerators, such as pulsars and SNRs, and for testing exotic hypotheses, including dark matter annihilation.

1.2 Dark Matter

Dark matter (DM) has been one of the most intensely studied and debated topics in modern physics over the past several decades. Its existence was first postulated in the early 1930s as a result of a series of astrophysical observations. Since then, extensive theoretical and experimental efforts have been devoted to understanding its nature and properties.

The scientific interest in DM, which nowadays plays a central role in modern cosmology, began more than 90 years ago with the observations of galaxy clusters by the Swiss astronomer Fritz Zwicky [27, 28]. He was the first to infer the presence of an unseen mass component in the Universe. The term *dark matter* refers to this hypothetical form of matter that does not interact with photons and therefore does not emit, absorb, or scatter significant electromagnetic radiation. Decades later, pioneering studies by Vera Rubin [29, 30] in the 1970s on the rotation curves of spiral galaxies, subsequently confirmed by a wide range of observations, revived the interest of the scientific community in this mysterious component. These findings, together with gravitational lensing measurements [31] and other cosmological probes, provided compelling indirect evidence for the existence of a non-luminous form of matter. The current cosmological standard model

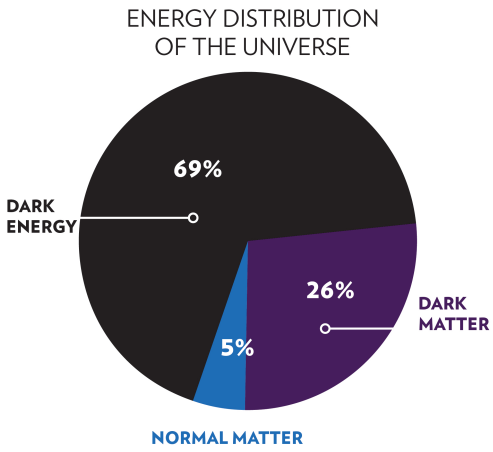

Figure 1.6: Pie chart that illustrates the main components of the universe according to the cosmological standard model. 69% of the energy in the universe is dark energy, 26% is dark matter, while only 5% is ordinary matter.

predicts that DM account for 26% of the energy content of the universe, while ordinary matter only for the 5%. Figure 1.6 the cosmological energy components in a pie chart.

It is, however, important to note that some of the observational evidence cited in support of DM, based primarily on its gravitational influence on astrophysical systems, can also be interpreted within alternative frameworks that do not invoke DM. Among these, Modified Newtonian Dynamics (MOND), first proposed in 1982 and published in 1983 [32], assumes that Newtonian gravity (and, by extension, general relativity) may fail at galactic or cosmological scales. MOND can reproduce the observed rotational velocities of spiral galaxies more accurately than the standard DM model, but it fails to explain the dynamics and mass distributions of galaxy clusters, such as the Bullet Cluster. Furthermore, these alternative theories cannot account for the observed anisotropies in the cosmic microwave background (CMB) [33] or for large-scale structure formation as successfully as DM-based models. For these reasons, the dark matter hypothesis remains the most widely accepted explanation for the current cosmological observations.

According to the standard cosmological model, dark matter is a relic of the Big Bang. The formation of large-scale cosmic structures disfavors the presence of relativistic *hot* dark matter (HDM) and instead supports a scenario dominated by non-relativistic *cold* dark matter (CDM) [34, 35].

Several theoretical models for CDM have been developed, all of which must satisfy few fundamental criteria: the DM particles must be electrically neutral (to avoid electromagnetic interactions), massive enough to contribute to the present-day cosmic mass density, and weakly interacting so that they have not yet decayed or annihilated away. The hypothetical particles that meet these conditions are commonly referred to as Weakly Interacting Massive Particles (WIMPs). Among the most extensively stud-

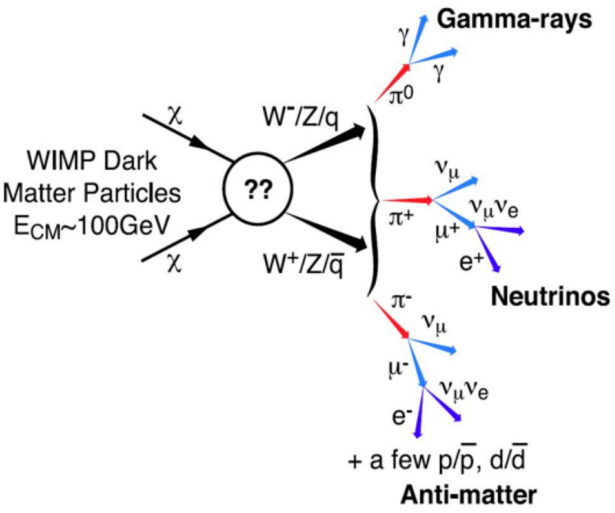

Figure 1.7: The diagram depicts the expected channels of decay/annihilation of WIMP Dark Matter particles. The final states are expected to be either γ-photons, neutrinos or light stable particle-antiparticle pairs.

ied candidates are supersymmetric particles known as neutralinos, denoted by χ, which possess characteristic interaction cross-sections of the weak scale [36, 37].

The latest results coming from both underground and space experiments are pushing more and more stringent constraints on the WIMP mass, challenging the theory itself. Because of this, more complex alternative DM explanations are rising in popularity, like the axions hypothesis, while the WIMP framework still stand as the leading research focus for its easier experimental accessibility[38].

1.2.1 Experimental Investigation of Dark Matter

The experimental investigation of dark matter (DM) and of its properties has experienced a remarkable acceleration in recent decades. Based on a variety of physical principles and detection strategies, the search for DM candidates is conducted through multiple complementary approaches, including high-energy accelerator experiments [39], underground detectors [40], ground-based telescopes [41], balloon-borne instruments [42], and space-based observatories [43, 44, 45, 46].

Among these, the so-called *indirect* detection technique seeks to identify faint signatures of annihilation or decay products of DM particles [47, 48]. This method focuses on the identification of rare components of CRs, photons or neutrinos that exceed the expected flux from known astrophysical sources. The main challenges that indirect DM search need to face are the limited understanding of the astrophysical backgrounds, the substantial systematic uncertainties and the cost and constraints of building such experiments in space. In order to enhance the chance of observing clear signals of DM,

detectors can target specific energy ranges where the expected DM signal is distinct from the background emission or, in the case of photon detectors, regions of the Universe with higher DM density, such as the Galactic center.

A schematic representation of possible DM annihilation channels is shown in Figure 1.7. It highlights the potential production of Standard Model particles, including photons, neutrinos, and charged particles, resulting from DM particle interactions. The detection and study of these annihilation products are made possible by ground-based telescopes, balloon-borne instruments, and satellite detectors.

Among charged particles, positrons and antiprotons are considered the most promising channels for indirect DM detection. A detailed discussion of the electron and positron components of cosmic rays, along with the latest flux measurements, will be presented in Section 1.3. Regarding antiprotons, the AMS-02 experimental results generated debate about possible evidence of DM candidates due to an apparent excess in the energy range between 5 and 10 GeV [49], that would be consistent with potential DM candidates with masses between 50 and 100 GeV [50, 51]. Further studies were not able to unambigously exclude an astrophysical origin for the data[52].

In contrast to charged particles, photons are neither deflected by magnetic fields nor significantly absorbed during propagation, making monochromatic γ-rays one of the most distinctive signatures, or *smoking guns*, for DM annihilation [53]. Searches for γ-ray signals from DM are conducted toward regions of expected high density, such as the Galactic center, the Milky Way halo, nearby galaxies, and extragalactic structures. Ground-based experiments such as MAGIC [54], VERITAS [55], HESS [56], and CTA are optimized for the detection of γ-rays in the TeV range, whereas the Fermi-LAT instrument is particularly suited for observations in the GeV energy domain [57].

Finally, the study of neutrino emissions from DM annihilation provides an additional complementary probe. Hints of DM presence can be investigated through measurements of the diffuse neutrino flux from the Milky Way halo [58, 59], as suggested by IceCube observations in the TeV-PeV energy range. However, compared to photons and charged particles, the detection of cosmic neutrinos poses substantial experimental challenges and currently yields the weakest constraints on the mass of DM candidates, χ.

From this overview, it is evident that the search for the origin/nature of DM remains one of the most active and debated subjects in contemporary physics. Although the current generation of detectors has significantly narrowed the viable parameter space of DM models, no conclusive evidence for its specific nature has yet been found. Future, more sensitive experiments will likely be required to resolve this enduring mystery.

1.3 Measurements of Cosmic Electrons and Positrons

The study of high-energy cosmic-ray electrons (e^-) and positrons (e^+) provides unique insights into both astrophysical particle acceleration mechanisms and potential DM annihilation processes. As we described in section 1.1.4, the propagation of electrons and positrons in the ISM is strongly influenced by energy losses due to synchrotron radiation and IC scattering. The detected flux of $e^{\pm}$ reflects, therefore, the contributions of rela-

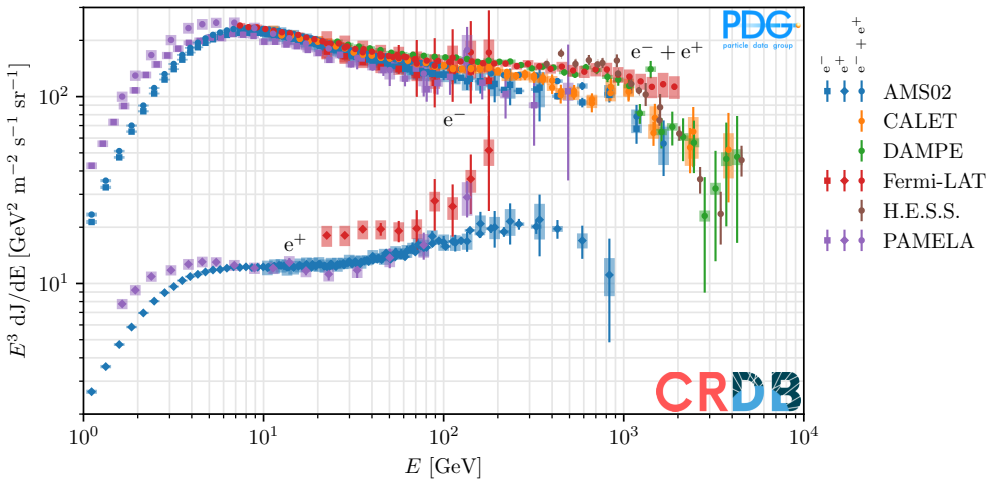

Figure 1.8: Intensities of cosmic ray electrons (squares), positrons (diamonds) and their sum (dots) as a function of kinetic energy E, multiplied by E^3 to enhance the visibility of the spectral features. Data are from CRDB [11].

tively nearby sources, typically within a few kpc of the Solar System, and is sensitive to the structure of the local galactic environment.

Over the last two decades, several dedicated space-based missions have measured the fluxes of cosmic-ray electrons and positrons with unprecedented precision. Figure 1.8 shows a summary of the measurements performed by the key experiments of this era. These experiments include:

- PAMELA (Payload for Antimatter Matter Exploration and Light-nuclei Astrophysics)[60]: operational from 2006 to 2016, PAMELA was a satellite based experimental facility equipped with a magnetic spectrometer that enabled the first detailed measurements of the positron fraction and the $e^{\pm}$ fluxes in the energy range from ~ 1 GeV to several hundred GeV;

- AMS-02 (Alpha Magnetic Spectrometer)[61]: operating onboard the International Space Station since 2011, AMS-02 provides high-precision measurements of both electrons and positrons up to energies of ~ 1 TeV. It is to this day the most complex space instrument for CR detection, employing multiple redundant and independent measurement system in order to minimize systematic uncertainties on measurements;

- Fermi-LAT (Large Area Telescope)[62]: although primarily a γ-ray observatory, Fermi-LAT provides complementary measurements of the combined $e^- + e^+$ spectrum up to ~ 2 TeV through the detection of electromagnetic showers in its calorimeter. Despite not having a magnet onboard, separate spectra for e^+ and e^- were estimated exploiting the different magnetic cut-off from the Earth shadow[63];

- CALET (CALOrimetric Electron Telescope)[64]: installed in 2015 on the International Space Station with a new approach to CR detection that sacrifice the magnetic field in favor of a deep calorimeter (30 X_0) and a broader field of view to collect more events even at higher energies. It provided precision measurement of the combined $e^- + e^+$ spectrum up to several TeV;
- DAMPE (DArk Matter Particle Explorer)[65]: satellite based facility that operates complementary to CALET. It employs a deeper calorimeter (32 X_0) and an even broader field of view.

One of the most notable discoveries in recent years is the rise of the positron fraction above ~ 10 GeV, observed independently by PAMELA, AMS-02, and Fermi-LAT. This behavior deviates from the monotonically decreasing fraction that was expected in a standard framework where all positrons are secondary CRs produced by interactions of primary CRs with the ISM. The observed excess indicates the presence of additional primary positron sources, either astrophysical, such as nearby pulsars and pulsar wind nebulae, or exotic, such as the annihilation or decay of DM particles. Figure 1.9 shows the positron spectrum measured by AMS-02 compared with a model accounting for a primary source term along the secondaries diffuse contribution.

The total $e^- + e^+$ flux exhibits several intriguing features:

- a smooth power-law behavior at low energies, consistent with diffusive propagation from supernova remnants (SNRs);
- a hardening of the spectrum above $\sim$ 50 GeV, indicative of contributions from nearby or young sources;
- potential spectral breaks or cut-offs around ~ 1 TeV, which may reflect the maximum acceleration energy of local sources or the energy loss horizon imposed by synchrotron and IC processes.

These measurements, obtained from the combined contributions of the AMS-02, CALET and DAMPE experiments, enable detailed studies of the source distribution, propagation effects, and the energy dependence of the diffusion coefficient in the local ISM.

The observed features in the $e^{\pm}$ spectrum can be interpreted within two main frameworks: nearby astrophysical sources or dark matter contributions.

Nearby pulsars and pulsar wind nebulae are capable of accelerating $e^{\pm}$ pairs to TeV energies. Their proximity and age determine the energy spectrum and anisotropy of the observed flux. Modeling the injection spectra and propagation of $e^{\pm}$ from these sources can reproduce the observed rise in the positron fraction and spectral features [66];

Certain models of WIMP dark matter predict annihilation or decay into leptonic final states. The energy scale and spectral shape of the positron excess can, in principle, be accommodated within DM scenarios, particularly for particles with masses in the range of $\mathcal{O}(100\ \text{GeV} - 1\ \text{TeV})$. However, robust discrimination from astrophysical sources requires complementary observations, including γ-ray and neutrino channels [67].

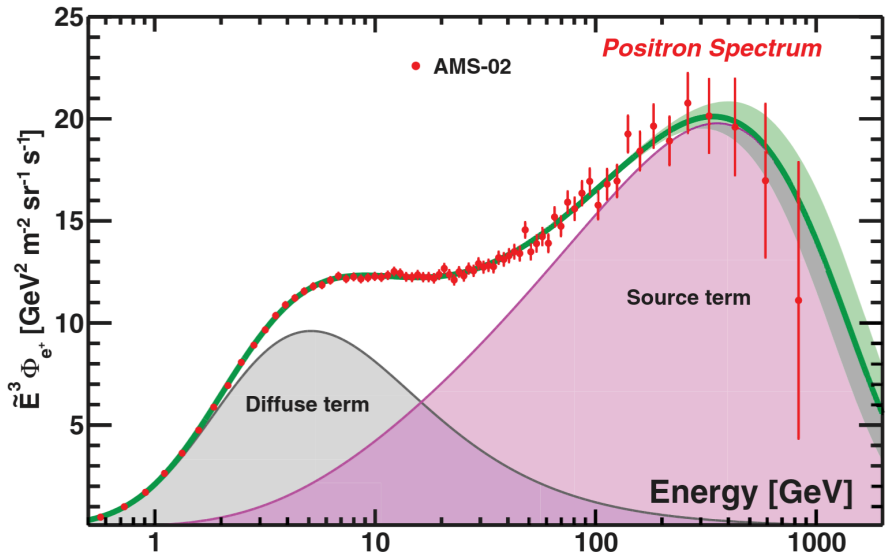

Figure 1.9: AMS-02 measurements [68] of the positron flux as a function of the energy, multiplied by a factor E^3 to better appreciate the characteristics. The picture includes an empirical fit to the data that shows consistency with an additional source of positrons.

High-energy $e^{\pm}$ measurements provide stringent constraints on propagation models. Because electrons and positrons experience severe radiative energy losses, the detected flux is dominated by relatively local sources. Consequently, propagation parameters such as the diffusion coefficient $D(E)$, the halo height z_h, and the energy-loss rates can be constrained with higher accuracy than for hadronic cosmic rays. Additionally, these measurements allow the investigation of potential spatial anisotropies, which can shed light on the distribution of nearby accelerators.

The TeV energy region is crucial to shed light on the origin of the observed positron excess. In particular if we will observe a sharp cut-off this will strongly support the DM scenario, while a smooth tail would compatible with the astrophysical origin. A new generation of CR detectors is therefore necessary to extend our knowledge of the electron+positron spectrum.

Chapter 2

Detection of Cosmic Rays

In the first chapter we described the properties of the CRs spectrum and discussed how broad the energetic range of CRs is. In order to study such a diverse range of events it is necessary to employ extremely different experimental techniques. We can divide these approaches in two main complementary families: direct and indirect detection.

Direct detection of CR particles has to be performed on balloons flying above the stratosphere or orbiting satellites in order to avoid the interaction of the radiation with Earth's atmosphere. However, this kind of space-borne facilities have strict volume, mass, power and bandwidth limitation. This limits the amount of events that they are able to gather in a reasonable time of exposure. This means that, in the span of years of activity, they can only collect a statistically significant amount of data for the more abundant lower energy component of the spectrum. For this reason a crucial feature of direct CR detector is their *geometric acceptance*, a quantity that represents the capacity of a telescope to detect events when is exposed to a certain flux of radiation. In the simple case of an isotropic flux it is expressed by the ratio between the number of events detected and the intensity of the flux (a more general definition will be discussed in chapter 4). This quantity depends not only on the volume of the instrument, but also on its Field of View (FoV), i.e. the solid angle covered by all the direction of arrival of the radiation that the instrument is able to correctly detect. This is why the upcoming space based CR detector will focus on extend as much as possible their FoV in order to strongly increase their acceptance without significantly outgrow the volume and mass of the currently operating experiments. In particular, we'll later describe the upcoming HERD experiment that will achieve a FoV$> 2\pi$, and the proposed design for the ALADInO and AMS-100 projects that want to implement 4π FoV facilities.

The study of more energetic CRs (> 1 PeV), instead, can be performed in large area ground experiments. On ground, these sites, can cover thousands of km^2, but instead of detecting the actual CR particles, they collect the broad shower of secondary particles generated by the interaction of CRs with the atmosphere. Different techniques have been elaborated and often combined to reconstruct the properties of the incoming radiation. We can detect the relativistic muons that populate the long tail of the showers, or the Cherenkov radiation emitted along the atmospheric propagation, or even the radio signal

generated by the electric current of particles moving towards the ground. Studying the features of the shower, we can reconstruct some features like the mass and charge of the primary, but with much less precision compared to direct detection. Nonetheless, thanks to these approach we can study the spectrum of CRs up to extremely high energies.

This thesis will focus on an analysis developed for space-borne detectors. For this reason, after presenting rapidly the other techniques, We're going to analyse with particular detail the peculiarity of this branch of the subject.

2.1 Ground based detection

Ground-based detectors exploit the extensive air showers (EAS) produced when high-energy cosmic rays interact with the Earth's atmosphere. These interactions generate cascades of secondary particles, including electrons, positrons, muons, and photons, which propagate to the ground and can be measured using surface arrays and Cherenkov telescopes. Two primary techniques are employed.

Air Shower Arrays: arrays of scintillation counters or water Cherenkov detectors sample the lateral distribution of secondary particles at the ground. By reconstructing the shower front, the primary particle's energy, arrival direction, and, to some extent, mass composition can be inferred. Examples of large-scale air shower arrays include the Pierre Auger Observatory [69] and the Telescope Array [70].

Imaging Atmospheric Cherenkov Telescopes: IACTs, such as MAGIC [71], HESS [72], and VERITAS [73], detect Cherenkov light emitted by ultra-relativistic charged particles in the atmosphere. This technique provides high-resolution measurements of very high-energy γ-rays (from tens of GeV to tens of TeV), which can be used to search for indirect signatures of DM annihilation and study astrophysical CR sources.

Ground-based detectors typically have large effective areas and are sensitive to the highest energy cosmic rays and γ-rays. However, they suffer from the limited knowledge of the atmospheric showers development especially at such high energies. The impossibility to calibrate the instruments with events of similar energetic scale imposes a strong reliance on Monte Carlo simulations and never tested hadronic interaction models. The typical uncertainty that affect indirect CR measurement are not compatible with the study of fine structures in the spectra or precision of the different components.

2.2 Direct detection

In order to avoid the destructive interaction of CRs with the atmosphere, direct detection can only be performed in high atmosphere or in orbit. For this reason the main solution used during the years are either balloon for short data collection, or satellites for longer exposures. In the future we could see CR detectors installed in space facilities that orbit around a Sun-Earth Lagrange point[74], where, without Earth's shielding and magnetic

field, they will be exposed to a higher flux, or on the Moon surface, where it would be possible to build large area detectors on ground, but avoiding the interaction of an atmosphere. For this kind of facilities is also possible a gradual deployment of a progressively larger active volume, while ensuring the collection of meaningful scientific data during the intermediate stages of its implementation as proposed by the MOONRAY project[75].

Balloon-borne detectors operate above the bulk of the Earth's atmosphere, reducing the background from secondary cosmic rays produced in the air. Balloon flights can last from several hours to a few months, allowing for high-resolution measurements of particle spectra over limited periods. Notable balloon missions include ATIC[76], BESS[77], CREAM[78], SuperTIGER[79], HELIX[80] and GAPS[81].

Balloon experiments are particularly effective for measuring low to intermediate energy cosmic rays (from a few GeV to a few TeV) and for directly observing rare components, such as positrons, antiprotons, and light nuclei. They play a crucial role in testing and validating new technologies that will be installed in more expensive and long-living space-based detectors, but can also produce valuable scientific results thanks to instruments that employ advanced high precision detectors with large acceptance at much lower cost that any space mission. GAPS and HELIX are examples.

The detection techniques and technologies used to study CR both in balloons and space-based facilities are very similar to those used in accelerator experiments. Almost all experiments have a tracker that reconstruct the trajectory of the particles, a charge detector, magnetic spectrometer or calorimeter, or both to extrapolate the total energy of the impinging CR, often time-of-flight systems are also employed to measure the velocity of the particles.

The main strategy employed to measure energy is what divides direct CR experiments in two main families: spectrometers and calorimeters.

2.2.1 Magnetic Spectrometry

textcolorreviewMagnetic spectrometry is a very powerful tool in high energy physics experiments that employs a tracking system immersed in a magnetic field in order to measure the deflection of an electrically charged particle and infer at the same time its rigidity (i.e. $p/|Z|$), the sign of its charge and its arrival direction. If the spectrometer is combined with charge detectors and velocity detectors it should be possible to fully reconstruct the particle species, energy and trajectory. AMS-02[61] is the most important CR experiment that employs such technology for particle detection.

While having a lot of useful capabilities, the implementation of magnetic spectrometers in space also presents experimental limitations. A particularly relevant difficulty lie in generating and maintaining strong, stable magnetic fields in the harsh environment of space, where power availability is limited and thermal control is complex. If not properly designed to cancel itself outside the facility, a strong magnetic field in a light satellite based will also couple with the Earth magnetic field generating a precession on the facility. SuperConducting (SC) magnets, commonly required for high-resolution measurements, demand cryogenic cooling systems that must operate reliably over long durations with-

out maintenance, but with current technologies this is almost impossible because of the constraints on mass, volume, and power imposed by launch vehicles. For this reason only permanent magnets have currently been implemented in space spectrometers with magnetic fields up to 0.15 T (AMS-02). In recent years, thanks to the emerging technology of high temperature superconducting materials, employing SC magnets in space spectrometers is starting to be more feasible. The balloon based experiment HELIX employed a 1 T SC magnet that was able to mantain operation condition for about 7 days[80].

The limitation in the strength of the magnetic field translates in a limit also on the precision of the reconstruction. We can see how, evaluating the relative uncertainty on the measured momentum p.

Let's consider a particle with charge Z that enters a uniform stable magnetic field B. The Lorenz force applied to the particle is

$$\vec{F_L} = Ze\vec{v} \times \vec{B}$$

Charged particles in magnetic field follow circular trajectory, thus F_L acts as a centripetal force

$$F_L = \frac{mv^2}{\rho}$$

Where ρ is the radius of curvature of the trajectory. If we consider the particle entering the tracker perpendicular to $\vec{B}$ we find a relation between the momentum $p = mv$ of the particle and ρ

$$p = ZeB\rho$$

When ρ is high enough the deviation angle θ of the trajectory can be approximated with its tangent. If the magnetic field's depth is L then $\theta = L/\rho$. This give us the relation

$$p = \frac{ZeBL}{\theta} \tag{2.1}$$

$$\frac{dp}{d\theta} = \frac{ZeBL}{\theta^2} = \frac{p^2}{ZeBL} \tag{2.2}$$

So we can get an expression for the relative uncertainty on the momentum that is

$$\frac{\sigma(p)}{p} = \frac{p}{ZeBL}\sigma(\theta) \tag{2.3}$$

The measurement of the deflection angle depends on the measurement of the direction before and after the magnetic field and its resolution is determined, not only by the spatial resolution of each tracking planes, but also by how many are used for the measurement and how distant they are between each other. It's important to highlight how, while having more tracking planes provides more data to measure the trajectory, it also forces the particle through more material that increase the chance of multiple Coulomb scattering that can change its direction of motion. The scattering actually become the dominant source of uncertainty at low rigidities[82] and drives the necessity to build spectrometers as thin as possible.

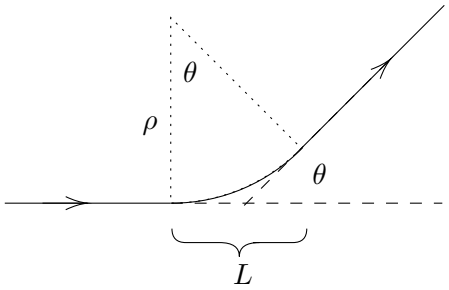

Figure 2.1: Trajectory of charged particle in a magnetic field.

The key property to get from Eq.2.3 is that the relative uncertainty on the momentum $\sigma(p)/p$ is directly proportional to the rigidity. This means that, once fixed the design of a magnetic spectrometer, the measurements that it will be able to provide for a given particle species will be worser the higher the momentum of the such particle. In particular for every spectrometer it exists a rigidity value at which the relative uncertainty is 100%. This value is called the Maximum Detectable Rigidity (MDR).

2.2.2 Calorimetry

Calorimeters are detectors designed to measure the total kinetic energy of a particle by transferring such energy to the material of the calorimeter itself. To absorb such energy the calorimeter forces the particle through a series of destructive interactions that produce a cascade of secondary particles. Employing scintillating materials the calorimeter can convert the energy that these particles lose by ionization in visible photons that can be detected and measured by photodetectors to infer the total energy of the primary particle.

We can distinguish calorimeters in two main types: *homogeneous calorimeters* and *sampling calorimeter*. Calorimeters of the first type are made of a single scintillating material that is used to both induce the interactions and produce the scintillation. Sampling calorimeters, instead, alternate the scintillator with dense passive materials that can produce intense interaction even in short depth. Calorimeters of this latter type have worse energy resolution due to the fraction of the energy that is inevitably lost in the passive material, but can be much less expensive and need considerably less depth, and therefore volume and mass to completely absorb events of the same energy.

For a calorimeter that can properly contain the shower of a detected particle, the energy resolution can be approximated as the summation in quadrature of three main behaviors:

$$\frac{\sigma_E}{E} = \frac{a}{\sqrt{E}} \oplus \frac{b}{E} \oplus c \tag{2.4}$$

In this expression a emerges as a combination of multiple Poisson-like fluctuations like the variation in shower particles absorbed in sampling calorimeters, that of scintillation photons emitted by the scintillator and electrons produced in photodetectors. The term b depend on the electronics noise and pile-up of background particles that produce an

uncertainty independent on the energy of the detected event.At last c appears mostly due to calibration uncertainty and crystal non-uniformity.

It's important to highlight how, unlike what we saw for magnetic spectrometers, the energy resolution gets better at higher energies. This crucial property calorimeters are a fundamental choice for energy measurement in the current and next generation of cosmic rays experimental facilities.

If a substantial quantity of shower particles escape the calorimeter volume without being detected we talk about *leakage* of the shower. The leakage can be either from the front of the calorimeter (*albedo* or *backsplash*), from the sides (*lateral leakage*) or from the rear (*longitudinal leakage*). The different kinds of leakage represent further sources of uncertainty, but their contribution behaves very differently according to the energy of the event.

Backsplash is the only type of leakage that cannot be avoided at all through design choices for the calorimeter. It's generated by the scattering of particles produced at large angles due to processes like Compton scattering or photoelectric effect. Since the energies of the scattering products are at maximum a few MeV, the fraction of energy that is escaping is only relevant for very low-energy showers.

Lateral leakage can be contained employing larger calorimeters and is therefore easier to deal with through design choices. Even if some leakage is present this doesn't produce a very strong effect on energy resolution because it can be well accounted for through calibration. The lateral spread of a shower is indeed highly simmetrical and can be precisely characterized. The fraction of energy escaping through lateral leakage decreases with increasing energy of the primary particle beacuse of the narrower angle at which the more energetic shower particles are produced.

Longitudinal leakage is the contribution of more concern in the design of a calorimeter. Unlike with lateral leakage, the energy fraction escaping longitudinally is subject to strong fluctuations. This is because it is strongly tied to the first interaction of a single particle from which the shower starts. Longitudinal leakage grows at higher energies and is therefore necessary to tailor the calorimeter depth specifically for the energy range that will be of interest to study. As we'll discuss in more detail in the next chapter, the longitudinal extension of a shower scales as the logarithm of the energy of the primary. This means that also the depth of a calorimeter should scale with the logarithm of the maximum energy meant to study.

This is a fundamental difference when comparing the performance of a calorimeter to a magnetic spectrometer for energy measurement in space detectors. We saw in section 2.2.1 that the maximum rigidity detectable by a spectrometer grows linearly with the depth of the magnetic field. With the size constraints of space missions calorimeters represent a much more efficient solution for precision measurement of high energy events.

Note that even if a calorimeter cannot completely contain a shower, it doesn't mean that it can't properly reconstruct the energy of the particle. Many calorimeters use a longitudinal segmentation that enables the sampling of the development of the shower at different depths. This allows to calibrate the calorimeter response according to the profile of the shower.

Calorimeter segmentation can provide even further information about the observed particle. In particular, the profile of the shower can be used to discriminate different kind of particles that produce showers based on different types of interactions. The most common application in space detectors is the discrimination of electrons and positrons from protons and anti-protons withouth the need to measure the sign of the charge. More details will be illustrated in the next chapter.

There are also downsides in the calorimetric approach. A big problem in particular is the calibration of high energy events. The calibration of spectrometers mostly requires precise alignment of the tracking layers, that can be achieved easily with laser systems, and the measurement is easily performed just by tracking the trajectory of a single particle in the magnetic field. Calorimeters require to model a huge number of secondary particles that are subject to several statistical processes. For this reason calorimeter response need to be calibrated carefully with experimental data or, for the energies that we cannot reach in laboratories, with Monte Carlo simulations. The use of simulations causes a systematic uncertainty on the measurement coming from the limited understanding of the underlying processes.

2.3 Next generation experiments

A leading goal for the next generation of direct CR detectors will be the extension of all the currently known energy spectra up to energies at least an order of magnitude larger than those currently reachable. Since the spectrum of all the CR components decrease approximately as a power law, the main problem to face is the decreasing statistics of detectable events. The new experiments will need to increase their gathering power, without exceeding the mass, volume and power constraints of space missions. This is why these upcoming facilities will leverage the isotropy of CRs and focus on new instrumental design based on the maximization of their field of view. A first step will be taken in the near future by HERD[83], a forecoming experiment for high-energy CR direct measurement based on a novel isotropic design. The core of HERD will be an isotropic calorimeter, finely segmented in three dimensions, that will provide both a precise energy measurement and powerful e/p discrimination for events incoming from any direction. This solution is already considered to be the new standard for any new generation CR detectors.

A step even further will require ambitious ideas like those proposed by ALADInO[74] or AMS-100[84] projects, that foresee to employ novel design and new technologies never tested before in space like high temperature superconducting magnets together with a 3D segmented calorimeter based on the HERD design.

2.3.1 HERD

The High Energy cosmic Radiation Detector (HERD)[83] is a facility for direct detection of CRs that will be installed on the Chinese Space Station Tiangong3 in 2028. The experiment is being developed by an international collaboration lead by the Institute of High

Energy Physics (IHEP) and the Chinese Academy of Science (CAS) of Beijing. Important contributions came from several research institutes from Italy, Spain and Switzerland.

HERD aims at measuring CR protons and Helium up to the PeV energy order, heavier nuclei up to hundreds of TeV per nucleon, electrons (and positrons) and γ photons up to tens of TeV. Its scientific goals include resolving the nuclear composition of CRs at the knee and consequently sheding light on its origin, and precisely characterizing high-energy electrons, positrons, and gamma rays for potential dark matter signatures.

To reach the aforementioned energies, which are more than 1 order of magnitude higher than those accessible by current space-borne experiments, HERD will employ a novel design based on a deep, isotropical, highly-segmented, homogeneous calorimeter, combined with tracking and charge measurement sub-detectors that surround the calorimeter on 5 out of the 6 faces of the cubic facility, granting a wide field of view larger than half a full solid angle. This configuration leverages the isotropy of the CR flux to maximize the detectable events without increasing significantly the volume and mass of the facility with respect to currently operating experiments.

At the heart of HERD is a large, three-dimensional, imaging calorimeter (CALO) composed of about 7500 small LYSO scintillating cubes. This homogeneous, finely segmented structure features more than 50 radiation lengths and several interaction lengths in depth, ensuring good containment of both electromagnetic and hadronic showers at the studied energies. Because it can accept particles from the top and four sides, HERD achieves a geometric acceptance several times larger than any previous detector.

Complementary sub-detectors provide charge, tracking, and veto capabilities. These include silicon trackers with tungsten converters for gamma-ray conversion and direction measurement, plastic scintillators for charge and anti-coincidence, a dedicated silicon charge detector, and a transition radiation detector for high-energy calibration. Together, these instruments give HERD precise particle identification capabilities and robust separation of electrons and gamma rays from the much more abundant proton background.

With the current design, HERD is expected to reach 1% energy resolution for electrons and gamma rays above 100 GeV, 20% for hadrons up to PeV energies, and electron/proton separation up to 10^5. These capabilities will make HERD the of the most powerful instruments for direct cosmic-ray studies in space, possibly helping to clarify the mechanisms of cosmic acceleration, propagation, and potentially revealing hints of new physics.

CALO

The CALOrimeter (CALO) [85, 86] is the core detector of the HERD instrument. It is a spherical, homogeneous, and fully 3D-segmented calorimeter capable of detecting particles incoming from any direction. Its design builds upon the results of the CaloCube R&D project[87], which extensively studied this detector concept. Based on those findings, the baseline configuration of CALO consists of approximately 7500 LYSO (lutetium-yttrium oxyorthosilicate) cubes, each with a 3 cm edge length, corresponding to about 2.6 radiation lengths X_0 and 1.4 Molière radii. The calorimeter cubes are arranged in spherical

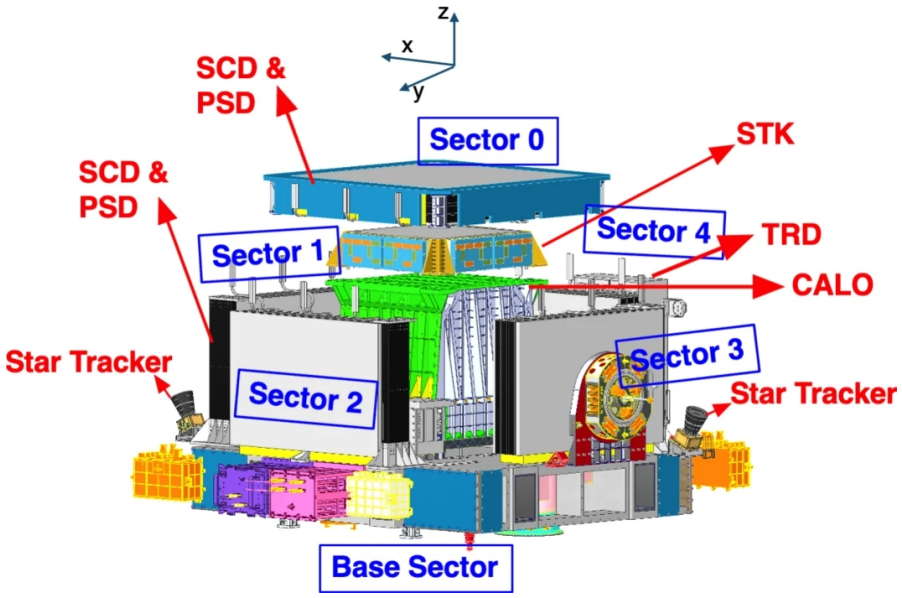

Figure 2.2: Exploded schema of the HERD structure showing all the sub-detectors surrounding the central calorimeter.

configuration, identical when looked from any side of the detector. For particles that cross the CALO along its diameter, the total calorimeter depth is approximately 55 X_0 or 3 interaction lengths λ_I.

Each crystal's scintillation light is collected through a double readout system that enables cross-calibration of energy measurements. The first readout chain employs wavelength-shifting fibers (WLSF) coupled to image-intensified scientific CMOS (IsCMOS) cameras, while the second uses PhotoDiodes (PDs) of different active areas, connected to a customized front-end electronics.

The WLSF system employs two loops of 300 µm thick fibers attached to each crystal that collect photons and re-emit them at their ends in the wavelength region 450-600 nm. One end of each fiber is connected to a IsCMOS camera, while the other two ends are connected, together with other fiber coming from nearby cubes, to a Photo Multiplier Tube (PMT) to provide fast trigger signals.

The double PD read-out system is based on the use of two types of PD with different active areas: the Large PD (LPD) and the Small PD (SPD). This solution relies on the SPD to measure precisely the smaller signals, while it employs the LPD for larger signals that saturate the SPD, therefore achieving a broad dynamic range and enabling a cross calibration on the overlapping energy range.

The double readout architecture not only ensures redundancy, but it also enhances the precision of energy scale calibration. This latter factor is expected to be of crucial importance since recent cosmic-ray calorimetric experiments have suggested that energy scale uncertainties may contribute to discrepancies in electron flux measurements.

Together with the Transition Radiation Detector (TRD), the CALO's design will

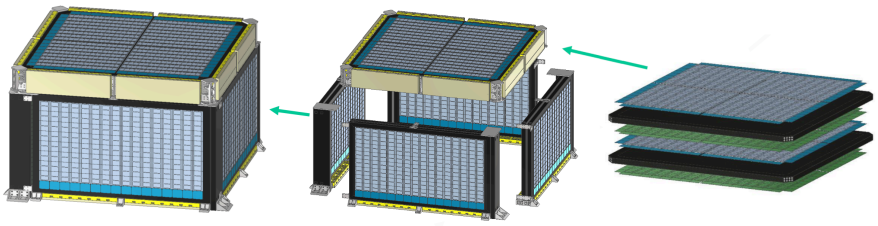

Figure 2.3: 3D render of the SCD modules as they will be assembled on the HERD facility. On the right the top module is exploded to show how the single layers (grey and green) will be mounted on the aluminum supports (black).

significantly improve the accuracy, stability, and understanding of the energy scale in future HERD cosmic-ray measurements compared to previous detector generations.

SCD

The Silicon Charge Detector (SCD)[88] is the first subsystem encountered by incoming particles in the HERD instrument. Positioned just above the Plastic Scintillator Detector (PSD), it is designed to provide accurate charge measurements across HERD's wide field of view. The use of a silicon-based charge detector at the top of the instrument minimizes the chances of interactions and eventual nuclear fragmentation of the incoming particles before a precise charge measurement, thereby reducing systematic uncertainties in cosmic-ray flux measurements.

In its current design, the SCD consists of five detector modules: one square module measuring 1.6×1.6 m^2 located on the top of the instrument (sector 0), and four lateral modules (sectors 1 to 4) each measuring 1.4×0.9 m^2 mounted on the sides. See figures 2.2 and 2.3 for a diagram of the structure. Each detection unit includes eight layers of 320 µm-thick silicon microstrip detectors with 150 µm pitch. The layers are arranged alternately in orthogonal orientations and supported by low-density aluminum honeycomb panels. The overall active detection area amounts to approximately 60 m^2.

Monte Carlo simulations and beam tests of the detector system have been performed to evaluate the SCD's charge measurement performance. Results indicate that the combined charge resolution from the eight-layer configuration is better than 0.3 charge units (c.u.) for all species and, in particular, better than 0.15 for $Z = 1$[88].

In addition to charge identification, the SCD also provides 3D tracking capability, which will be exploited in conjunction with the STK subsystem for precise particle trajectory reconstruction. These added functions enhance inter-detector redundancy and enable cross-calibration between HERD sub-detectors, improving overall measurement reliability.

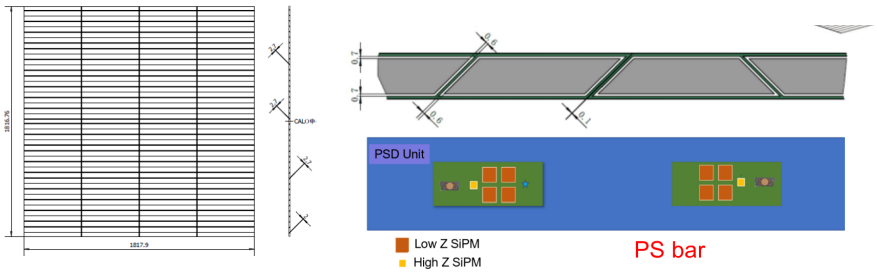

Figure 2.4: The picture on the left shows how the plastic bars will be arranged to cover the full square plane of a sector of the PSD. Sizes are in mm. On the top right, the section view of a layer show the trapezoidal cross-section of the bars that enables the strict hermeticity of the PSD, while on bottom right a map of the different types of SiPM mounted on the bars to collect the broad range of signals from the scintillators.

PSD

The Plastic Scintillator Detector (PSD) of HERD [89, 90] serves as an anti-coincidence detector distinguishing incident photons from charged particles, but also provides a second precise charge measurements for incoming cosmic-ray nuclei up to $Z = 26$ and timing information with a 1 ns resolution to aid in track reconstruction.

The PSD will hermetically cover the same 5 sectors of the SCD employing a single layer of scintillator bars with a trapezoidal cross-section. This peculiar shape enables the overlap between adjacent bars to achieve tighter hermeticity of the planes. The top plane will measure 180×180 cm^2, while each one of the four side planes will measure 170×95 cm^2. The planes will be made up of plastic bars 45 cm long, 4 cm broad and 1 cm thick. Figure 2.4 shows how the bars will assemble in a hermetic plane and a schema of the installed SiPM.

The tiles are read out by Silicon PhotoMultipliers (SiPMs) placed on the top of the tiles, to ensure high light detection efficiency and dynamic range for nuclei identification. The readout design includes different SiPMs for low high-Z detection, with 4 Low-Z SiPMs (3.0×3.0 mm^2, 50 µm cell) and 4 High-Z SiPMs (1.3×1.3 mm^2, 15 µm cell). The smaller SiPMs will be used for high-charge detection since saturation at higher photon flux with respect to the bigger.

The PSD's performance has been validated through extensive prototype testing and beam tests, demonstrating its capability to meet the requirements of the HERD mission (i.e. detection efficiency $> 99.8\%$ and charge resolution $< 10\%$.)

STK

Sector 0 will also mount an inner Silicon TracKer (STK)[91] between the PSD and the top side of the CALO. This subdetector will not only perform precise tracking on particles entering CALO, but will also employ tungsten layers to induce pair production in γ-photons to perform high energy astronomy.

The planes will employ 14 single layer silicon strip detectors alternately placed in orthogonal orientations and interposed with tungsten layers. Each silicon layer is 500 µm thick and has a 250 µm pitch.

The ongoing beam tests that are being performed have established for the STK a spatial resolution of about 54 µm and an angular resolution for γ-rays $< 0.1^\circ$ at 10 GeV.

TRD

For TeV-scale protons a relevant fraction of the generated showers leaks from the CALO, but ground calibration of spaceborne calorimeters is limited to particle energies of up to $\sim$ 400 GeV, constrained by the maximum beam energy available at the CERN SPS. Consequently, the energy of more energetic events must be inferred through extrapolation from lower-energy data, a process that introduces significant uncertainties.

To overcome these limitations, a Transition Radiation Detector (TRD)[92, 93] can be employed to directly calibrate the energy of incident particles within the range where transition radiation (TR) is produced but not yet saturated. The emitted TR energy is proportional to the Lorentz factor γ of the incoming charged particle. Transition radiation photons are generated when $\gamma \sim 10^3$ and reach saturation at $\gamma \sim 10^4$, corresponding to proton energies between roughly 1 and 10 TeV. By detecting the X-rays produced through this mechanism, the TRD enables a direct and absolute energy determination of incident charged particles in the TeV region by measuring their Lorentz factor.

The TRD is implemented through a modular and highly redundant design, consisting of three layers, each made up of nine detection modules. Every module includes a TR radiator, an X-ray gaseous detector with an active area of 20×20 cm^2, and associated readout electronics, all supported by grid-like mechanical frames. This configuration ensures both high sensitivity and robust performance for in-orbit calibration of the calorimeter's energy scale. The module is only installed on one side of the facility, but leverages the abundancy of protons in CRs to perform continuous calibration of the CALO performances at various temperature condition and even after years of operations, when the crystals are expected to lose transparency.

2.3.2 Next generation spectrometers

While the innovative solutions introduced by HERD are already ground-breaking in terms of acceptance, the lack of a magnetic spectrometer implies the impossibility to perform precision studies on antimatter abundance that are extremely sensitive to DM models, but also the lack of a second energy measure to exploit for high energy cross-calibration. Two main design proposals for next generation magnetic spectrometers are already emerged and are under preliminary study: ALADInO[74] and AMS-100[84].

Both these projects rely on the isotropic calorimeter design introduced by HERD for both energy measurement and particle e/p discrimination, but explore different approaches to encapsule the calorimeter inside a large acceptance magnetic spectrometer. For the magnetic field they will both leverage high-temperature superconducting tapes made of second-generation rare-earth barium copper oxide (ReBCO), operating around

40 K, which avoids the need for liquid helium cryogenics and greatly enhances thermal stability and quench resistance[94].

Both these proposals aspire to be implemented in the high-Earth orbit or preferably at the Sun-Earth Lagrange point L2. These region grants a reduced geomagnetic shielding that enable the precision measurement of antimatter CR components from GeV to supra-TeV scale.

The combination of spectrometric measurement with the deep absorbing calorimeter enables their cross-calibration, opening the opportunity for precision, data-driven determination of the absolute rigidity scale in space, improving what is achievable at calibration beams at ground and consequently reducing one of the major systematic uncertainties in flux measurements [95]. Similarly, the cross-calibration improves the uncertainty on the absolute energy scale of calorimeters, which in space can be only calibrated at tens of GeV using a data-driven determination of the geomagnetic rigidity cutoff [96, 97], and which strongly contributes to the error on the determination of the CR flux intensities.

ALADInO

The Antimatter Large Acceptance Detector In Orbit (ALADInO)[74] project is a proposed CR magnetic spectrometer that employs novel technological and design solutions to perform CR charge sign identification and rigidity measurement up to an MDR larger than 20 TV. A baseline design for the ALADInO detector is shown in Figure 2.5.

The most distinctive feature of the detector is the design of its spectrometer that is based on a toroidal magnetic field generated by 10 high-temperature superconducting coils. This design grants an average magnetic field of 0.8 T in the tracker volume, while minimizing the stray field on the outside.

The instrument is further equipped with a central 3D imaging calorimeter, inspired by the HERD design. The calorimeter features a depth of 61 radiation lengths X_0 corresponding to approximately 3.5 nuclear interaction lengths λ_I for precise measurement of the energy spectra of $e^{\pm}$.

Finally, the instrument is completed with a time-of-flight featuring $\mathcal{O}(10^{-2})$ resolution in the velocity measurement for efficient isotopes separation.

The instrument can employ three different acceptance configurations, illustrated in figure 2.5, exploiting the redundancy in energy measurement to reconstruct events that cross both the spectrometer and calorimeter, but also those crossing only the spectrometer or only the calorimeter.

The central calorimeter of ALADInO is designed on the example of the HERD CALO. It's built assembling 3 cm long and 3 cm thick LYSO cylinders in a honeycomb configuration for a total depth of 60 X_0 or 3.5 λ_I. It provides, not only precise energy measurement beyond the MDR of the spectrometer, but also expand significantly the total acceptance of the facility. For particles that cross both the spectrometer and calorimeter the geometric factor is expected to be $\sim$3 $\mathrm{m}^2\,\mathrm{sr}$, while for the calorimeter only or spectrometer only it goes up to $\sim$10 $\mathrm{m}^2\,\mathrm{sr}$.

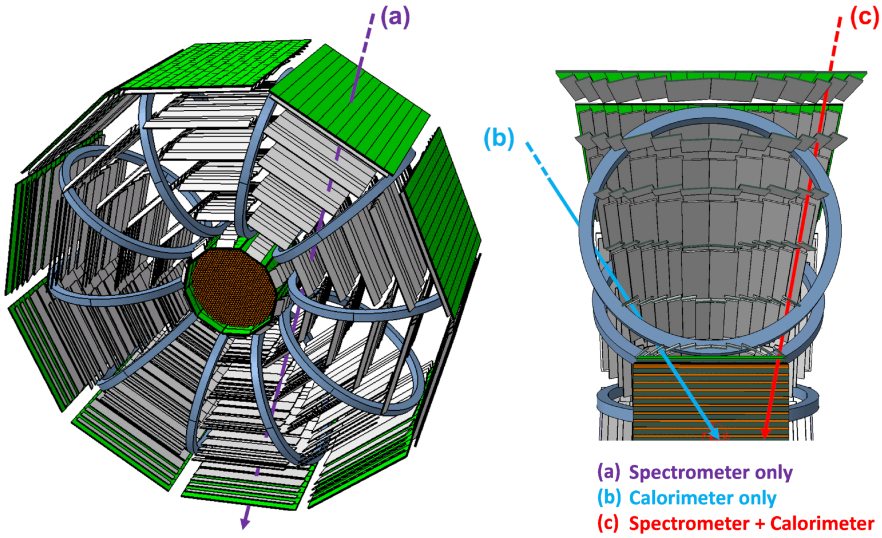

Figure 2.5: Overview of the design proposed for ALADInO. Arrows exemplify the 3 acceptance configurations.

The combination of a magnetic spectrometer and calorimeter in the ALADInO facility also allows for high energy cross-calibration up to the PeV energy scale significantly reducing the systematic uncertainty level that we have in purely calorimetric detectors like DAMPE or CALET.

AMS-100

AMS-100[84] is an alternative proposed solution to implement a novel CR magnetic spectrometer to explore the high energy CRs. The driving feature of this project is the unprecedented acceptance of 100 m^2 sr. This acceptance value is 10 times larger than that reached by ALADInO in calorimeter-only configuration.

Instead of a toroidal magnetic field, AMS-100 employs a uniform magnetic field generated by a high temperature superconducting solenoid made out of the same ReBCO bands proposed for ALADInO. Since the field is not zero outside the solenoid, the facility also need a compensation coil around it to avoid the precession of the station. For the tracking, the spectrometer will exploit six double layers of silicon microstrip detectors with 50µm spatial resolution. This tracking capability combined with the 1 T magnetic field produced by the 4 m radius coils will grant an MDR of about 100 TV.

At the center of the solenoid, AMS-100 employs a deep homogeneous cylindrincal calorimeter with a depth of 70 X_0 or 4 λ_I. Inspired by the HERD design, the calorimeter will be highly segmented in three dimensions to provide e/p discrimination based on the reconstruction of the shapes of showers. The calorimeter will be wrapped in pre-shower detector consisting in 12 layers of silicon detectors interleaved with tungsten layers. This pre-shower detector will provide good angular resolution for the detection of γ-rays and

will limit the rate of shower particles backsplashing towards the tracker.

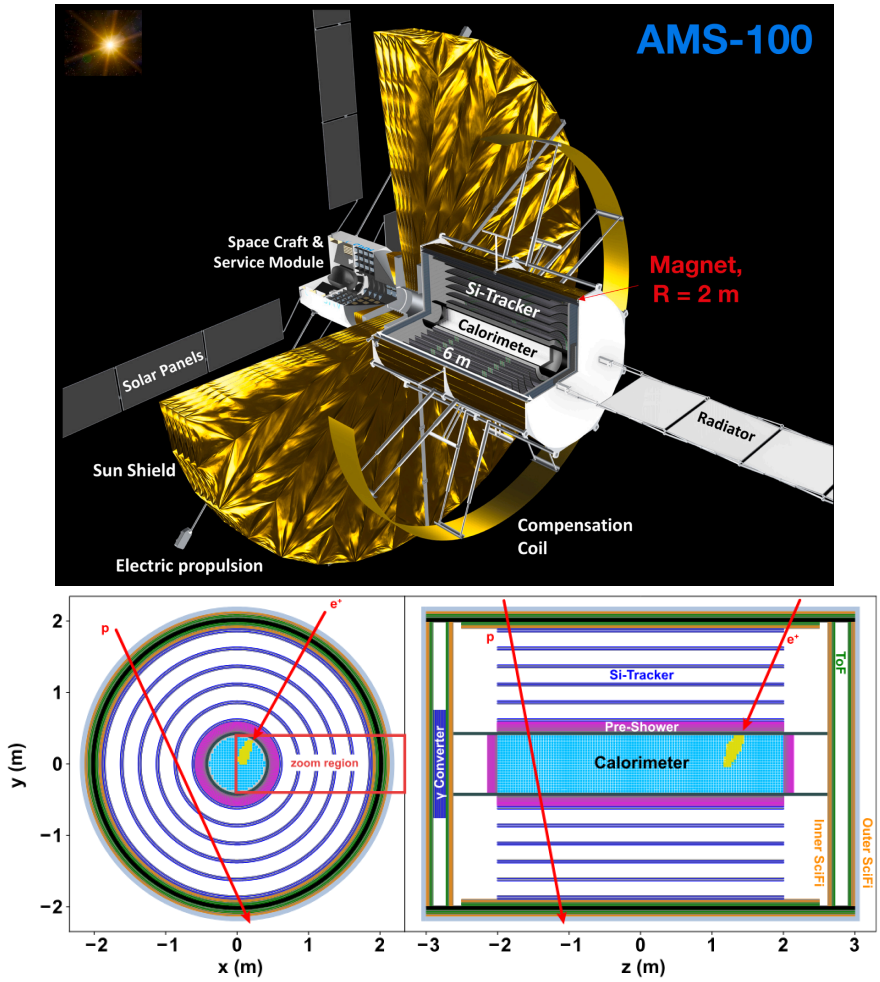

Figure 2.6: The picture on top is a rendering of the proposed design for AMS-100. On the bottom two orthographic projections of the detector depict the two possible acceptance configurations.

Chapter 3

3D calorimetry

In chapter 2 we presented the properties of calorimeters illustrating in detail how convenient they are for precise energy measurement in CR direct detection. We also briefly introduced how the segmentation of calorimeters allow to study the topological development of particle showers in order to implement powerful particle identification based on the different kind of interaction that generate the showers.

Since this thesis aim to describe the development of an e/p discrimination tool, in this chapter we'll now focus on how the electrons-generated and proton-generated showers differ and how we can use 3D calorimetry to discriminate between the two particle species.

3.1 Particle showers

When a relativistic particle traverses a dense material, it undergoes a series of inelastic interactions with the atoms and nuclei that it crosses. These interactions produce new energetic particles that keep interacting with the material generating even more secondary particles. This avalanche effect produces the so-called particle shower. Since different kind of particles undergo different types of interaction that translate in showers with different properties, these showers can be classified into two main categories:

- electromagnetic showers: generated by electrons, positrons or photons;
- hadronic showers: generated by hadrons like protons, pions or kaons.

3.1.1 Electromagnetic showers

Cascade showers produced by electrons, positrons and photons are sustained by the same kind of purely electromagnetic interactions, for this reason they are classified as ElectroMagnetic (EM) showers.

In order for a shower to start, electrons or positrons need to radiate γ-photons energetic enough that each photon can decay in $e^+ + e^-$ pair and that this produced pair can keep radiate again to keep the cascade going. The process that generate such γ-photons is called bremsstrahlung and, even if the rate of emission is material-dependent,

already for $e^{\pm}$ more energetic than about 100MeV it is the dominant source of energy loss in most materials. The emitted photons need to have an energy of at least 1MeV to produce the mass of the $e^+ + e^-$ pair. Less energetic photons will interact through Compton scattering or photoelectric effect releasing rapidly all their energy to the material. When the secondary $e^{\pm}$ are produced with energies below the so-called critical energy E_c their dominant source of energy loss will become the ionization of the material and their branch of shower will rapidly stop developing and be absorbed.

The energy radiated through bremsstrahlung can be described by the law

$$-\left(\frac{dE}{dx}\right)_{rad} = \frac{E}{X_0}. \tag{3.1}$$

This relation implies an exponential loss of energy or equivalently that when an electron crosses a slab of material with depth X_0, it loses, on average, $1/e$ of its energy by bremsstrahlung.

X_0 is called radiation length and is a property of the traversed material that can be evaluated approximately as

$$X_0 \simeq \frac{1}{\rho[\mathrm{g/cm^3}]} \frac{716.4\, A[\mathrm{g/mol}]}{Z(Z+1)\ln(287/\sqrt{Z})}\mathrm{cm}. \tag{3.2}$$

ρ, Z and A are density, atomic number and atomic mass of the traversed material.

For photons the rate of interaction can be described in terms of the mean free path λ. If we consider a beam of N photons, the average variation in their number, per unit thickness, due to pair production is given by:

$$\frac{dN}{dx} = -\frac{N}{\lambda}. \tag{3.3}$$

The quantities λ and X_0 are actually interdependent through the relation

$$\lambda = \frac{9}{7} X_0. \tag{3.4}$$

The parameter X_0 therefore represents a characteristic length scale for both bremsstrahlung and pair production processes and is thus used as a reference in the study of electromagnetic showers. For the description of the longitudinal development of an electromagnetic shower it is generally useful to define the depth of the shower in units of radiation length as $t = x/X_0$.

The Heitler model

The Heitler model provides a simplified description of the evolution of an electromagnetic shower that is useful to visualize the different component and mechanisms behind the generation of an electromagnetic cascade. It is based on three main assumptions:

- electrons and positrons lose energy only through bremsstrahlung, while photons interact solely through pair production;

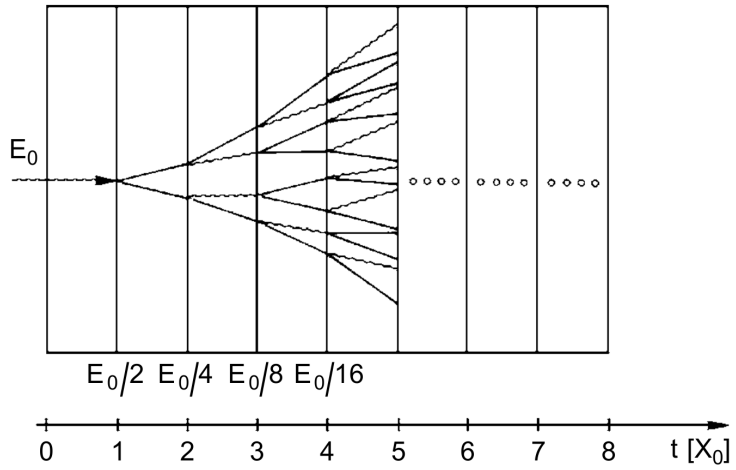

Figure 3.1: Visualization of the Heitler model to describe the shower development. Every X_0 each particle in the shower either radiate or decay, doubling the total number of particles that populate the cascade, while each of them is left with half the energy of the previous step.

- after traveling one radiation length X_0, each photon produces an e^+e^- pair, and each electron or positron emits one photon via bremsstrahlung;
- the energy of the interacting particle is equally divided among the outgoing particles at each interaction vertex.

Figure 3.1 illustrates the development scheme of this model.

In this framework, the number of particles as a function of depth is described by a simple power of 2 as:

$$N(t) = 2^t \tag{3.5}$$

and consequently the energy of a single particle at depth t is

$$E(t) = \frac{E_0}{N(t)} = E_0 \cdot 2^{-t}. \tag{3.6}$$

When the energy of the produced particles drops below the critical energy E_c the emission of new particles ceases. This condition corresponds to the point of maximum shower development, when the number of particles reaches its peak.

In the Heitler model, each particle at this point has an energy equal to the critical energy. Substituting $E(t) = E_c$ into Eq. 3.6 gives the depth of maximum development:

$$t_{max} = \frac{\ln(E_0/E_c)}{\ln(2)} \propto \ln(E_0/E_c) \tag{3.7}$$

and the corresponding maximum number of particles:

$$N_{max} = \frac{E_0}{E_c} \tag{3.8}$$

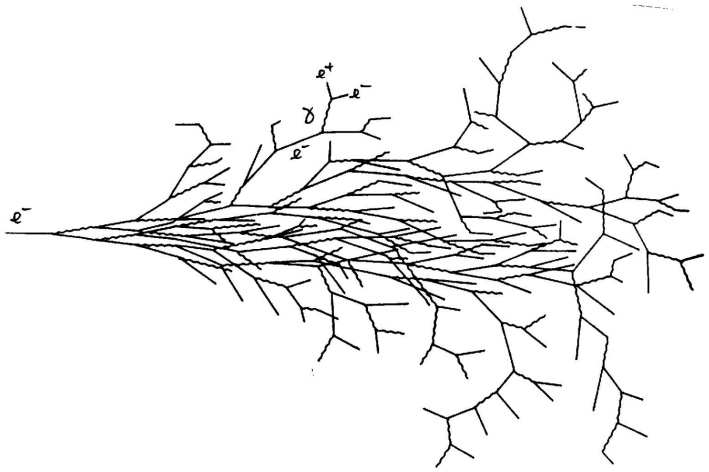

Figure 3.2: Schematic representation of a simulated electromagnetic cascade. Straight lines represent electrons and positrons, while wavy lines represent photons.

After reaching this maximum, the number of particles decreases as electrons and positrons lose energy through ionization and excitation, while photons are absorbed by the photoelectric effect or lose energy via Compton scattering. In general, the particles in the shower come to rest within a few radiation lengths X_0 beyond the point of maximum development.

Despite its simplicity, the Heitler model reproduces at least two key features of electromagnetic showers that are observed experimentally:

- the proportionality between the maximum number of particles and the energy of the primary particle $N_{max} \propto E_0$;
- the proportionality between the depth of maximum development and the logarithm of the primary particle's energy $t_{max} \propto \ln(E_0)$.

Gamma distribution model

Realistic showers are far more complex than the description provided by the Heitler model. Fig. 3.2 shows a rendering of the processes and particles involved in an electromagnetic shower.

A far more complete and realistic description of the EM shower development was developed by Rossi and Greisen in 1941[98]. They elaborated a set of integro-differential equations that describe how the number of electrons and photons evolves as they travel through matter, taking into consideration theoretically sound bremsstrahlung and pair production (in Approximation A) and also the ionization losses (in Approximation B). The analytical solutions to these equations cannot be trivially deducted, but the model is able to predict many characteristic features that include the dependence of the peak with respect to the energy or the exponential decay of tail.

These properties where exploited by Longo and Sestili in 1975[99] to develop a semi-empirical function that accurately describe the average longitudinal development of EM showers:

$$\frac{dE}{dt} = E_0\, b\, \frac{(bt)^{a-1} e^{-bt}}{\Gamma(a)} \tag{3.9}$$

where E_0 is the energy of the incident particle that initiates the shower, a and b are material-dependent parameters, and $\Gamma(a)$ is the Euler gamma function. In this approximation, the depth of maximum development is:

$$t_{max} = \frac{a-1}{b} = \ln\left(\frac{E_0}{E_c}\right) + C \tag{3.10}$$

where C is a constant that takes different values depending on the species of the particle that initiated the shower. $C = 0.5$ for photons, $C = -0.5$ for electrons or positrons.

Figure 3.3 presents the longitudinal energy-loss profiles for a 10 GeV electron-induced shower in lead, iron, and aluminum. Although the depth is expressed in units of X_0, a dependence on the absorber material remains, due to differences in the critical energy E_c.

Lateral spread

Regarding the lateral development of the shower, the angular distribution of particles produced by bremsstrahlung and pair production is very narrow (the typical opening angle being of the order $m_e c^2/E_\gamma$). Thus, the dominant process governing lateral spread is multiple scattering, which the particles undergo as they traverse the medium. According to Molière's theory of multiple scattering[100], the lateral spread is characterized by the Molière radius, defined as:

$$R_M = \frac{21\text{MeV}}{E_c} \cdot X_0[\text{cm}] \cdot \rho \left[\frac{\text{g}}{\text{cm}^3}\right] \tag{3.11}$$

Approximately 95% of the shower energy is released within a cylinder of radius about twice the Molière radius, almost independently of the primary particle's energy.

Figure 3.4 shows both the longitudinal and lateral development of a shower initiated by a 6 GeV electron in lead.

3.1.2 Hadronic showers

Like for the EM case, hadronic showers are generated by a cascade of inelastic interactions between high-energy particles and a material. This type of showers are sustained by hadronic interactions between the particle and the nuclei of the material producing mostly pions, both neutral and charged, and less frequently nucleons, kaons, and other hadrons.

While in electromagnetic showers the longitudinal development is characterized by the radiation length X_0, in hadronic showers the characteristic length is the mean free path for inelastic nuclear interactions, or *interaction length*, λ_I, defined as:

$$\frac{dN}{dx} = -\frac{N}{\lambda_I} \quad , \quad \lambda_I = \frac{A}{N_A\ \rho\ \sigma_{inel}} \tag{3.12}$$

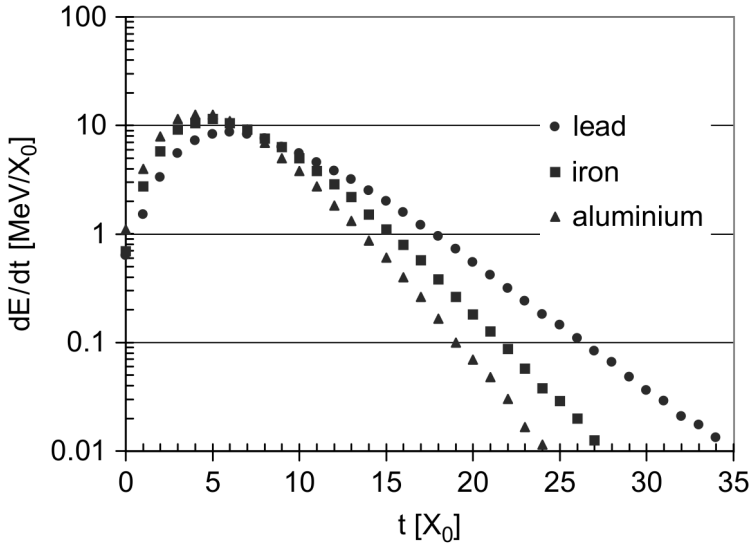

Figure 3.3: Longitudinal development of the electromagnetic shower initiated by 10 GeV electrons in different materials. Data from [101]

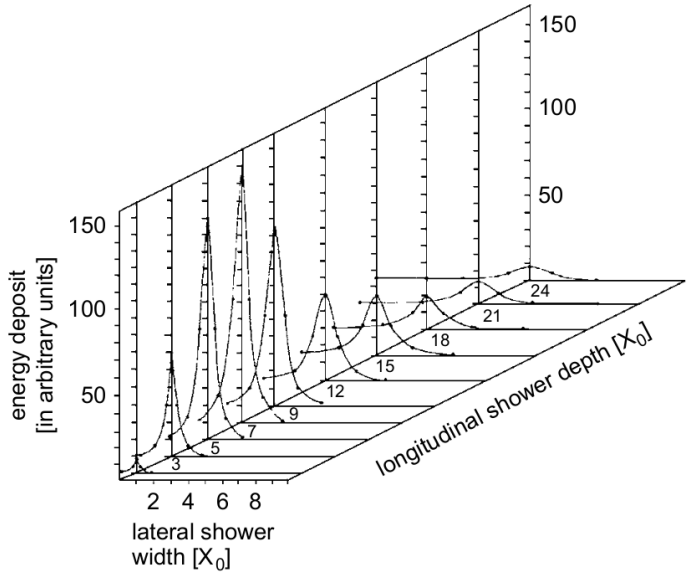

Figure 3.4: Longitudinal and lateral development of an electron shower (6 GeV) in lead. Data from [102]

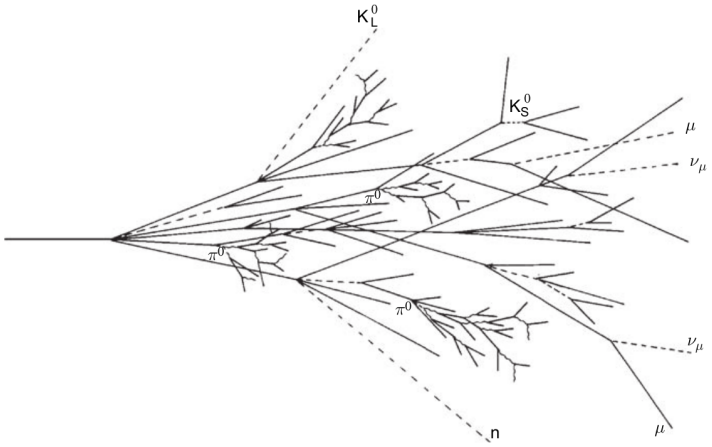

Figure 3.5: Schematic development of a hadronic shower. The solid straight lines represent charged particles that take part in the cascade interactions, wavy lines are photons, while dotted lines are particles that escape the calorimeter accounting for the invisible energy of the shower.

where A and ρ are respectively the mass number of the nuclei and the density of the medium, σ_{inel} is the inelastic nuclear interaction cross-section between the incident hadron and a target nucleus, and N_A is Avogadro's number. For energies larger than a few GeV, σ_{inel} depends only weakly on energy and particle type, so the expression for λ_I can be approximated as:

$$\lambda_I \simeq 35 \frac{\mathrm{g}}{\mathrm{cm}^2} A^{1/3} \tag{3.13}$$

Figure 3.5 shows the lateral and longitudinal development of a shower induced by a pion with a momentum of 10 GeV in iron.

Unlike what we saw for the EM case, modeling hadronic showers is a much more complex matter. This complexity results from the broader variety of particles involved in the cascade, the interactions occurring and the different scale a wich they develop.

One key feature to discuss is the relevant fraction *invisible energy*. About 30-40% of the energy of any hadronic shower cannot be detected and is therefore completely lost because of the energy that goes into breaking nuclear bonds, the production of stable or long-lived neutral particles that escape the calorimeter without interacting (neutrons, neutrinos, K^0), and the production of muons from π and K decays, which traverse the calorimeter depositing only a small fraction of their energy. The fraction of invisible energy varies significantly from event to event.

Among the large number of pions generated in a hadronic shower, roughly one-third are neutral pions (π^0), which decay into two photons with a branching ratio of about 98.8% and a characteristic lifetime of 10^{-16} s. The resulting photons can initiate electromagnetic sub-showers. If the incident hadron has an energy E_0, the average fraction of energy released as electromagnetic sub-showers can be described by the phenomenological

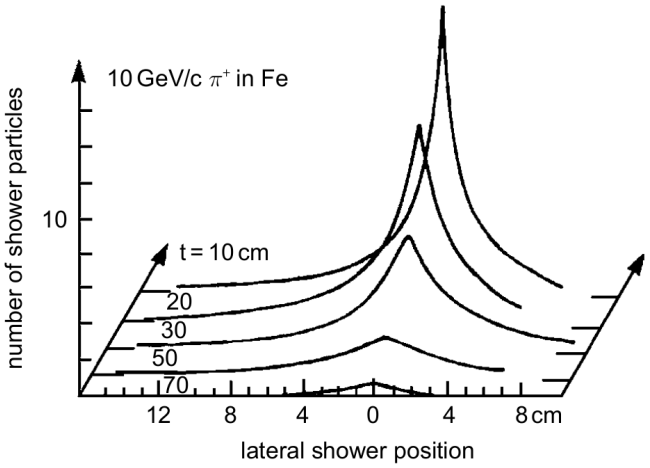

Figure 3.6: Longitudinal and lateral profile of the hadronic shower generated by a 10 GeV positive pion in iron.

expression:

$$f_{em} = 1 - \left(\frac{E_0}{E_h}\right)^{k-1} \tag{3.14}$$

where $k \simeq 0.8 \div 0.85$ while E_h depends strongly on the material in which the shower develops (for example, $E_h \simeq 0.7$ GeV for iron and $E_h \simeq 1.3$ GeV for lead). However, the production of π^0 mesons is subject to large fluctuations due to the stochastic nature of hadronic interactions. Consequently, the electromagnetic energy fraction also fluctuates strongly from event to event, and combined with the different calorimeter response to electromagnetic and hadronic components, this adds significant complexity to the modelization of the showers.

A schematic representation of the longitudinal and lateral development of a hadronic shower is shown in Fig. 3.6

An accurate model of the development of the hadronic showers is of crucial importance for the calibration of the response of calorimeters, but there is no analytical functions that describe the development as the gamma model does for EM showers. The longitudinal development is generally expressed in terms of the *containment length*, defined as the length within which 95% of the shower energy is contained. Figure 3.7 shows the longitudinal extension of the showers generated by pions of different energies in iron. From these experimental data emerges a linear dependence between the length of the shower and the logarithm of the energy of the primary. A fit for showers in iron gives us the relation:

$$L(95\%) = [9.4 \ln(E[\text{GeV}]) + 39]\,\text{cm} \tag{3.15}$$

By scaling this equation using the values of λ_I for different materials, one can estimate the containment length for the desired absorber.

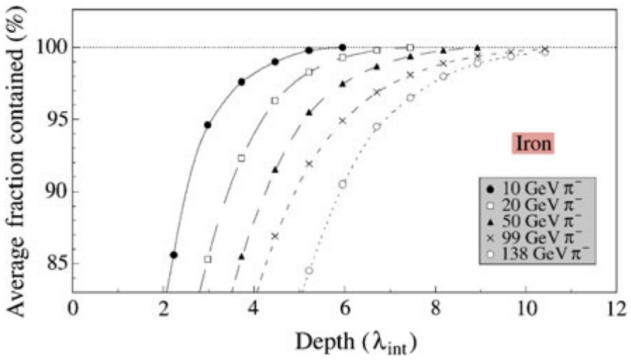

Figure 3.7: Experimental values of the average shower energy fraction contained in a given depth of iron for pions of different energies.

The lateral development of a hadronic shower is related to the large transverse momentum (on average about 0.35 GeV) imparted to secondary particles at each hadronic interaction vertex. For this reason we cannot rely on Molière's theory for multiple scattering like we do for EM showers. The lateral development can be parameterised analogously to the longitudinal one by defining a containment radius. In general, the lateral development of a hadronic shower depends on the energy and scales proportionally with λ_I. A more accurate description of the longitudinal development must also include, besides the purely hadronic component, the electromagnetic contribution arising from the decay of π^0 mesons into photons.

Typically, in materials used for calorimetry, λ_I is much larger than X_0, as shown in Tab. 3.1, which lists characteristic quantities of electromagnetic and hadronic showers for several materials. Consequently, in the same material, the longitudinal development of a hadronic shower is much greater than that of an electromagnetic one.
The same applies to the lateral containment, where λ_I for hadronic showers should be compared to twice the Molière radius for electromagnetic showers (recalling that about 95% of the shower energy is released within a cylinder of radius $2R_M$).

Material	X_0	λ_I	R_M
Tungsten	0.35 cm	9.95 cm	0.93 cm
BGO	1.12 cm	22.8 cm	2.26 cm
LYSO	1.14 cm	20.9 cm	2.1 cm
Silicon	9.37 cm	46.52 cm	4.94 cm

Table 3.1: Comparison of the radiation length X_0, the interaction length λ_I, and the Molière radius R_M for several materials commonly used in the construction of (electromagnetic) calorimeters.

3.2 Calorimetric particle ID

Identification of particles in high energy experiments is mostly based on two principles:

- mass measurements;
- differences in interactions.

Since the first approach cannot be realized as a direct measurement, mass has to be deduced from other variables. These are in general the momentum p and the velocity $\beta = v/c$, where one exploits the basic relationship

$$p = \gamma m v \quad \rightarrow \quad m = \frac{p}{c\,\beta\,\gamma} \tag{3.16}$$

Here c is the speed of light in vacuum and $\gamma = (1-\beta^2)^{-1/2}$ is the relativistic Lorentz factor. The resolution in the mass determination is

$$\left(\frac{dm}{m}\right)^2 = \left(\frac{dp}{p}\right)^2 + \left(\gamma^2 \frac{d\beta}{\beta}\right)^2 \tag{3.17}$$

Because of the γ^2 term, in most case relevant to CR physics, the mass resolution is dominated by the momentum uncertainty at low energy (low γ), while it becomes completely determined by the velocity resolution for energies above tens of GeV.

The momentum is obtained by measuring the curvature of the track in a magnetic field. The particle velocity is instead obtained by means of one of the following methods:

- measurement of the energy deposit by ionization,
- time-of-flight (TOF) measurements,
- detection of Cherenkov radiation or
- detection of transition radiation.

We already saw in section 2.2.1 how momentum resolution depends linearly on momentum itself for rigidities over the GV scale. The measurement of ionization loss is practically not viable because for relativistic particles the loss is almost constant, with respect to β, and therefore does not provide the required resolution for its estimation.

Also the time-of-flight measurement gets less precise as the velocity increases. This is because the time resolution is fixed by the detector design while the time of flight of particles gets shorter the faster is the particle.

$$\beta = \frac{L}{c\delta t} \longrightarrow \frac{\sigma(\beta)}{\beta} = \frac{c\beta}{L}\sigma(\delta t) \tag{3.18}$$

Cherenkov radiation detectors use the emission angle θ_c to determine velocity thanks to the relation

$$\beta = \frac{1}{n\cos(\theta_c)} \tag{3.19}$$

Here n is the refraction index of the radiator material. Also in this case the resolution gets worse with increasing β:

$$\frac{\sigma(\beta)}{\beta} = n \sin(\theta_c)\, \beta\, \sigma(\theta_c) \tag{3.20}$$

Transition radiation (TR) detection is the only principle that holds even at higher energies. The detection principle is based on the emission of photons (typically X-rays) by charged particles when crossing the boundary between two medium with different dielectric constant. The emitted intensity linearly grows with the γ of the particle without saturating at high energies like Cherenkov does. This means that measuring the TR we can precisely infer beta or directly the mass from γ as $m = E/(\gamma c^2)$. TR detectors can thus be used for powerful particle ID at high energies up to the saturation of the X-ray detectors. This method, indeed, has proven to provide strong e/p discrimination capabilities in AMS-02, but also showed its limitation when compared with calorimeter based identification when energy approaches the TeV scale[103].

Calorimeter-based particle identification is the most powerful e/p discrimination approach for the supra-GeV energy range. It has been proven to be the main discrimination tool in AMS-02 [103, 104] and lead the design choice for the calorimeters of both CALET [64] and DAMPE [65] that feature, in fact, imaging calorimeters to reconstruct the shower topology development. It exploits the analysis of the different shower development mechanisms of electromagnetic and hadronic interactions in matter. Electrons and photons predominantly interact via bremsstrahlung and pair production, generating electromagnetic showers characterized by compact lateral profiles of the order of the Molière radius and longitudinal containment determined by the material's radiation length X_0. In contrast, protons and nuclei undergo inelastic nuclear interactions, producing hadronic showers with larger fluctuations, deeper starting points, and broader spatial extension, typically scaling with the nuclear interaction length λ_I. Figure 3.8

By measuring observables such as the depth of the first interaction, the longitudinal shower profile, transverse energy spread, and total deposited energy, a finely segmented calorimeter can perform event-by-event particle discrimination. Combining this topological information with energy resolution enables reliable separation of hadrons from electrons and photons, and even the identification of some nuclei proving to be an essential tool for cosmic-ray composition studies at TeV-PeV energies.

3.3 3D segmented calorimeters

In the previous section we discussed how the most powerful tool for particle ID, and in particular for e/p discrimination, at high energies is the calorimetric approach based on the study of the topological feature of showers. In currently operating CR experiments like AMS-02, DAMPE or CALET, this is approached with segmented calorimeters. In each of this these experiments the calorimeter has a layered structure, where each layer is segmented again to form a hodoscopic structure, where each layer is placed in an orthogonal orientation with respect to the next one. This way the showers generated by

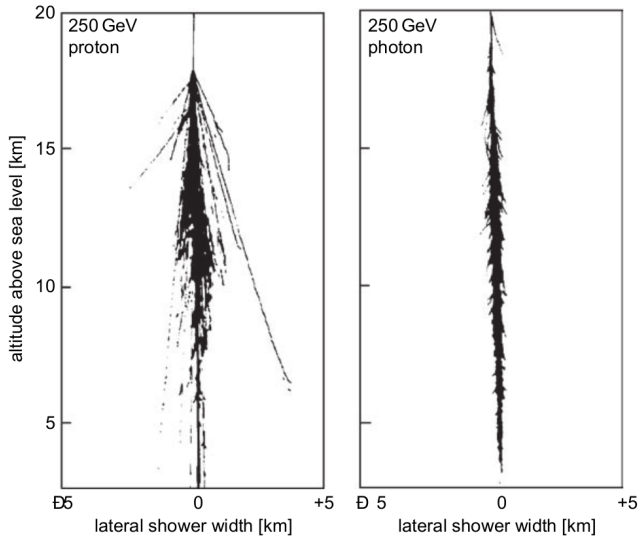

Figure 3.8: A comparison between the cascade shower generated by a 250 GeV proton (left) and a 250 GeV photon (right).

particles that impinge from the front of the calorimeter are sampled along their longitudinal direction (z), but also along one of the lateral directions, either x or y depending on the specific layer.

The same detailed 3 reconstruction of the shower cannot be performed on showers that enter the calorimeter with a strong inclination or that enter from a side of the detector. This result in a limitation of the acceptance of the instrument. As we discussed in chapter 2 the next generation of CR direct detectors will need to leverage the larger possible acceptance to explore higher energy CRs. This is why the CaloCube[87, 105, 106] project explored the feasibility of a fully segmented calorimeter that can reconstruct events from any arrival direction. The experience of CaloCube served as the basis for the design of calorimeter employed by HERD and by any of its successors.

3.3.1 CaloCube model

CaloCube[87, 105, 106] was a research project, supported by INFN, CNR and several Italian Universities, aimed to test the feasibility and performance of a new type of calorimeter for space-borne high-energy cosmic rays detectors.

The detector concept was based on a highly granular, homogeneous cube of scintillating crystals of CsI(Tl), assembled as a three-dimensional matrix. This design maximizes geometrical acceptance by being isotropically segmented in x, y and z direction. Particles can be detected from multiple directions while offering enough depth in radiation and interaction lengths to contain particle showers. The fine segmentation allows accurate reconstruction of electromagnetic and hadronic cascades, as well as particle identification. Light detection is provided by photodiodes applied directly on the cubes and connected

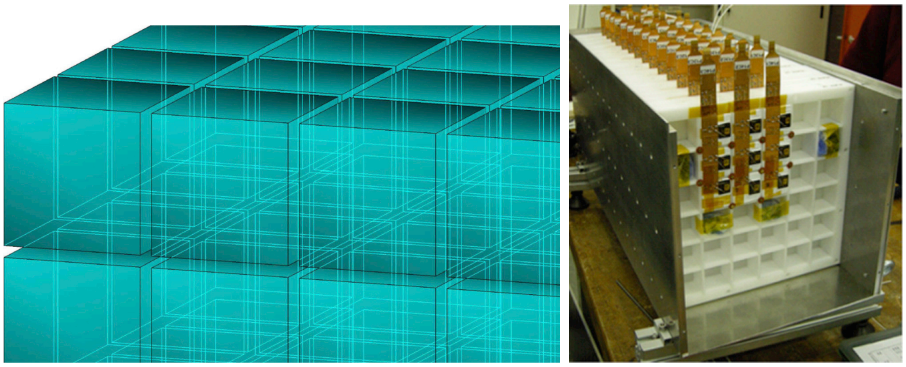

Figure 3.9: Graphical representation of 3D matrix structure of the Calocube design (left) and a picture of the actual prototype (right) used during beam test at SPS-CERN [106].

to kapton cables that gather the signal to the external ADC. The photodiodes employed need a large dynamic range that balance good sensitivity for MIP ionization or distant tails of the shower, with the ability to handle even the highest signals from PeV scale events.

The size of the cubes was chosen as a compromise between the granularity needed to characterize the showers' shape and the cost in terms of power needed to run a high number of photodiodes. The chosen size for the crystals in the prototype was $36 \times 36 \times 36$ mm^3, corresponding to $1.95X_0$ edge cubes.

The project has combined Monte Carlo simulations with the construction and testing of prototypes at CERN and other facilities. Beam tests with electrons, protons, and ions have validated the expected performance, especially for electromagnetic showers, where energy resolutions below a few percent are achievable. Simulations also confirmed that CaloCube could reach effective acceptances several times larger than current space-borne instruments, while keeping total mass within feasible limits for launch. Results so far indicate that CaloCube is going to be the basis of a next-generation of space calorimeter.

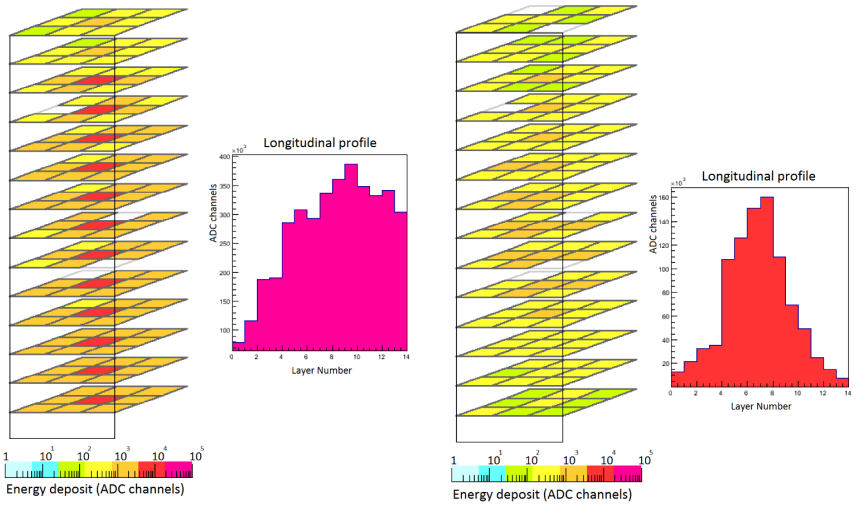

Figure 3.10: Graphic visualization of the reconstructed events in the Calocube prototype. A proton (left) and an electron (right). Data are from beam test performed at SPS-CERN [105]. Thanks to the granular design is possible to simultaneously reconstruct the longitudinal and lateral development of the showers enabling novel discrimination capabilities for isotropic events.

Chapter 4

Space-borne measurements of $e^- + e^+$

In this chapter we will describe the elements necessary to perform a study of the flux of cosmic rays and an estimation of the accuracy that we'll be able to reach with the detector design that we are taking in consideration for this work. We'll exploit the HERD proposed design as case study and we'll focus on the measurement of the combined flux of electrons and positrons in CRs. Because of the lack of a magnetic spectrometer we cannot separate the flux of e^+ and e^-, but the combined flux is still a significant matter of study for many CR properties.

4.1 Flux measurement

For charged CRs we are usually interested in describing the flux as the differential intensity rate of particles in a certain region of space. The integral flux Φ is defined as

$$\Phi = \frac{dN}{dt\, dS\, d\omega} \tag{4.1}$$

where dN is the number of particle crossing a unit area dS from a unit solid angle $d\omega = d\phi dcos(\theta)$ in the unit interval of time dt. This flux is commonly studied as a differential flux in energy

$$\Phi(E) = \frac{d\Phi}{dE} \tag{4.2}$$

From this definition, $\Phi(E)$ has units of $\mathrm{GeV}^{-1}\,\mathrm{m}^{-2}\,\mathrm{sr}^{-1}\,\mathrm{s}^{-1}$.

The data collected by a detector are typically classified according to an energy binning based on the estimated event energy and the whole analysis is performed as function of binned energy intervals. In this framework, the flux can be expressed as:

$$\Phi(\tilde{E}) = \frac{\Delta N(\tilde{E})}{\Delta E \Delta t(\tilde{E}) A_{eff}(\tilde{E})} \tag{4.3}$$

where ΔN is the number of particles collected by the detector and selected by the analysis for the energy bin $[E, E + \Delta E]$, Δt is the exposure time employed to record the crossing particles and A_{eff} is the effective acceptance for the particular analysis. This last quantity is a typical characteristic of the detector that quantifies the gathering power of the instrument and that depends both on the size of the detector and on its Field of View. Each of these parameters depend on the energy of the observed particles, and are therefore quoted as a function of $\tilde{E}$, which is the most representative energy value for the energy bin $[E, E + \Delta E]$. In the case of CRs, since we expect a power law for the differential flux, $\tilde{E}$ is commonly chosen has the geometric mean of the bin extrema.

Eq. 4.3 holds in the assumption of an absolute flux measurement, where no dependence on the particle incoming direction is studied. The differential flux of particles for a given solid angle $\Delta\Omega = \Delta\phi\Delta cos(\theta)$ is expressed as a generalization of Eq. 4.3 by:

$$\frac{d\Phi(\tilde{E})}{d\Omega} = \frac{\Delta N(\tilde{E}, \Delta\Omega)}{\Delta E \Delta t(\tilde{E}) A_{eff}(\tilde{E}, \Delta\Omega)} \tag{4.4}$$

where $\Delta N(\tilde{E}, \Delta\Omega)$ is the number of particles collected by the detector and selected by the analysis for the energy bin $[E, E+\Delta E]$ and the solid angle $[\Omega, \Omega+\Delta\Omega]$, and $A_{eff}(\tilde{E}, \Delta\Omega)$ is the differential effective acceptance of the detector for the particular analysis for the field of view covered by $\Delta\Omega$. The measurement of the differential flux $d\Phi/d\Omega$ is of particular interest for directional analyses, like the search for anisotropy signals in the antimatter fluxes.

The effective acceptance A_{eff} is a crucial element to be able to reconstruct an absolute flux from experimental data, but it's not of straightforward derivation. It depends on a combination of purely geometric properties, the efficiency of the detectors and the event selection chosen for a certain analysis. In particular when performing a measurement on a specific particle species, candidate events need to satisfy several conditions related to a trajectory that crosses the relevant detectors in active areas that grant good quality of reconstruction, but are also related to the efficiency with which the events are detected and extracted from the background of other kind of events. These conditions are specific to the particle species, and they produce different types of uncertainty on the counting of events.

4.1.1 Uncertainty on the flux

Let's explore the specific way in which the elements of Eq. 4.3 impact on the uncertainty.

The counting N is the number of detected signal. If a detector is exposed to a pure flux, with no background, this measurement should be a purely Poisson phenomenon. In most real application, background events exist and must be removed through events selections. These selections have typical efficiencies that could depend on many factors like, particle species or energy, and, for CR experiments they are often impossible to evaluate without relying on Monte Carlo simulations. If the selection is strong enough to completely remove background N could still be considered a Poisson variable, but if a residual background exists, this must be statistically estimated using technicals like

template fits. With this kind of approaches the uncertainty on N will be a combination of the signal Poisson uncertainty and the background Poisson uncertainty. Section 4.4 will describe this procedure in detail.

The uncertainty on the term A_{eff} is more complex because it depends on the geometry of the telescope, but also on the efficiency of the detectors, the efficiency of the quality selections and of any other cuts applied to events. Because of its complexity, the uncertainty on this term must be evaluated using Monte Carlo simulations, but since in most cases it's impossible to finely calibrate the simulations results with experimental data, many uncertainties add up in this term. When these uncertainties are also correlated to energy or background rejection, they introduce unwanted systematic effects in terms of flux normalization or flux energy dependence. In section 4.2 and 4.2.2 we'll see with some more detail the procedure to study this parameter.

The uncertainty deriving from ΔE is mostly coming from the uncertainty in energy measurement. For a flux $\Phi(E) = E^{-\gamma}$ measured with energy resolution $\sigma(E)/E$, the relative uncertainty on Φ is proportional to $\gamma\sigma(E)/E$. In direct CR detectors this translates in a strong dependence of the Φ resolution from the energy resolution. The width ΔE of the energy bin mitigate this uncertainty.

The uncertainty on exposure depends on an easy time measurement except for the lower rigidity particles that are affected by the geomagnetic field. The physics of such processes are well understood and the contributions to uncertainty are mostly negligible.

4.2 Geometric acceptance

The counting rate of any particle telescope depends on the intensity of the radiation that the detectors is exposed to, but also on geometric properties like the effective dimensions and relative positions of the sensitive components, and on their efficiencies.

For an ideal telescope, whose efficiency for detecting particles of a given type is 1 in a given energy interval and 0 otherwise and whose sensors are mathematical surfaces with no thickness, the factor of proportionality relating the counting rate C to the intensity $I(\omega) = dN/(dtdSd\omega)$ is defined as the *gathering power* (Γ) of the telescope.

In the particular case of a detector with efficiency 1, exposed to an isotropic radiation ($I(\omega) = I_0$) the proportionality factor between the counting rate and radiation intensity is called *geometrical factor* or *geometric acceptance* (G).

$$C = GI_0 \tag{4.5}$$

Despite being possible to analytically evaluate the geometric factor and gathering power of a telescope for a few very simple configurations, in most cases it's necessary to rely on numerical approximation based on Monte Carlo methods. Describing the theoretical formulation of these quantities is however worth the effort in order to better understand their properties, but also to derive some formulae useful for the numerical approach to the problem.

4.2.1 General analytical formulation

The counting rate of a particle telescope can be expressed as:

$$C(\vec{x},t) = \frac{1}{T}\int_0^T dt \int_S d\vec{\sigma}\cdot\hat{r}\int_\Omega d\omega \int_0^\infty dE\,\varepsilon(E,\vec{\sigma},\omega,t)\Phi(E,\vec{x},\omega,t) \tag{4.6}$$

where

C = coincidence counting rate (s^{-1}),
Φ = spectral intensity of the radiation or flux ($s^{-1}\,m^{-2}\,sr^{-1}\,GeV^{-1}$),
ε = detection efficiency,
t = time after the start of observation,
T = total observation time,
$d\vec{\sigma}$ = element of surface area of the last telescope sensor to be penetrated,
S = total area of the last telescope sensor,
$d\omega = d\phi dcos\theta$ = element of solid angle (θ polar angle, ϕ azimuth),
Ω = domain of ω, this is limited by the other telescope sensors,
$\vec{x}$ = spatial coordinate of the telescope,
$\hat{r}$ = unit vector in direction ω, and
$\hat{r}\cdot d\vec{\sigma}$ = effective element of area looking into ω.

This equation expresses the requirements for the detection of a particle and, although being quite general, still requires several implicit assumptions like:

1. that $d\vec{\sigma}$, ω, and $\vec{x}$ are time independent, which would not be the case for a spinning telescope;
2. that no transformation of particle type occurs;
3. that the particle trajectory is a straight line; and
4. that Φ is independent of $\vec{\sigma}$ and ε of $\vec{x}$.

The dropping of these assumptions only complicate Eq. 4.6 and renders an analytic solution difficult.

To simplify the problem further, we consider only ideal telescopes where the efficiency is independent of ω, $\vec{\sigma}$ and t and is given by:

$$\begin{aligned} \varepsilon &= 1, \quad E_l \le E \le E_u, \\ &= 0, \quad E < E_u,\ E > E_l. \end{aligned} \tag{4.7}$$

We will also assume a steady and homogeneous flux, where the energy and angular behavior are independent, such that the flux term will become:

$$\Phi(E,\omega) = \Phi(E)F(\omega), \tag{4.8}$$

then Eq. 4.6 becomes

$$C = \left(\int_\Omega d\omega \int_S d\vec{\sigma} \cdot \hat{r} F(\omega) \right) I \tag{4.9}$$

where

$$I = \int_{E_l}^{E_u} dE \Phi(E). \tag{4.10}$$

The expression between parenthesis in Eq. 4.9 is the gathering power of the telescope when the intensity has an angular dependence given by $F(\omega)$. That is

$$\Gamma = \int_\Omega d\omega \int_S d\vec{\sigma} \cdot \hat{r} F(\omega) = \int_\Omega d\omega F(\omega) \int_S d\vec{\sigma} \cdot \hat{r}. \tag{4.11}$$

Considering Eq. 4.11 again we see that if the intensity is isotropic then $F(\omega)$ is unity and the geometrical factor (the gathering power for isotropic flux) depends only on the geometry of the telescope. In other words:

$$G = \int_\Omega d\omega \int_S d\vec{\sigma} \cdot \hat{r}. \tag{4.12}$$

If we generalize slightly Eq. 4.9 reintroducing an energy dependent efficiency of the detector we get the expression

$$C = \int_{E_l}^{E_u} dE \Phi(E) \left(\varepsilon(E) \int_\Omega d\omega \int_S d\vec{\sigma} \cdot \hat{r} F(\omega) \right) = \int_{E_l}^{E_u} dE \Phi(E) A_{eff}(E) \tag{4.13}$$

The quantity in parentheses, that contain all the detector dependent properties, is called *acceptance* of the telescope. The evaluation of this function is of crucial importance to perform a measurement of flux. As we saw in Eq. 4.3 is this function indeed that contains all the detector properties that allows for a full derivation of the physical differential flux from the counting rate.

Single plane detector

For an ideal telescope comprising a single planar detector (refer to Fig. 4.1), the geometric factor is readily derived from Eq. 4.12 as:

$$G = \int_\Omega d\omega \int_S d\vec{\sigma} \cdot \hat{r} = \int_\Omega \int_S cos\theta d\sigma d\omega = 2\pi A \int_0^1 cos\theta d cos\theta = \pi A \tag{4.14}$$

In this context, Ω represents a full hemisphere (assuming particles are incident from only one side), and $A = \int_S d\sigma$ denotes the detector's surface area. Consequently, the geometric factor for a single planar detector of area A is simply

$$G = \pi A. \tag{4.15}$$

If particles are incident from both sides, the effective area doubles to include both the top and bottom surfaces.

The procedure applied in Eq. 4.14 is valid for single plane detectors of any shape for which exists a tangent plane in any given point. This means that it applies not only to flat surfaces, but also at any cylinder or sphere.

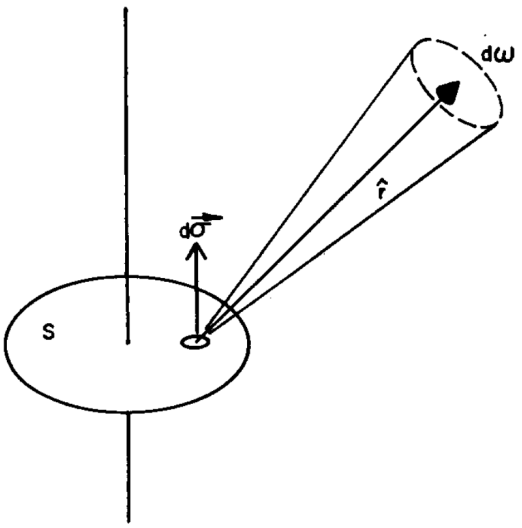

Figure 4.1: Schema of a telescope made of a single detector plane viewing one hemisphere. Picture from [107].

4.2.2 Monte Carlo estimation of geometric acceptance

The analytical derivation of the acceptance of a detector that is slightly more complex than a basic telescope is an extremely difficult task. In most cases the best way to get an accurate estimation is using numerical approaches based on Monte Carlo methods.

The basis of this technique is the definition of the geometric acceptance as the factor of proportionality between the incident isotropic flux and the observed events counting rate. The most general procedure exploits the simulation of an isotropic flux that irradiates the detector and consist on the counting of the relative number of events that are accepted with respect with those simulated, renormalizing this ratio to the known acceptance of the generation surface.

The strategy start from the definition of a source surface that is expected to cover the whole field of view of the detector. From the generation surface, the procedures iterates the following steps:

1. choose a random point on the source surface and a random trajectory through this point;

2. follow this trajectory and check if it passes through the detectors of interest;

3. repeat steps 1-2 enough times to let a statistical pattern emerge.

The geometrical factor for the telescope is then given by

$$G = \frac{N_{sel}}{N_{gen}} \times G_{gen} \tag{4.16}$$

Where N_{gen} is the total number of generated events, N_{sel} is the number of accepted, and G_{gen} is geometrical factor of the source surface.

During the simulation of the events is important to ensure that equal areas of the source surface weight equally in the generation of particles. The same goes for the generation of the directions of particles: any unit of solid angle should weight the same.

If the generated directions are weighted according to the angular dependence of the flux $F(\omega)$ then the Eq. 4.16 will produce the gathering power of the telescope instead of its geometric factor.

4.2.3 Acceptance estimation

Eq. 4.3 requires, for the determination of the CR flux from experimental results, to evaluate the effective acceptance A_{eff} of the employed detector. We introduced an analytical expression for this quantity in Eq. 4.13, but as we saw for the geometric acceptance, it is not any easy task to evaluate analytically such expression for realistically complex detectors. For this reason, also for the effective acceptance, Monte Carlo simulations are the most common solutions to approach the evaluation.

It's important to highlight how the element that differentiate $A_{eff}(E)$ from G is the inclusion of the detection efficiency $\varepsilon(E)$. This element incorporates, not only the intrinsic efficiency of the detectors, but also the efficiency of selections applied to events in order to grant good quality of reconstruction, separation from a background or any other selection needed to properly reconstruct the event. These efficiencies are in general dependent at least on the particle species studied and their energy.

To properly evaluate such quantity simulation must take into consideration, not only purely geometric properties, but also the physical interactions of studied particles with the detector, every possible source of background and an extremely detailed reproduction of the reconstruction process that lead to the measured data. For this goal simulation frameworks like Geant4 [108] serve an essential role. This kind of software allows the detailed definition of the geometry and composition of a realistic detector and generate a user-defined flux of randomized particles simulating their motion, interactions with the detector's components and the generation of secondary particles that keep propagating. All this while recording all the relevant information about the process in order to analyze statistical properties when a enough data have been collected.

4.3 HERD geometry

For the work we used one of the detector geometries proposed for the HERD experiment. The specific geometry is slightly different from the definitive one that was illustrated in chapter 2, but is based on a previous design. The main difference is the internal tracker: instead of the Silicon TracKer (STK) we used the FIber Tracker (FIT). This alternative sub-detector was supposed to have five modules to be installed on every side of the calorimeter, each composed by 7 tracking planes of scintillating fibers in hodoscopic configuration.

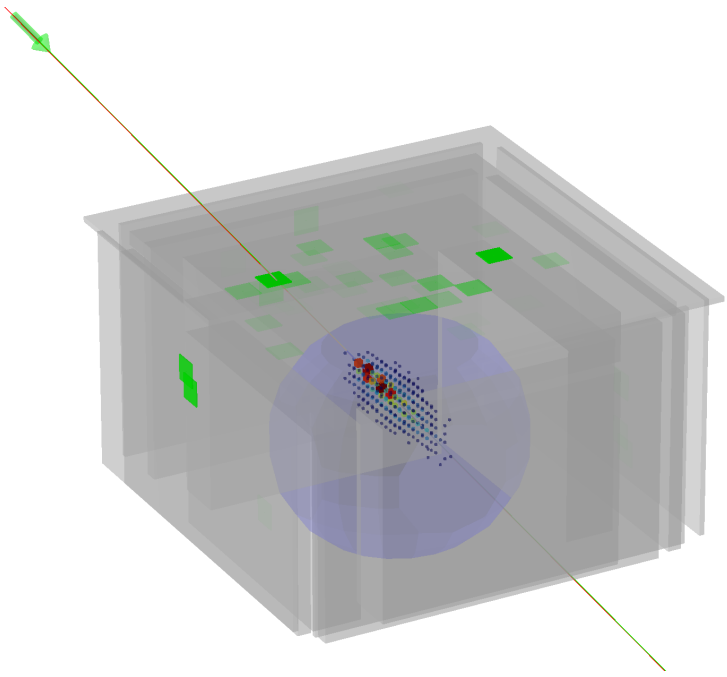

Figure 4.2: Event display from the HERD collaboration software showing a particle crossing the outer detectors and entering the calorimeter. In order to have a full reconstruction of the event the particle must cross at least a few layers of the tracker and produce a shower well contained in the calorimeter.

Cut	frequency	percentage	G [m^2 sr]
Total	7381450	100%	
POLAR	234506	3.18%	8.70
CALO0	151612	2.05%	5.63
CALO1	126778	1.72%	4.70
CALO2	103633	1.40%	3.85
CALO3	64340	0.87%	2.39
SCD1	57561	0.78%	2.14
SCD2	57533	0.78%	2.13
SCD4	57301	0.78%	2.13

Table 4.1: Accepted events based on different level of selection to ensures good reconstruction of the properties of incoming particles.

4.3.1 HERD acceptance

The analytical calculation of the gathering power and acceptance of such detector design is not trivial, but we can use computational solution to evaluate it.

We used the simulation provided by the HERD collaboration, based on Geant4 [108], to simulate an isotropic flux of non-interacting particles and rejected those that would be blocked Earth's shielding. This condition is expressed as a selection on the polar angle requiring it to be less than 112°. These particles are originated randomly from a spherical surface that surround the instrument, with a random direction of motion and can only move in a straight line and eventually cross a volume of the detector.

In order to obtain the gathering power of our experiment we need to count what fraction of events ends up in regions of the detector that ensures proper reconstruction of the event. This means that we need to define some constraints on the path of the particles that can ensures the measurement of the main properties.

First of all, it is crucial for the reconstruction to have a shower in calorimeter. The particle must at least cross the calorimeter volume, but for a good energy measurement the shower needs to be well contained in the calorimeter: if the intersection is too near to the edge the shower could not even start and for sure the energy reconstructed would be extremely poor. So we must ask for the particle to cross not any part of the CALO, but at least an inner fiducial volume. We defined this constraint selecting the events for which the length of the intersection between the trajectory and the CALO volume was greater than a minimum value.

Table 4.1 shows values obtained from the selection of the simulated events on the basis of the intersection length in the CALO: $CALO0$ are the events that have an intersection > 0; $CALO10$ are the events for which the intersection is greater than 10 X_0, $CALO20$ those whose interaction is greater than 20 X_0 and $CALO30$ those with an intersection larger than 30 X_0.

The calorimeter shower is not the only relevant interaction for the event reconstruction. Track and charge measurement are also very important. In table 4.1 are also

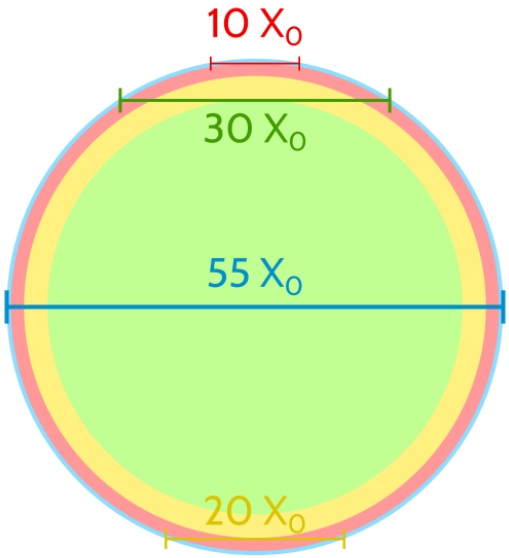

Figure 4.3: The diagram depicts the fiducial volume in the spherical CALO associated with the three cuts on minimum intersection length of the trajectory.

indicated the fraction of event that barely touch a plane of the SCD ($SCD1$), that traverse at least 2 layers ($SCD2$) and that interact with at least 4 layers of the SCD ($SCD4$). These conditions are preliminary chosen as reference of minimal requirements to reconstruct a track of the event.

Using equation 4.16 we can estimate the geometric factor of the HERD design. The generation surface used in the simulation was a sphere with radius 2.63 m, big enough to contain the whole instrument, while not being too large to waste resources simulating many particles not even crossing the detector. As per Eq. 4.15 the geometric factor of such surface is π times its area, thus the detector's geometric factor is

$$G = 4\pi^2 2.63^2 m^2 sr \cdot \frac{N_{sel}}{N_{gen}}. \tag{4.17}$$

The values that we got for different level of selection are reported in table 4.1. These values don't take into consideration the peculiarities of a proton or electron reconstruction in HERD and any additional efficiency to be factored in, but we don't expect order of magnitude variations. Comparing these numbers with the acceptance achieved by DAMPE [65], i.e. 0.3 m^2 sr for electrons and 0.1 m^2 sr for protons, it's evident the improvement in gathering power of the new design.

4.4 Signal identification

The main difficulty when studying the electron+positron flux in CRs is dealing with how low the rate is when compared with the extremely high background of protons and other nuclei. See Fig. 1.1 for the comparison of CR spectra. Charge measurement enables the efficient cut of any particle with $|Z| \neq 1$, leaving protons and anti-protons as the only residual background for $e^{\pm}$. However, at 1 TeV, protons are more than 10^3 times more abundant than electrons and this ratio becomes even higher at higher energies, due to the different slope of the spectra. For this reason it is crucial to have powerful discrimination tools that can accurately identify the proton background to be removed from the data, without losing too many electrons due to any misidentification.

One positive note, that help this background reduction, is that, because hadronic showers have a relevant fraction of invisible energy (see Sec. 3.1.2) and a higher leakage than EM showers, events generated by a proton will deposit significantly less energy than an electron of the same kinetic energy. Vice versa, when comparing events according to their deposited energy we'll compare electrons with protons of higher kinetic energy. The simulation on the HERD detectors shows a that protons almost never deposit more than half their kinetic energy, while electrons deposit about 84%. Since the proton spectrum is decreasing as $E^{-2.7}$, while the electron one as about E^{-3}, the observed protons to electrons ratio becomes

$$\frac{\Phi_p^{dep}(E)}{\Phi_e^{dep}(E)} = \frac{\Phi_p(E/0.5)}{\Phi_e(E/0.84)} = \frac{\Phi_p(E)0.5^{2.7}}{\Phi_e(E)0.84^3} \simeq \frac{\Phi_p(E)}{\Phi_e(E)}0.26 \tag{4.18}$$

The ultimate goal of background rejection is to reduce background intensity until its associated uncertainty becomes negligible compared to non-removable sources. For CR flux estimation, these primary uncertainties arise from statistical signal fluctuations and systematic errors in acceptance evaluation. The latter depends on the fidelity of detector simulations in reproducing instrumental effects that range from particle interactions to electronic readouts, and is influenced by geometric features, event selection efficiency, and detector calibration. Generally, redundancy within detection systems improves these uncertainties by providing independent cross-checks, allowing for a more precise validation of simulated values. Nevertheless, relative uncertainty for direct CR detectors typically remains, at best, on the percent scale, even for sophisticated instruments with extensive cross-measurements like AMS-02.

4.4.1 Background contamination

The standard approach to remove a background from the detected events is based on the definition of one or more parameters that assume different values if the event is a signal or if it is background. These parameters are called *discrimination parameters* or *discriminators* and, ideally, if the distribution of their values for signal events is completely separated from that of background events, they can be used to readily identify the event and discard the background. In most practical cases, it exists an overlap between the distribution of signal and background values. In these cases the selection

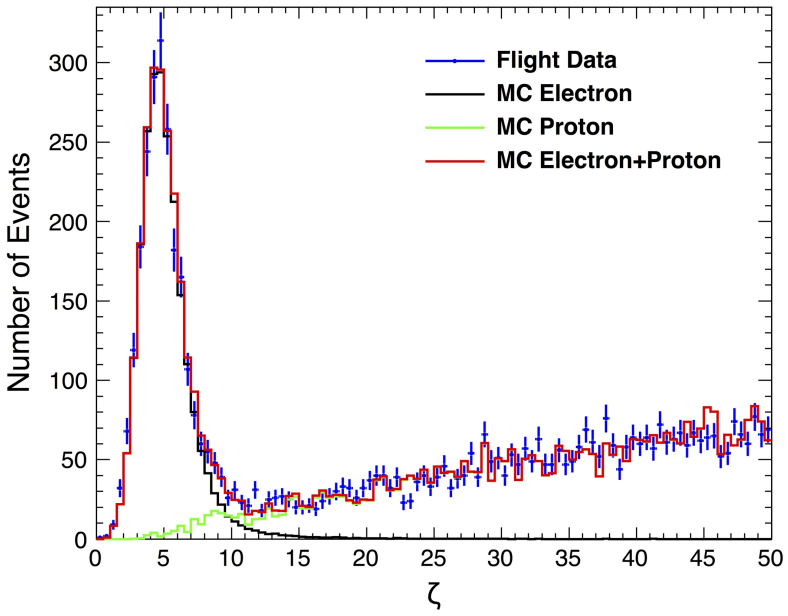

Figure 4.4: [109]

is based on the choice of a threshold value for such discriminators that will provide the best compromise between accepting a residual background and loosing some signal events. Fig. 4.4 shows the example of the distribution of a discrimination parameter used for the identification of electrons by DAMPE [109]. Selecting only the event with $\zeta < 10$ will remove almost all background while losing only few signals.

When the residual background is not negligible, in order to have the best estimation of the signal, it's necessary to quantify as accurately as possible the background that is not contaminating the accepted events. A powerful strategy to do so is based on the so-called *template fit*. This technique leverages the knowledge of the distributions of the discrimination parameter for signals and background events to estimate the relative abundance of the two components in a mixed dataset. If it's known that the discriminator λ follows the distribution $f_{sig}(\lambda)$ for signals and $f_{bkg}(\lambda)$ for the background, then we can fit the histogram that describe the distribution of the values of λ for the studied dataset with the composite function

$$N_{sig} f_{sig}(\lambda) + N_{bkg} f_{bkg}(\lambda) \tag{4.19}$$

to evaluate the abundance of signals N_{sig} and that of background N_{bkg}.

This approach is very powerful because, even if the background is extremely more abundant than the signal, the uncertainty on the signal estimation only depends on the overlap between the two distribution, and in particular is compatible with the combination of the statistical Poisson error on the signal counting and the statistical Poisson error on the counting of the residual background.

To better understand this mechanics we'll make use of a Monte Carlo toy simulation

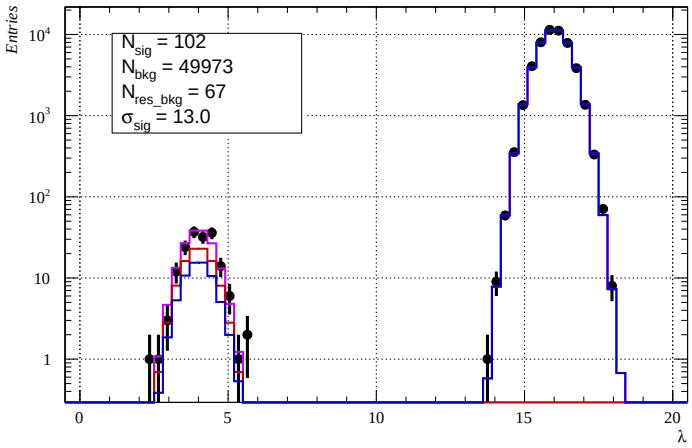

Figure 4.5: Example of template fit performed on the distribution of a discrimination variable λ for a dataset with background overlapping with signal. The black dots represent the distribution of the observed λ, while the purple line is the combination of the signal and background components as obtained from the fit.

as an example. We simulated 2 populations, a signal and background, with known distribution of the discrimination parameter λ. For signal λ follows a Gaussian distribution centered on 4. For backgrounds most events follows a Gaussian centered on 16, while 0.135% of events behave exactly like signals. We simulated a random flux with expected signal counts $N_{sig} = 102$ and expected background counts $N_{bkg} = 5 \times 10^4$. The black dots in Fig. 4.5 depicts the distribution of λ for the simulated dataset containing both signal and background events. The purple line represents the result of the template fit on the dataset. In this example the background that contaminates signals amounts to $49973 * 0.00135 = 67$, while the signal itself counts 94 events. The uncertainty on the signal that we get from the fit is compatible with the sum in quadrature of the Poisson error on signal and residual background $\sqrt{N_{sig} + N_{res\_bkg}} = 13.0$.

These observations hold under the assumption of perfectly knowing the typical distribution of the discriminator for signals and backgrounds, but usually we can only characterize these distributions thanks to simulations. The limited accuracy of such simulation add systematic uncertainty to the signal estimation that we can perform even with the more sophisticated fit.

4.5 Uncertainty estimation

Putting the pieces together we can produce some estimation of the uncertainty for the $e^{\pm}$ flux that we could perform with HERD. We'll consider as main sources of uncertainty the signal counting, comprensive of the background contamination, and the systematics from the acceptance. We'll use this results to evaluate a goal for the discrimination power

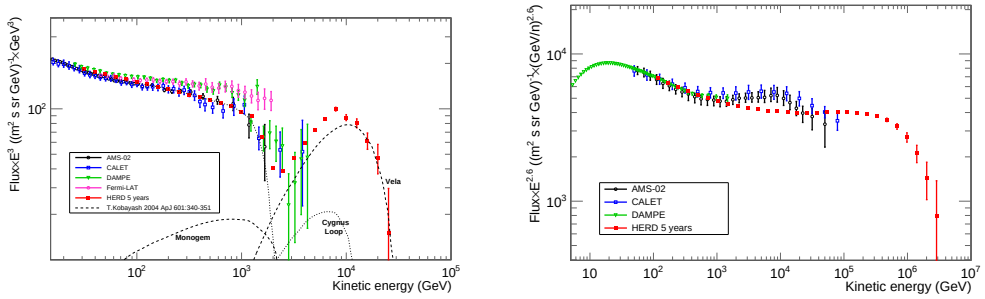

Figure 4.6: In red, the expected flux for electrons and protons assuming a local source of $e^{\pm}$ from the Vela pulsar. These spectra were used to estimate the expected signal and background counts.

of the algorithm that we'll describe in the next chapter.

To estimate the counting rate of electrons and protons we exploited the expected fluxes depicted in Fig. 4.6. These spectra are forecasts produced taking into consideration a local source of $e^{\pm}$ from the Vela pulsar [110], together with current experimental data from space and ground CR detectors.

The spectra were used to weight the simulation of a dataset of electron and proton events in such a way that the number of events per E_0 bin would match the expected events after 5 years of exposure for a detector with the acceptance that we estimated for HERD. The simulated data were then reported with respect to their total deposited energy in the CALO. Fig. 4.7 shows the distribution of the expected number of electrons and protons.

These numbers were than used to evaluate the expected uncertainty on the signal measurement. To do so, we need to assume the signal efficiency and bacjground contamination of the discrimination technique that we'll use. As signal efficiency we considered 0.9, while for background contamination we compared the case 10^{-3} and 10^{-4}. These values are compatible with performance that we'll see in the next chapters.

Figure 4.8 shows the expected uncertainty on the flux of electrons after 5 years of exposure of the HERD instrument. The statistical uncertainty on the signal is evaluated as the ratio between the squared root of the expected event count and the count itself and is shown in the picture by the red line. For the statistical uncertainty on the background contamination too, we used the ratio between the squared root of the expected background count and the signal count. These values are shown as the blue line.

The systematic relative uncertainty on the acceptance has been assumed as a constant 0.02 as this is the value achieved by AMS-02 in this energy range [111]. Since HERD won't achieve the same level of redundancy in the measurements as AMS-02, we expect this value to be an overestimation of precision.

The comparison shows that even with a contamination reduced to only 10^{-3} the systematic uncertainty on acceptance and the signal statistics dominate up to about 10 TeV. Only at higher deposited energies the uncertainty generated by the background

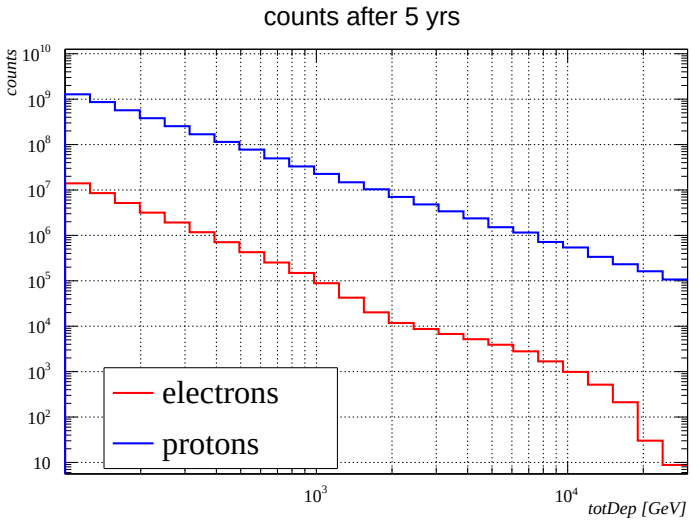

Figure 4.7: Expected event counts for electrons (red) and protons (blue) after 5 years of exposure of the HERD instrument.

contamination start becoming dominant. For a contamination at 10^{-4} this contribution is negligible up to about 20 TeV. For a 5 years exposure, at these energies the relative uncertainty from the electrons statistics is already over 20%, so a background reduction to 10^{-4} is enough to achieve optimal performance.

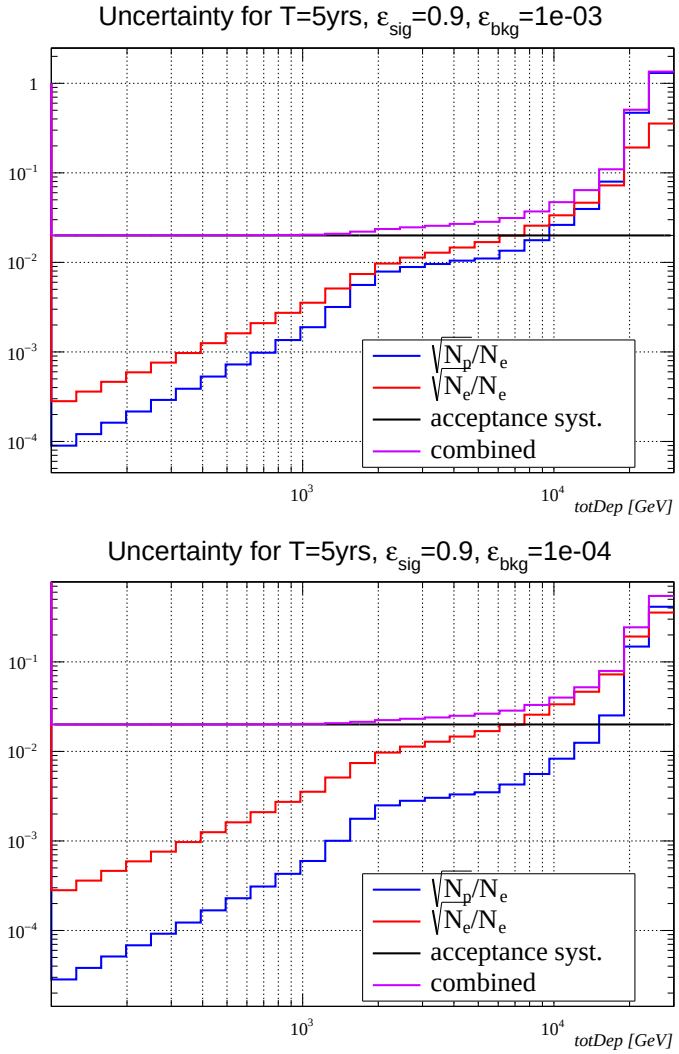

Figure 4.8: The two plots show the main contributions to flux uncertainty for the case of 10^{-3} and 10^{-4} background contamination. The black line is the systematic uncertainty associated to acceptance estimation for a typical CR instrument. The red line describes the relative uncertainty on signal events counting, while the blue one is the relative uncertainty from the residual background contamination on the signal measurement. The purple line shows the combination of the three. Both plots are computed for the HERD facility design after 5 years of exposure with a 90% signal efficiency. The top picture considers background contamination as 10^{-3}, while the bottom one as 10^{-4}.

Chapter 5

Particle ID with 3D calorimeters

This chapter describes the main goal of this work, and the details of the analysis technique that was developed to achieve it. Within the whole chapter the word *electron* will be used to mean both electrons and positrons. Likewise, *proton* will mean both protons and antiprotons.

5.1 Goal of the analysis

The goal of the project is to exploit the unique reconstruction capabilities of a 3D segmented calorimeter to develop a tool capable of identifying electrons in an environment strongly dominated by protons, like that of cosmic rays. This discriminator should achieve good performances for any arrival direction and even at high energy, featuring enough separation power to achieve a contained statistical and systematic uncertainty in the electron flux measurement up to 10 TeV. In particular, on the base on the conclusions of the previous chapter, to have a negligible contribution to signal uncertainty from the background up to tens of TeV we'll need to have a background reduction on the order of 10^4.

5.1.1 Likelihood

To build this e/p discriminator we'll focus on assembling a statistically backed approach like a Likelihood test, instead of a black-box solution like a machine learning approach.

The likelihood is a statistical metric that quantifies the compatibility of a set of measurements with a hypothesis of known statistical behaviour. In particular the statistical behaviour is defined through the Probability Density Function (PDF) of the measured properties x, that is the function $f(x)$ such as the probability of measuring x in the interval $[x_A, x_B]$ is

$$P(x_A, x_B) = \int_{x_A}^{x_B} f(x')dx'. \tag{5.1}$$

This figure can be used to discriminate between two or more hypotheses, if the PDF of the measured properties depend on the tested hypothesis ($\mathcal{H}$).

Let's assume we have a set of N independent measurements $X = \{x_i\}_{i=1}^{N}$ for a certain observable. If we expect the observable to follow the PDF $f(x|\mathcal{H})$ in case of $\mathcal{H} = true$, we define the likelihood L of $\mathcal{H}$ based on the measurements X as

$$\mathcal{L}(\mathcal{H}|X) = \prod_{i=1}^{N} f(x_i|\mathcal{H}) \tag{5.2}$$

The higher the likelihood value, the more compatible the hypothesis is with the measurements.

When we acquire a particle shower in the calorimeter, each cube will record an energy deposit measurement. If the PDF for the energy deposit by electrons in each cube is known, we can combine the measurement from each of the cubes to evaluate the likelihood of *electroness* for the event. Since we expect different particle species to produce different likelihood values, based on the differences between EM and hadronic sohwers discussed in previous chapters, this means that we can use the likelihood as a discrimination parameter to identify electrons among protons. When testing protons with the typical PDF of electrons we expect to obtain probability density values lower than those obtained testing electrons, so also the resultant likelihood for protons will be lower than that of electrons. If the values are separated enough we can use this value to tell the two species apart.

Since charge detectors can efficiently select the events with charge $|Z| = 1$, the only background for electrons are protons and, therefore, the discrimination of electrons is a test of two simple hypotheses: electrons or protons For this class of tests the Neyman-Pearson lemma[112] states that the most powerful test of the electron hypothesis $\mathcal{H}_e$ against the proton hypothesis $\mathcal{H}_p$ based on the observation X is the likelihood ratio

$$\Lambda(\mathcal{H}_e : \mathcal{H}_p|X) = \frac{\mathcal{L}(\mathcal{H}_e|X)}{\mathcal{L}(\mathcal{H}_p|X)} \tag{5.3}$$

This means that, in order to get the best discrimination possible, we will need to obtain a PDF for both the electron and proton hypotheses. This is not an easy task for neither one nor the other species, because of the complexity of the underlying processes involved. The fluctations observed in each measurement are the result of the several interactions that sustain the cascade shower, but also depend on the geometry of the cubes that sample the shower, the scintillation of the cube itself and the response of the readout sensors used. They'll depend on the region of the shower sampled but also on the energy of the primary. To characterize such behaviour we'll rely on simulation tools that will help us have a picture as complete as possible.

5.2 Preliminary phase

5.2.1 Computing tools

All the simulations and analyses were performed on INFN machines managed by CNAF[113] in Bologna or RECAS[114] in Bari. Simulations were performed by the HERD collaboration[115] using GGS[116], a simulation tool based on Geant4[108] (see Sec. 4.2.2) for

small to medium size particle physics experiments. The data were analyzed using the EventAnalysis[117], a framework for data analysis that enables the processing of dataset through modular algorithms that can be sequenced in complex analysis pipelines. The algorithms used were a combination of libraries provided by the HERD collaboration together with custom-built one that were developed ad-hoc for the purpose of this work. The whole process made extensive use of ROOT libraries[118], a collection of computing tools for data handling and statistical analysis developed by CERN.

5.2.2 Simulation

Geometry

The detector geometry used for the simulations was based on one of the designs proposed for the HERD experiment. In particular, instead of the currently adopted design, we used a slightly older one that employs the spherical CALOrimeter, the long bar version of the PSD and the FIT tracker instead of the STK. Even though only the calorimeter data were used for the analysis all the other sub-detectors were included in the simulation in order to account for fragmentation in the detector materials and other kind of interactions ongoing before the entrance in the CALO. Since interactions and secondary particles may generate additional showers in the calorimeter, or introduce artificial features in the calorimeter shower properties, this allows to train and test the algorithm on a signal sample that is most representative of that expected in the data that will be collected by the instrument. The used configuration is depicted in Fig. 2.2.

The cubes employed for the simulation of the CALO feature 3 cm edge, are made in LYSO, and are placed with a 4 mm interspace that was filled with carbon to simulate the supports and electronics contributions.

Events

We simulated a dataset of electrons and one of protons impinging on the instrument. Both of these were generated following an energy spectrum with the shape E^{-1}. Despite not being the actual physical spectrum of neither electrons nor protons, the events can be weighted in order to obtain realistic distributions based on the currently available spectrum measurement from operating CR detectors. One of the benefit of the choice of this expedient that makes use of a less steep power-law energy dependence of the generated fluxes is that the more energetic events are less rare than in reality, making it easier to have significant statistics at the upper end of the spectrum. As an additional feature, the E^{-1} distribution is also handy because the events become uniformly distributed when binned in logarithmic scale.

The simulated particles were generated from a spherical source of radius 2.63 m, centred at the center of the CALO, the same surface used for the acceptance study described in chapter 4. The particles were generated with random inward directions, uniformly distributed in azimuth and polar angle. Only particles crossing the CALO for an amount > 0 of X_0 have been kept for analysis, since other particles are not expected to

generate a significant amount of energy deposit in the calorimeter, and will be excluded from analysis by preliminary selections. It is worth to mention that a specific study is needed during data analysis in order to verify the possible contribution of sample contamination by CALO showers generated by secondary particles from interactions, that may mimic a signal event. These events are not studied in the context of this work.

In order to have enough longitudinal and lateral containment and therefore good quality of reconstruction for the showers, we performed a further selection of the events based on the length of the intersection between the longitudinal direction and the CALO volume. This longitudinal direction is based on the MC direction of the primary for the construction of the model, but exploit a reconstructed direction when testing events. In particular, we selected events with an intersection length greater than 30 X_0. This value was chosen on the base of a previous study performed by the HERD collaboration on the same dataset[115] as the minimum cut that offer the optimal energy resolution up to 10 TeV. In a spherical calorimeter this ensures, not only longitudinal containment, but also some lateral distance from the CALO external surface and therefore a more complete 3D containment of the shower.

The simulated electrons that interact with CALO, between 100 GeV and 20 TeV, are about 2 million, while the simulated protons, between 100 GeV and 100 TeV, almost 4.5 million. Only about half them have an intersection larger than 30 X_0. The exact numbers are reported in Table 5.1.

Species	**Energy range**	**CALO**	**30 X_0**
electrons	[100 GeV, 1 TeV]	0.891 M	0.450 M
electrons	[1 TeV, 20 TeV]	1.15 M	0.579 M
protons	[100 GeV, 1 TeV]	1.52 M	0.849 M
protons	[1 TeV, 10 TeV]	1.57 M	0.853 M
protons	[10 TeV, 100 TeV]	1.36 M	0.712 M

Table 5.1

The different energy segments have been simulated independently and don't perfectly match as one common E^{-1} spectrum. This means that we need to rescale the events based on the generation energy interval to get a continuous spectrum before performing any study on the distributions of these events.

The asymmetry in the energy range for electrons and protons is actually important to have reconstructed energy bins realistically populated in our range of interest. Indeed, unlike electrons, that generate regular well contained electromagnetic showers, protons showers extend on greater lengths, with a stronger variability in the starting point of the showers and involving a relevant quantity of quasi-non-interacting particles. This means that proton events will spread across a broad range of reconsructed energies always lower than their initial kinetic energy. Fig. 5.1 shows the distribution of deposited energy $totDep$ from protons of different initial kinetic energy E_0 compared to that of electrons. The ranges 100 GeV-20 TeV for electrons and 100 GeV-100 TeV for protons ensure a realistically populated 100 GeV-10 TeV range in reconstructed energy for both particle

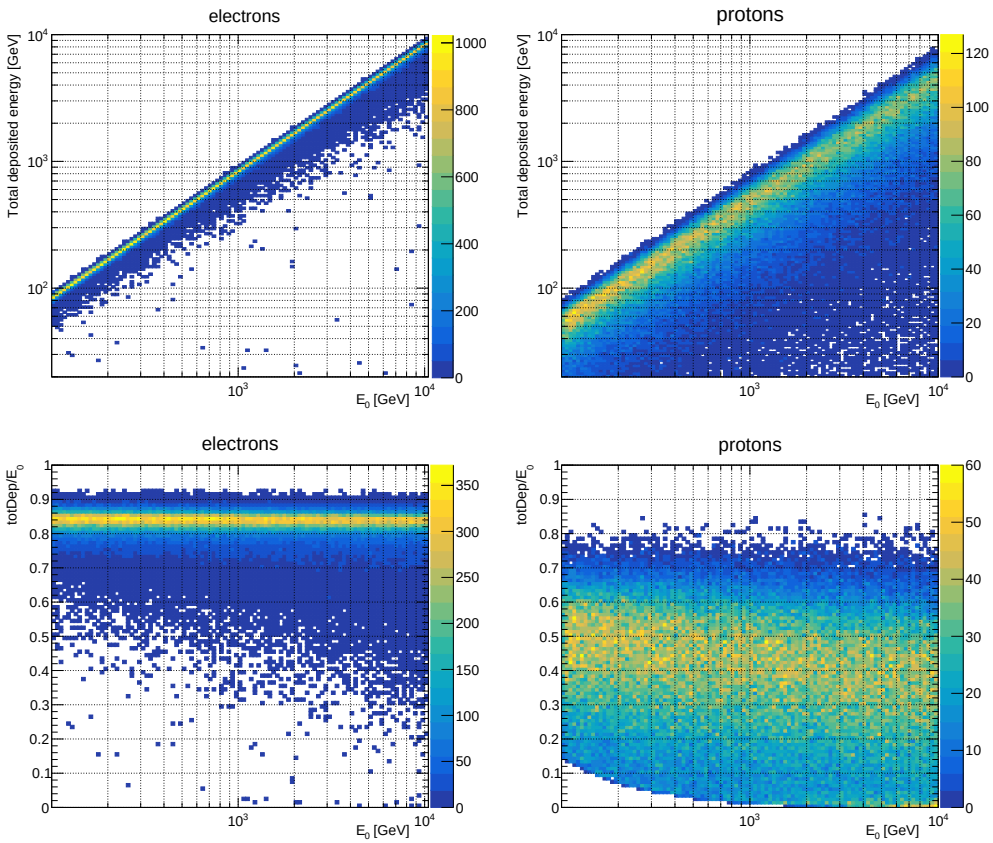

Figure 5.1: The two plots on top depict the distribution of the deposited energy in the calorimeter from electrons (left) and protons (right) with respect to the initial kinetic energy E_0 of the particle. The plots on the bottom show the fraction of initial kinetic energy that is deposited in the calorimeter wrt to E_0, again for electrons (left) and protons (right).

species.

Realistic energy deposits readout

To have a more realistic representation of the shower data compared to the MC information, we simulated the digitization of the digital signals performed by photodiodes installed on the LYSO cubes and the subsequent reconstruction of the energy values through calibration. This process accounts for critical instrumental effects, including electronic noise, light collection efficiency, and direct ionization within the photodiodes.

The conversion from energy to ADC channels is based on 2021 HERD beam test at CERN SPS. For the Large Photodiode (LPD), a Mean Ionizing Particle (MIP) signal corresponds to approximately 28 MeV, yielding a mean of 125 ± 32 ADC channels. For the Small Photodiode (SPD), which is insensitive to single MIPs, we adopted the flight-

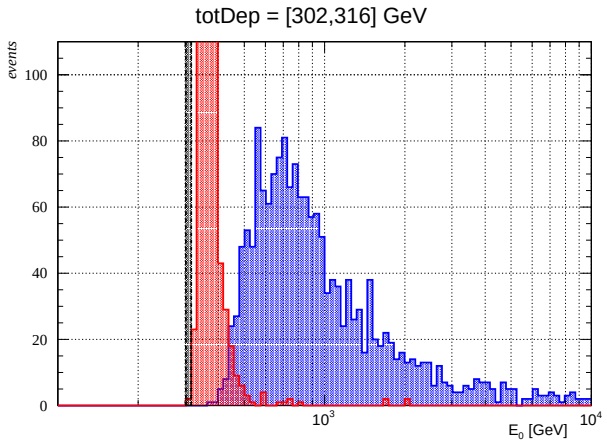

Figure 5.2: Composition of the reconstructed energy bin [302GeV, 316GeV] for protons (blue) and electrons (red) with respect to the initial kinetic energy of the primary particle. The black area identifies the boundaries of the *totDep* bin selected.

model (v2) design ratio of 1300 ± 20 to scale the LPD response. Direct ionization is modeled separately by calculating electron-hole pair production in silicon (3.8 MeV/cm) and processing the charge through the HiDRA ASIC response.

The digitization algorithm for each cube follows these steps:

1. convert scintillation and direct ionization energy to ADC channels,
2. sum the components and add the electronics pedestal (V_{ped}),
3. determine the gain regime (high/low) and account for saturation,
4. apply Gaussian electronic noise based on the active gain channel.

To emulate flight-model data constraints, a *zero suppression* threshold of $1.5\sigma_{noise}$ is applied to discard noise-only events. The final calibration step reverses the digitization to recover the energy in GeV. This procedure mimics the processing of real flight data: it subtracts the pedestal, accounts for gain ratios, and converts the total signal back to energy without attempting to disentangle the ionization and scintillation components. In the final analysis, the LPD signal is utilized unless saturated, at which point the system defaults to the SPD readout.

5.2.3 Data preparation

In order to highlight topological features of the showers the analysis was not based on the absolute xyz reference frame, but on a 2D reference frame based on the direction of development of each shower. This step is of fundamental importance to be able to compare every shower sample with the analogous sample of another shower. In a detector like HERD every event cross the CALO in different directions, so we cannot

simply compare showers in a layer by layer basis, but we need to rotate each event in a consistent frame.

For each shower we computed the main longitudinal axis using Principal Component Analysis (PCA), a data analys technique that identify the direction on which a multivariate distribution of data shows the largest variance from its center of gravity. Along this direction we determined the longitudinal coordinate t expressed in terms of radiation length X_0.

The second coordinate r was defined as the distance from the longitudinal axis in terms of Molière radius R_M. Since we expect to have a cylindrical symmetry, we don't need to introduce a third coordinate like an azimuthal angle θ.

Energy density

The measured value ε_i that we get from the photodiodes mounted on the cube i can be described as the integral, over the cube's volume of the deposited energy density function $f(x, y, z)$ that describe the spatial distribution of energy deposition in the calorimeter.

$$\varepsilon_i = \int_{x_i}^{x_i+\Delta x} \int_{y_i}^{y_i+\Delta y} \int_{z_i}^{z_i+\Delta z} f(x, y, z) dx dy dz \tag{5.4}$$

Approximating f as a step function that assumes in every cube the average value of f in the cube volume

$$\varepsilon_i = f(x, y, z)\Delta x \Delta y \Delta z \tag{5.5}$$

Now let's see how we can describe the observable ε_i with respect to the energy density defined in the (t, r, θ) reference frame. Let's start from assessing the change of coordinates for the particular case of $\hat{z} \parallel \hat{t}$

$$\begin{cases} t = z/X_0 \\ r = \sqrt{x^2 + y^2}/R_M \\ \theta = \tan^{-1}(y/x) \end{cases} \quad \begin{cases} dz = X_0 dt \\ dxdy = R_M^2 r dr d\theta \end{cases} \tag{5.6}$$

From

$$f(t, r, \theta) dt dr d\theta = f(x, y, z) dx dy dz \tag{5.7}$$

Using the coordinate substitution from Eq. 5.6

$$f(t, r, \theta) dt dr d\theta = f(x, y, z) r dr d\theta X_0 R_M^2 dt \tag{5.8}$$

$$f(t, r, \theta) = f(x, y, z) r X_0 R_M^2 \tag{5.9}$$

Substituting $f(x, y, z)$ from eq. 5.5 we get

$$f(t, r, \theta) = \frac{\varepsilon_i r X_0 R_M^2}{\Delta x \Delta y \Delta z} \tag{5.10}$$

Since we expect cylindrical symmetry, the integration on θ only introduce a factor 2π:

$$f(t,r) = \frac{\varepsilon_i r X_0 R_M^2}{\Delta x \Delta y \Delta z} 2\pi \tag{5.11}$$

Thanks to the expression in Eq. 5.11 we can use the measured energy deposits in the cubes to describe the energy density in the longitudinal-transversal reference frame.

5.3 Probability density function

The crucial part to evaluate a proper likelihood is to obtain a PDF for the energy deposit at a given t and r. For a given particle species this quantity will also depend on the particle initial energy. Unfortunately this function is not easily predicted by the theory or described by the experiments. In order to retrieve this $p(\varepsilon; t, r, E_0)$ we will have to test different kind of approximations.

5.3.1 A priori description

Deriving an a priori description of this PDF is a very challenging task. Rossi and Greisen put the basis for the modelling of showers in the 40s [98].

Let $N(E_0, t)$ be the total number of particles irrespective of energy which is found, on the average, at the thickness t when a primary particle of energy E_0 is incident at $t = 0$. If the shower particles were independent of each other, the probability $P(N)$ of N rather than $\bar{N}$ particles being present at t would be represented by the Poisson law

$$P(N) = \frac{e^{-\bar{N}}(\bar{N}^N)}{N!} \tag{5.12}$$

which gives for the mean square deviation from the average

$$V[N] = \langle (N - \bar{N})^2 \rangle = \langle N^2 \rangle - (\bar{N})^2 = \bar{N} \tag{5.13}$$

The particles of a shower, however, are not independent, since they arise from the same primary. Hence, the use of Eqs. 5.12 and 5.13 is not justified, although there are some reasons to believe that the Poisson distribution may be roughly valid at large thicknesses.

Furry [119] made an attempt to determine the function $P(N)$ using a simplified model for the shower phenomenon. In the Furry model the shower particles are considered to be all of the same nature and it is assumed that each particle traversing a thickness dt of matter has a definite probability, proportional to dt, of splitting into two equal particles. The collision loss is neglected. These assumptions lead to a value of $\bar{N}$ which increases exponentially with thickness, and to the following expressions for $P(N)$ and $V[N]$:

$$P(N) = \frac{1}{\bar{N}} \left[1 - \frac{1}{\bar{N}} \right]^{N-1} \tag{5.14}$$

$$V[N] = \bar{N}(\bar{N} - 1) \tag{5.15}$$

It is seen that according to the Furry model the fluctuations are much larger than those calculated from the Poisson formula. Indeed, the mean square deviation is approximately proportional to $\bar{N}^2$ rather than to $\bar{N}$. The most serious source of error in Furry's calculations arises from neglecting the collision loss. The effect of the collision loss becomes more and more noticeable with increasing thickness, as shown by the fact that the average number of shower particles $\bar{N}$ should pass through a maximum and then decrease again instead of increasing continuously as the Furry model would indicate. Therefore, we may expect Eqs. 5.14 and 5.15 to be approximately valid only for small thicknesses.

Nordsieck, Lamb, and Uhlenbeck [120] tackled the fluctuation problem from a more general standpoint, using again the Furry model but taking into account, at least roughly, the energy loss by collision. They did not reach any closed expression for $P(E)$ but were able to calculate some values for the mean square deviation. The quantity $\sigma = (\langle N^2 \rangle - (\bar{N})^2)/\bar{N}$ is 1 according to Poisson's formula, and $\bar{N} - 1$ according to Furry's formula.

Experimental results place the actual value between these two extremes. We can then conclude that the actual behaviour of the shower particles is somewhat intermediate between that predicted by the Poisson and Furry formulae.

All this work only focus on the fluctuations in the number of particles involved in the shower. The energy deposited by each particle is mostly loss via ionization. The fluctuation of this process is described by the Landau distribution. Once the energy of a particle reach a critical energy value E_c, the energy loss become order of magnitudes faster and the whole residual energy get deposited immediately.

Further contribution to the energy deposit fluctuation come from the variations in scintillation photons emission and in the photodiodes quantum efficiency, even if we expect these effect to be almost negligible. It is clear however that an accurate a priori modelling is extremely difficult to achieve. We'll necessarily need to rely on quite crude approximations.

5.3.2 Modified Poisson function approximation

Different attempts to describe a priori the local fluctuations in the number of shower particles failed to reach a definitive result. However, as we saw, at least in some cases, the behaviour should be in some way similar to that of a Poisson function. For this reason we explored the idea to use a parametric function based on a modification of a Poisson distribution.

One clear limitation in using the Poisson function out-of-the-box for energy deposit is that energy is not discrete, so we need to implement an extension of the function that work on continuous variables. In literature is possible to find different proposed extension.

Ilienko extension

The most formally rigorous is likely the one proposed by Ilienko in [121] that is defined through its cumulative distribution function (CDF) $F_\lambda(x)$ which is

$$F_\lambda(x) = \begin{cases} 0, & x \leq 0, \\ \dfrac{\Gamma(x,\lambda)}{\Gamma(x)}, & x > 0. \end{cases} \tag{5.16}$$

Here the function $\Gamma(x)$ is the Euler Γ-function, while $\Gamma(x,\lambda)$ is the Euler upper incomplete Γ-function

$$\Gamma(x,\lambda) \stackrel{\text{def}}{=} \int_\lambda^\infty e^{-t} t^{x-1} dt, \quad x > 0, \lambda \geq 0, \tag{5.17}$$

When $\lambda = 0$ we have the usual Γ-function. Using this extension actually presents several issues. The first one is that the PDF itself is not easily described by an analytical expression, so as a workaround we should rely on using a numerical derivative of the CDF. Another much more problematic issue is that this formulation does not provide an analytical estimate of the PDF moments, including its first order moment, i.e. the mean. This makes it extremely difficult to get the proper PDF from observed features like mean or variance of the energy deposits.

Naive extension

A more naive approach to generalize a Poisson distribution that we explored is based on the introduction of a factor η_n in the standard expression for Poisson fluctuations Eq. 5.12. The modified expression is

$$p(N|\bar{N},\eta_n) = \frac{e^{-\bar{N}/\eta_n}(\bar{N}/\eta_n)^{N/\eta_n}}{\eta_n\ \Gamma(N/\eta_n + 1)} \tag{5.18}$$

With this probability distribution we get as expected value and variance

$$E[N] = \bar{N} \quad V[N] = \bar{N}\eta_n \tag{5.19}$$

This means that varying the value of the parameter η_n the function can exactly overlap with a Poisson when $\eta_n = 1$, stretch broader if $\eta_n > 1$ or squeeze narrower if $0 < \eta_n < 1$. The results of Nordsieck and colleagues implies that this value of η_n should be contained between 1 and $\bar{N}$.

This expression is still referring to the number of particle in a sample of the shower, but the quantity that we are able to measure is a deposited energy. If we substitute N with $\eta_e\varepsilon$, where ε is the deposited energy and η_e is the average energy deposited by a particle, we get a PDF for the deposited energy. Of course, we are not accounting for the Landau distribution of the ionization loss, but we can try to encode that extra variability in a sort of effective parameter η. This η can be used to account for both

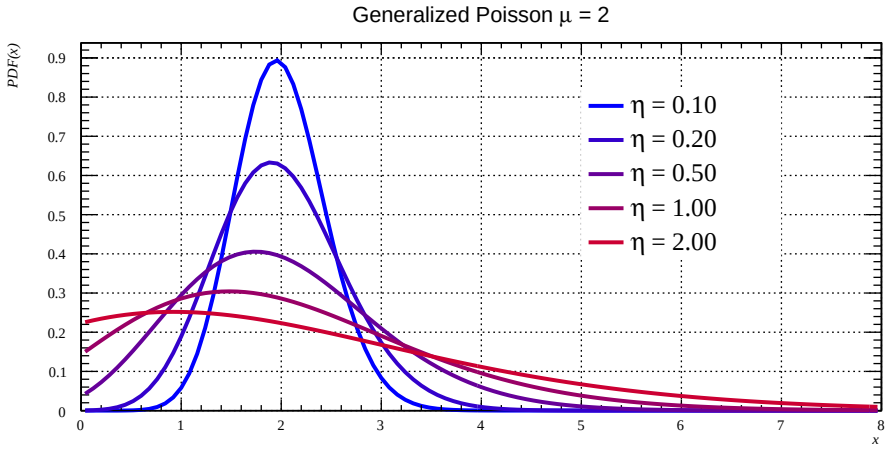

Figure 5.3: Plots of the modified Poisson function with mean 2 and variance that changes according to η.

the deviation from Poissonian distribution of the number, and the variation in energy deposit per particles.

$$p(\varepsilon|\bar{\varepsilon},\eta) = N(\bar{\varepsilon}/\eta)\frac{e^{-\bar{\varepsilon}/\eta}(\bar{\varepsilon}/\eta)^{\varepsilon/\eta}}{\eta\,\Gamma(\varepsilon/\eta+1)} \tag{5.20}$$

The introduction of this degree of freedom gives extra flexibility to the function. In particular, while the Poisson function is bound to have the variance always equal to the mean, in the modified version we can set independently mean and variance. This means that if we manage to model the average energy deposition density and the variance of the energy deposition density we can combine this information to obtain a PDF.

5.3.3 Generalized Laguerre polynomials approximation

A different possible approach is to relax the hypothesis on a specific function shape and rely instead more on measured properties to approximate the actual function. A strategy that we tested is to describe the PDF as a sum of generalized Laguerre polynomials, choosing coefficients of the sum such that the moments of the sum are the same as those measured.

The n^{th} moment of a real-valued continuous random variable with density function $f(x)$ about a value c is the integral

$$\mu_n = \int_{\infty}^{\infty}(x-c)^n f(x)dx \tag{5.21}$$

If the mean is used as the value of c this is called n^{th} central moment.

Particularly useful for our case is the case in which $c = 0$.

$$\mu'_n = \int_{\infty}^{\infty} x^n f(x)dx \tag{5.22}$$

This particular instance is called n^{th} raw moment and indicated with a superscript.

The first raw moment μ'_1 is the mean of the distribution, while the second central moment μ_2 is the variance.

The task of determining a probability distribution from the values of its moments is called problem of moments. An approximate numerical solution for positive random variables has been described by Wilson and Wragg in 1972 [122] employing generalized Laguerre polynomials.

The generalized Laguerre polynomials $L_n^\alpha(x)$, $\alpha > -1$, $0 \leq x < \infty$, are defined by

$$L_n^\alpha(x) = \sum_{i=0}^{\infty} \binom{n+\alpha}{n-i} \frac{(-x)^i}{i!} \tag{5.23}$$

and they satisfy the orthogonality condition

$$\int_0^\infty L_n^\alpha(x) L_m^\alpha(x) x^\alpha e^{-x} dx = \frac{\Gamma(n+\alpha+1)}{\Gamma(n+1)} \delta_{m,n} \tag{5.24}$$

over the interval $[0, \infty)$, where $\Gamma(x)$ is the gamma function and $\delta_{m,n}$ is the Kronecker delta function. We assume that the probability density function $f(x)$ can be expanded formally as an infinite series of generalized Laguerre polynomials, that is,

$$f(x) = \frac{a^{\alpha+1}}{\Gamma(\alpha+1)} x^\alpha e^{-ax} \sum_{k=0}^{\infty} c_k L_k^\alpha(ax) \tag{5.25}$$

where $a > 0$ is a scaling factor. In order to ensure that the fitted distribution has its first and second moments equal to μ'_1 and μ'_2 respectively, two integral conditions are required and hence the parameters a and α are chosen so that

$$\alpha = \frac{2(\mu'_1)^2 - \mu'_2}{\mu'_2 - (\mu'_1)^2}, \quad a = \frac{\mu'_1}{\mu'_2 - (\mu'_1)^2} \tag{5.26}$$

If, for each moment μ'_i, we introduce the function q_i defined by

$$q_i = a^i \frac{\Gamma(\alpha+1)}{\Gamma(i+\alpha+1)} \mu'_i \tag{5.27}$$

then from definition in Eq. 5.22 and expansion in Eq. 5.25 we have

$$q_i = \int_0^\infty \frac{y^i}{\Gamma(i+\alpha+1)} \sum_{k=0}^{\infty} c_k L_k^\alpha(y) y^\alpha e^{-y} dy \tag{5.28}$$

But $y^i/\Gamma(i+\alpha+1)$ can be expressed in terms of a finite generalized Laguerre series, namely $\sum_{k=0}^{i} b_k L_k^\alpha(y)$, where the coefficients b_k are given by

$$b_k = \frac{(-1)^k \Gamma(k+1)}{\Gamma(k+\alpha+1)} \binom{i}{k} \tag{5.29}$$

This leads to the following relations for the coefficients c_k,

$$q_i = \sum_{k=0}^{\infty} (-1)^k \binom{i}{k} c_k, \quad i = 0, 1, 2, \ldots \tag{5.30}$$

The function q_i can be expanded in a Newton-Gregory series of the form

$$q_i = \sum_{k=0}^{\infty} \Delta^k q_0 \binom{i}{k} \tag{5.31}$$

and thus the coefficients c_k of the generalized Laguerre series in Eq. 5.25 are related to the forward differences of q_0 by

$$c_k = (-1)^k \Delta^k q_0 \tag{5.32}$$

The parameters a and α are evaluated numerically from Eq. 5.26 and then the difference table for q_i can be formed from the recurrence relation

$$q_i = \frac{\mu'_i}{\mu'_{i-1}} \cdot \frac{a}{i + \alpha + 1} \cdot q_{i-1} \tag{5.33}$$

for $i = 2, 3, \ldots$, with $q_0 = 1$ and $q_1 = \mu'_1$.

Let $G_n^\alpha(x)$ denote an approximation to $f(x)$ obtained by using the above technique and including values of $\mu'_1, \mu'_2, \ldots, \mu'_n$. Obviously the first n moments of $G_n^\alpha(x)$ are $\mu'_1, \mu'_2, \ldots, \mu'_n$ and the integral condition $\int_0^\infty G_n^\alpha(x)dx = 1$ is also satisfied. Of course, there is no guarantee that $G_n^\alpha(X)$ does not have negative values at some points in the range $0 \leq x < \infty$, but in practice these have only occurred in the neighbourhood of the origin.

As can be expected, the inclusion of higher moments improves mainly the approximation to the tail of the distribution. Again, in practice, we have found it useful to include in the calculation as many moments as are available consistent with the production of a smooth difference table.

Note that the sum b_0 of the finite series $\sum_{k=0}^n c_k L_k^\alpha(x)$ is best evaluated from the recurrence relation

$$b_r = \frac{(2r + 1 + \alpha - x)}{r + 1} b_{r+1} - \frac{(r + 1 + \alpha)}{r + 2} b_{r+2} + c_r \tag{5.34}$$

for $r = k, k-1, \ldots, 1, 0$, with $b_{k+1} = b_{k+2} = 0$

If the parameter α in $L_n^\alpha(x)$ is chosen to be zero, then the generalized Laguerre polynomials become ordinary Laguerre polynomials. In this case c_2 is not identically zero, relations in Eq. 5.26 are replaced by $\alpha = 0$, $a = 1$, and the functions q_i have the simple form $\mu_i/i!$; otherwise, the analysis is unchanged.

5.4 Moments modeling

In this last section we explored different strategies to approximate the fluctuations in energy deposits of the showers, and we ended up with two major candidates: modified

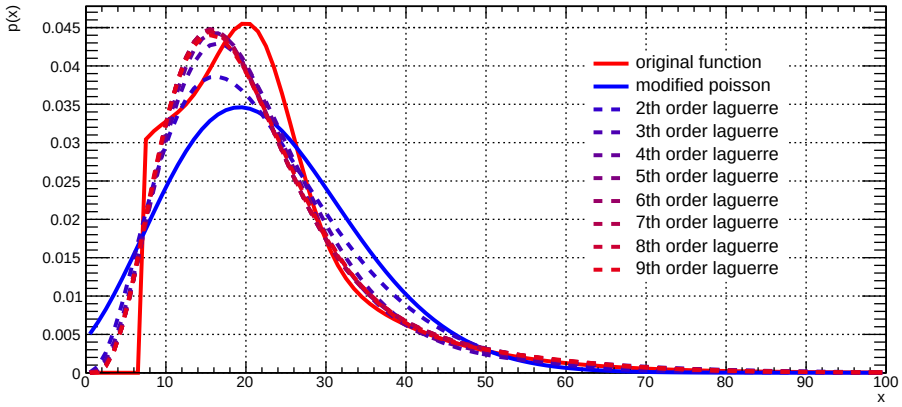

Figure 5.4: Examples of different approximations of a function using the Laguerre polynomials expansion.

Poisson function and sum of Laguerre polynomials. Both these methods, to recreate the PDF of the deposits, need the knowledge of some moments of the unknown fluctuation function.

For the modified Poisson we need the mean and the variance of the PDF. These metrics correspond respectively to the first raw moment and the second central moments of a distribution, but also the variance can be expressed in terms of only raw moments as

$$V(x) = \langle x^2 \rangle - \langle x \rangle^2 = \mu_2' - (\mu_1')^2 \tag{5.35}$$

The method based on the sum of generalized Laguerre polynomials, instead, should produce a closer approximation of the distribution the more are the moments that are known.

In order to implement both methods we modelled the raw moments of the energy deposits of electrons and of protons.

5.4.1 Mapping

A 3D histogram was used to map the average energy deposit density of the showers. The axes of the histogram are the logarithm of the total energy of the event, the longitudinal coordinate t and the radial coordinate r. The longitudinal coordinate was based on the MC direction of motion of the primary particle in order to avoid bias in the modelization related to the reconstruction method of the longitudinal direction. Every bin is filled with the average radial deposited energy in a cube placed within that (t,r) bin. The radial deposited energy is defined as in Eq. 5.11 as

$$f_i = \frac{\varepsilon_i r_i X_0 R_M^2}{V_{cube}} 2\pi \tag{5.36}$$

Where V_{cube} is the volume taken by a calorimeter cube, external mechanics included, and ε_i is the measured energy in the i^{th} cube. Both a mapping of the MC deposited energy and a reconstructed energy measurement, with noise and digitization simulation were created.

Each of these histograms were also built for several powers of the radial deposited energy density in order to map the raw moments of the deposited energy intrinsic PDF. In particular, we have a map up to the 16^{th} power.

Fig. 5.5, 5.6 show the histograms obtained for the development of showers generated respectively by electrons and protons, together with some slices corresponding to examples *totDep* bins. Fig. 5.7 and 5.8 show the same, but the energy deposits are digitized.

This mapping of the 16 moments have been performed on both electron and proton data and is already sufficient to evaluate a binned approximation of the energy deposition fluctuations of both electrons and protons in the 100GeV-10TeV energy range.

We have also explored the possibility to fit this development to get a parametrized description that could be more powerful and maybe even extendable at higher energies.

5.4.2 Fitting

The spatial development of the deposited energy density $f(t, r, E_0)$ at a fixed energy bin *totDep* can be factorized as

$$f(t, r, E_0) = f_L(t, totDep) \cdot f_T(r, t, totDep) \tag{5.37}$$

Both the longitudinal component $f_L(t)$ and the transversal component $f_T(r, t)$ can be fitted from the mapping of the development that we built.

Longitudinal development

The longitudinal component for an electromagnetic event, electron-like, is described by the function in Eq. 3.9.

$$f_L(t) = b\,\frac{(bt)^{a-1}e^{-bt}}{\Gamma(a)} \tag{5.38}$$

This parametrization depends only on the 2 parameters a and T_0, since $b = (a-1)/T_0$. Fig. 5.9 shows a selection of fitted longitudinal profiles for different total energy, while Fig. 5.10 show the value of the parameters from the fits with respect to the logarithm of the total energy of the event. Both the parameters are fitted by a linear model.

Transversal development

The transversal development for electromagnetic showers has been described using simulations in [123] as the sum of core and a tail contribution as

$$f_T(r, t) \propto Q_C \frac{2rR_C^2}{\left(r^2 + R_C^2\right)^2} + (1 - Q_C)\,\frac{2rR_T^2}{\left(r^2 + R_T^2\right)^2} \tag{5.39}$$

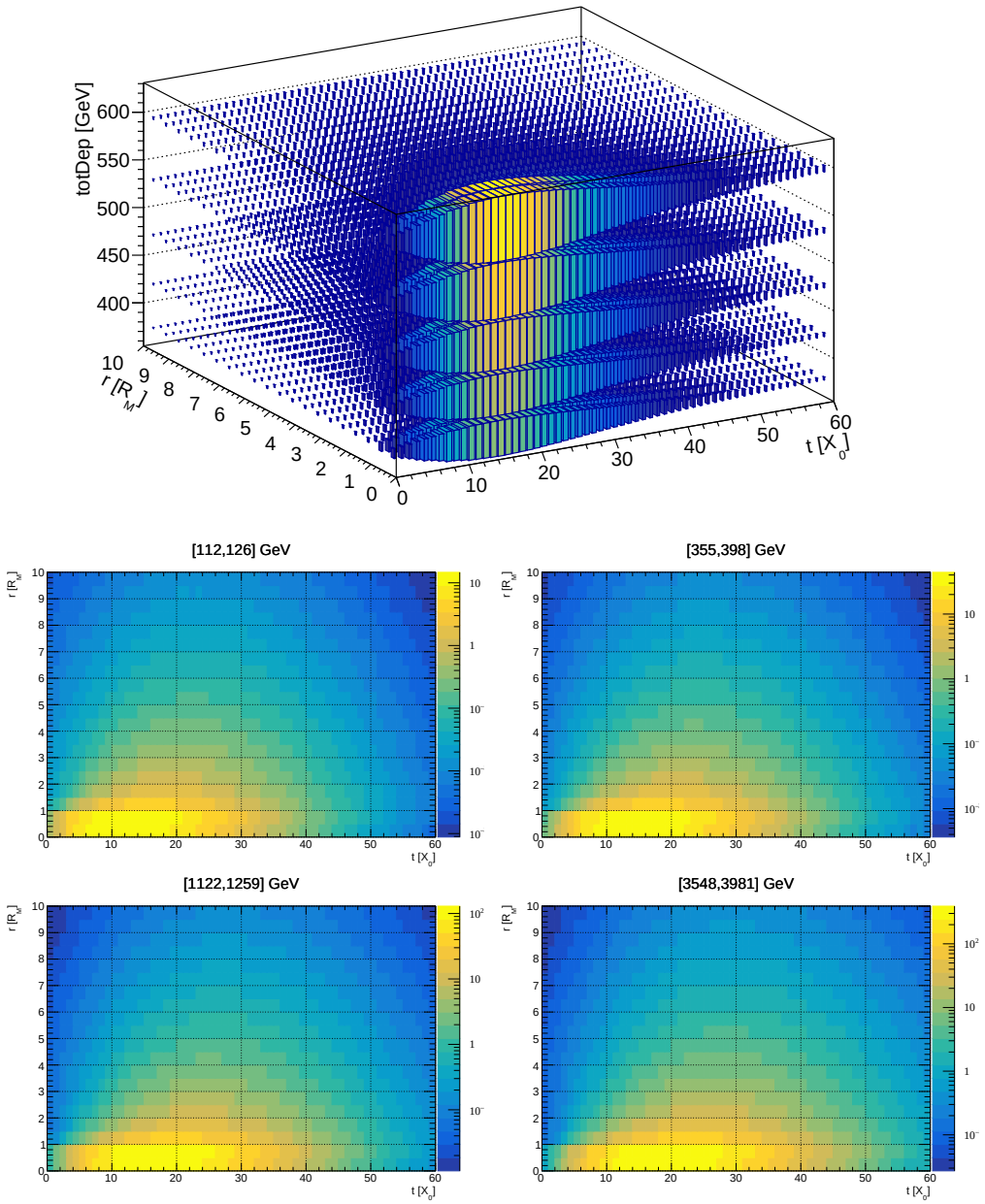

Figure 5.5: On top, average radial development of the deposited energy density for electrons at different reconstructed energy. At the bottom examples from 4 energy bins of the longitudinal and radial development.

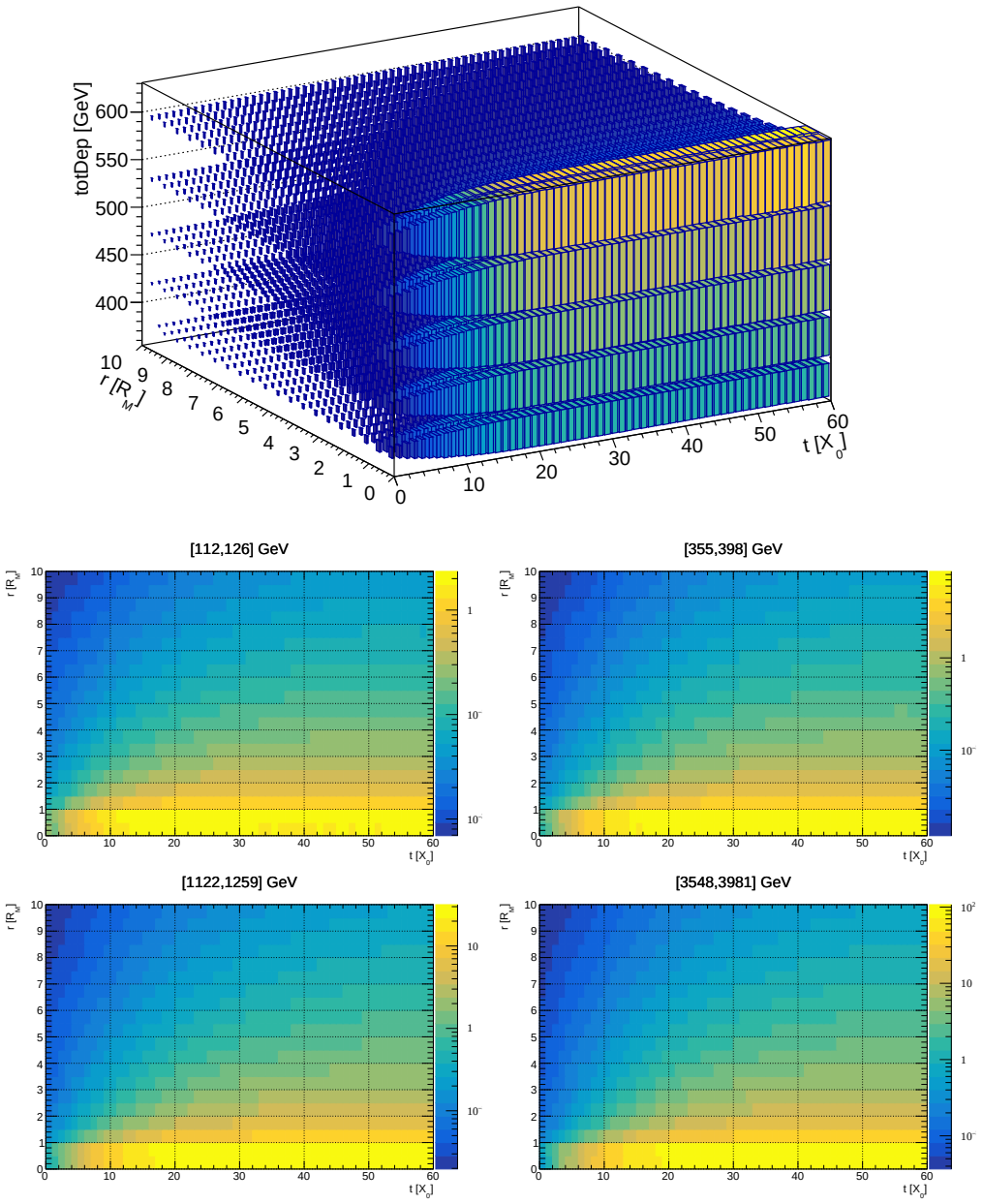

Figure 5.6: On top, average radial development of the deposited energy density for protons at different reconstructed energy. At the bottom examples from 4 energy bins of the longitudinal and radial development.

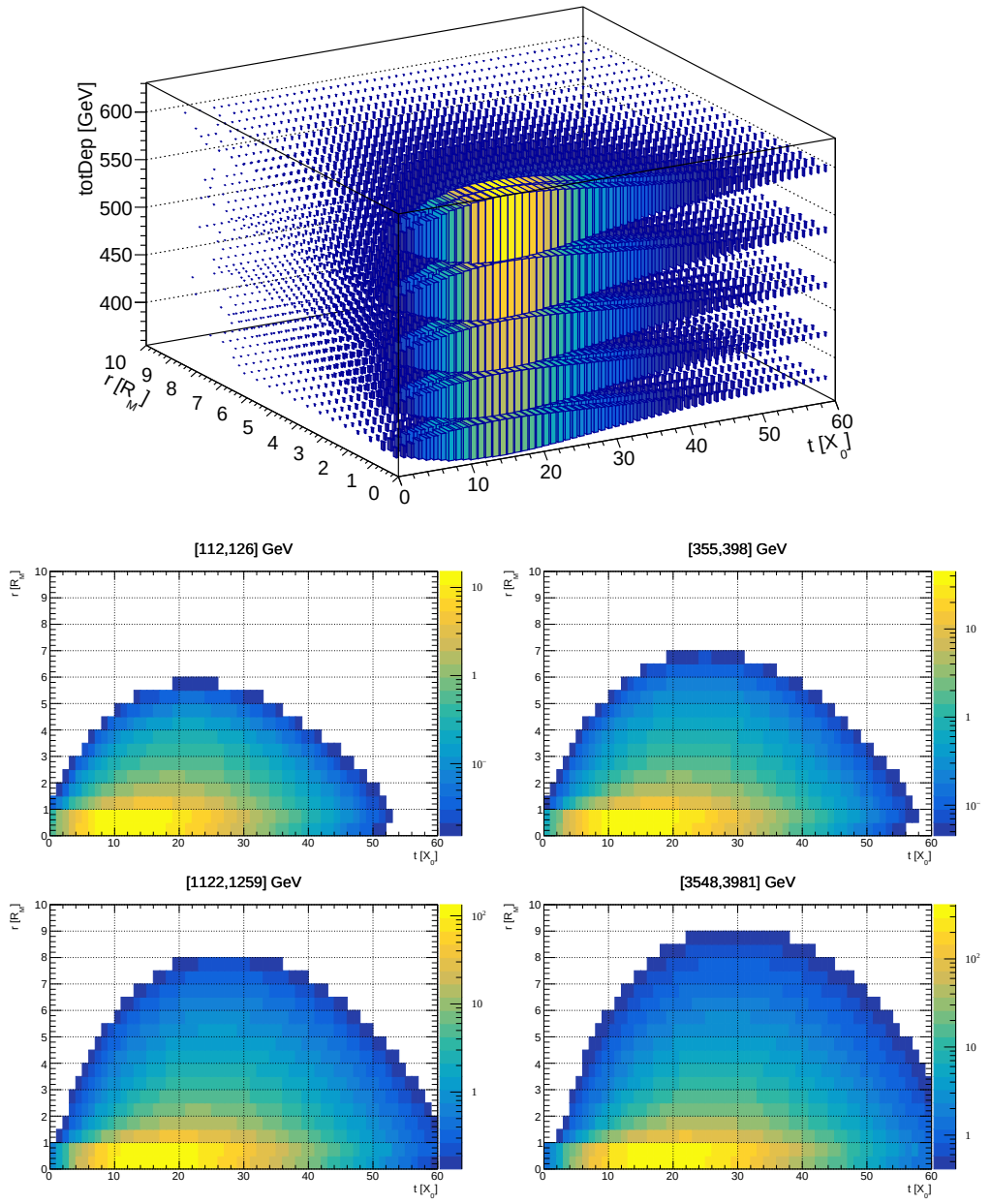

Figure 5.7: On top, average radial development of the deposited energy density for electrons at different reconstructed energy. At the bottom examples from 4 energy bins of the longitudinal and radial development.

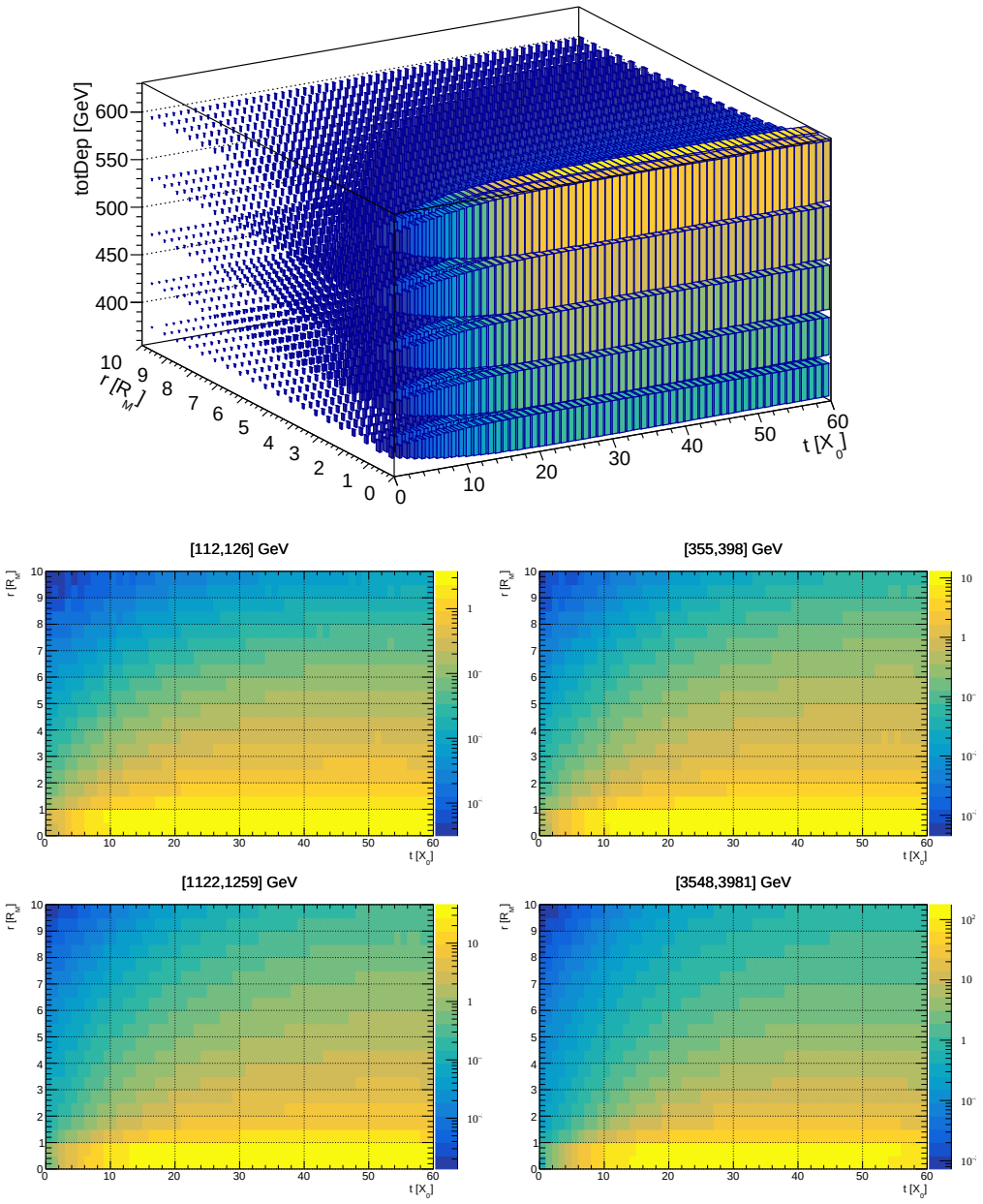

Figure 5.8: On top, average radial development of the deposited energy density for electrons at different reconstructed energy. At the bottom examples from 4 energy bins of the longitudinal and radial development.

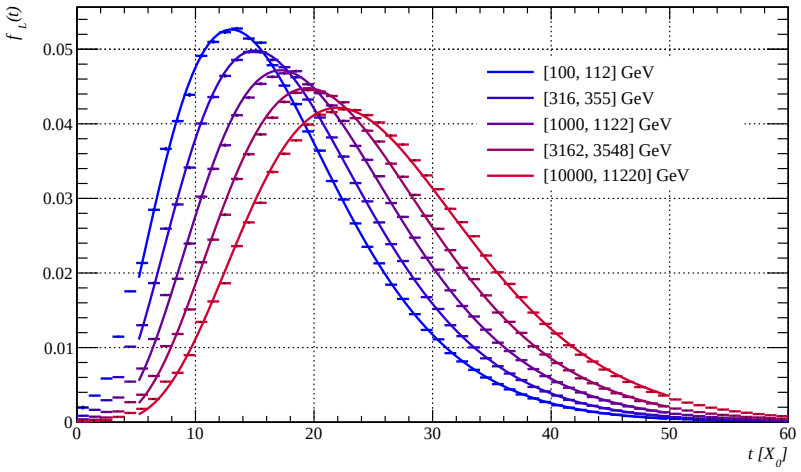

Figure 5.9: Longitudinal fits on some examples of shower development for different $totDep$.

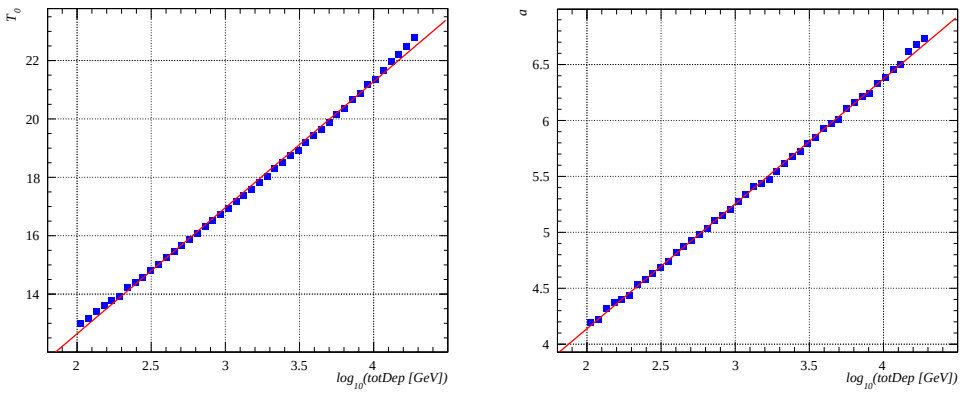

Figure 5.10: Linear fit on the longitudinal parameters T_0 and a with respect to $log_{10}(totDep)$.

For our case we can't use this expression out of the box because the profiles that we reconstruct are actually convoluted with the spatial resolution that we have on the radial direction. This resolution is about the size of a cube near the core, but gets finer as the r coordinate increases because of the combined contribution of a ring of cubes corresponding to the same (t, r) region.The result is a profile that appears broader at the core, while it gets more similar to Eq. 5.39 towards the tail.

To fit these profiles we tested several models looking for a function that could describe them well enough, that depends on a limited number of parameters, and that could be analytically normalized. The function that we found and used is

$$f_T(r,t) = r\left(2w\frac{e^{-r^2/h}}{h} + (1-w)\frac{(c-1)(c-2)}{R^2}\left(\frac{R}{r+R}\right)^c\right) \tag{5.40}$$

This function depend on 4 parameters: w that is the relative weight of the core component with respect to the tail, h which encodes the width of the core, R and c that characterize the shape of the tail. All four of these depend on both total energy of the event and t in a non-trivial way.

An important detail indeed is that transversal profile need to be modelled with respect to the t coordinate, for this reason we performed independent fits on slices of the development with a width of 3 X_0 along the longitudinal development. The width of 3 X_0 is chosen to avoid longitudinal bins where no crystals are included. Examples of these profile can be seen in figure 5.11 that depicts the comparison of radial profiles at 6 different depth of the shower for different values of $totDep$.

Fig. 5.12 shows the values obtained from the fits for the 4 parameters. To map and eventually predict the evolution of the parameters we used 2D bicubic splines implemented in the library ALGLIB[124] and fitted on the fitted values of the parameters. Fig. 5.13 show the 2D splines found from these fits.

5.4.3 Square energy deposit

So we have now a quite complete description of the average local energy deposit of EM showers. In order to describe the way these deposits fluctuate we also need to model at least their variance. To simplify the modelization, instead of the variance we'll study the square deposited energy density. Together with the model of the mean this function will provide us a description of the variance as $V[x] = E[x^2] - E[x]^2$. The advantage of this approach is that the same functions that we used for longitudinal and radial profiles of the average fit well on the mapped development of the squared deposits. Fig. 5.14 and 5.15 shows the fitting results.

5.5 Modeling realistic energy deposit

When using the realistic energy deposit to build a model of the shower energy fluctuation, we have to take into account that there is a threshold for the measured signal because, to save on bandwith, only signals over such threshold are sent to ground.

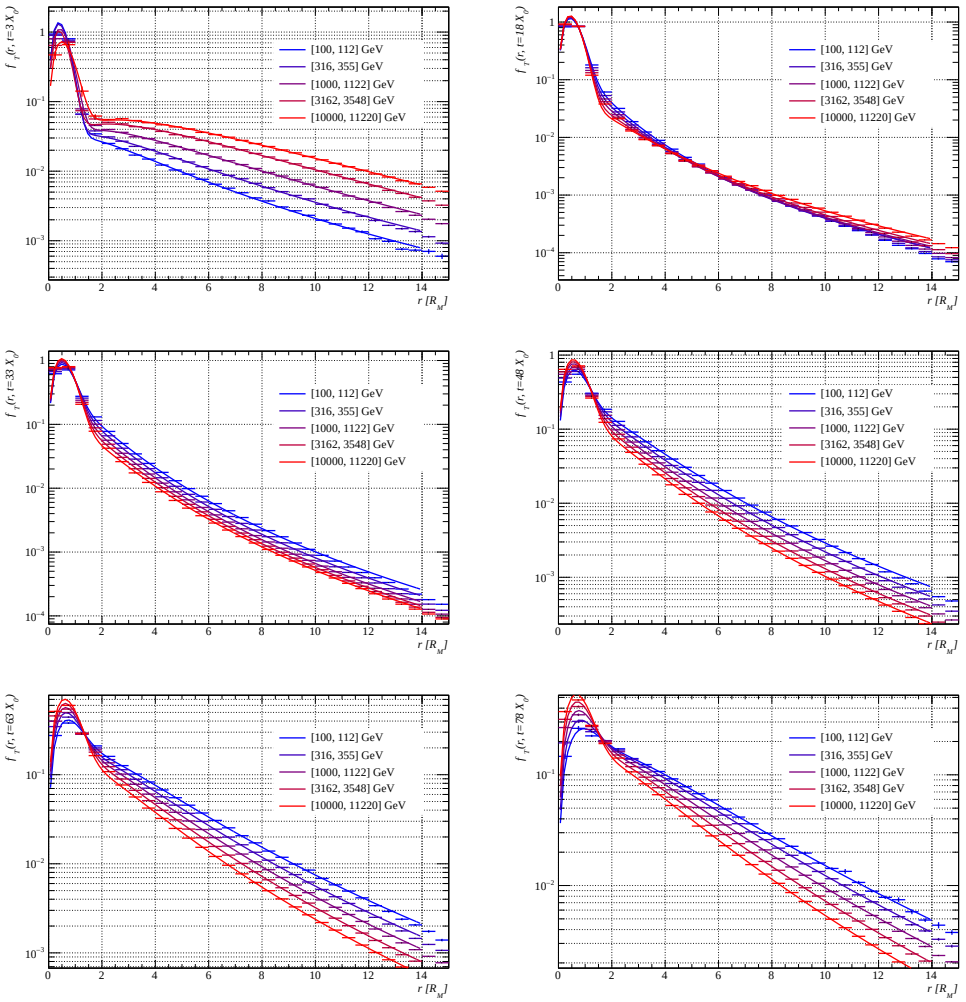

Figure 5.11: Transversal profiles of the average electromagnetic shower at different depths and different energy fitted using Eq. 5.40.

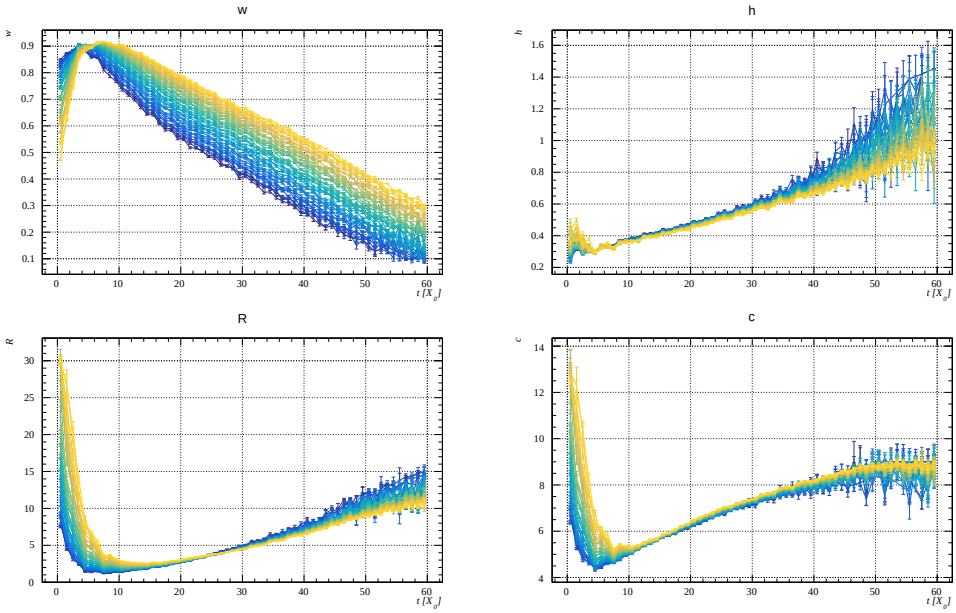

Figure 5.12: Values of the parameter w, h, R and c obtained by fitting the transversal model on the average electromagnetic shower. On the horizontal axis is reported the depth t, while the color scale represent the $totDep$ value, from 100 GeV (blue) to 10 TeV (yellow).

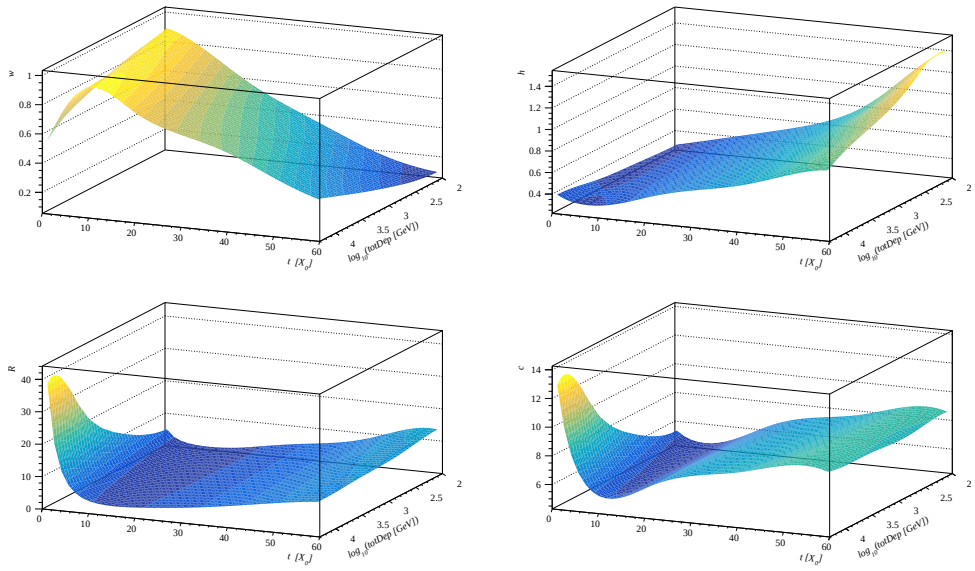

Figure 5.13: 2D bicubic splines that fit the fitted values of the 4 parameters used for the transversal model of the average electromagnetic shower (Fig. 5.12).

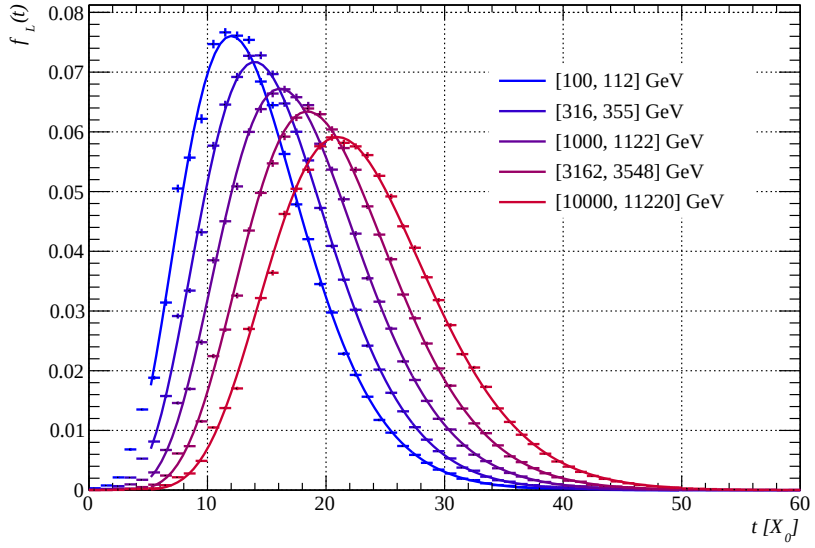

Figure 5.14: Fits on some examples of longitudinal development of squared energy deposit for different *totDep*.

The existence of this threshold open some issues related to the construction of a proper PDF because, if we ignore zero values we could lose useful information from shower data, while if we include them in the moments models we get to describe a non-continuous PDF with a hole between 0 and the threshold value.

What we decided to do is to map the average and the moments only on the above-threshold values, but to also record how many times every $(t, r, totDep)$ bin doens't reach the threshold. This way we can have a PDF that is defined as a step function like:

$$p(\varepsilon) = \begin{cases} \dfrac{N_{\text{blw}}}{\varepsilon_{\text{thr}} \cdot N}, & \varepsilon < \varepsilon_{\text{thr}} \\ \dfrac{1 - N_{\text{blw}}}{N} \cdot p_{\text{abv}}(\varepsilon), & \varepsilon \geq \varepsilon_{\text{thr}} \end{cases} \tag{5.41}$$

Where N is the total number of measurement that we collect in a $(t, r, totDep)$ bin (both below and above the threshold), N_{blw} is the number of measurement below the threshold in the same bin, ε_{thr} is the threshold value and $p_{\text{abv}}(\varepsilon)$ is the PDF built using the moments above the threshold.

Using this PDF we can include every crystal of the calorimeter in the evaluation of the discrimination parameter and compare the recorded deposit with a complete description of the expected behavior of such crystal. If the crystal record a below-threshold signal we compare this with the probability of having a below-threshold signal, if it records an above-threshold signal we compare it with the probability of seeing that particular signal value.

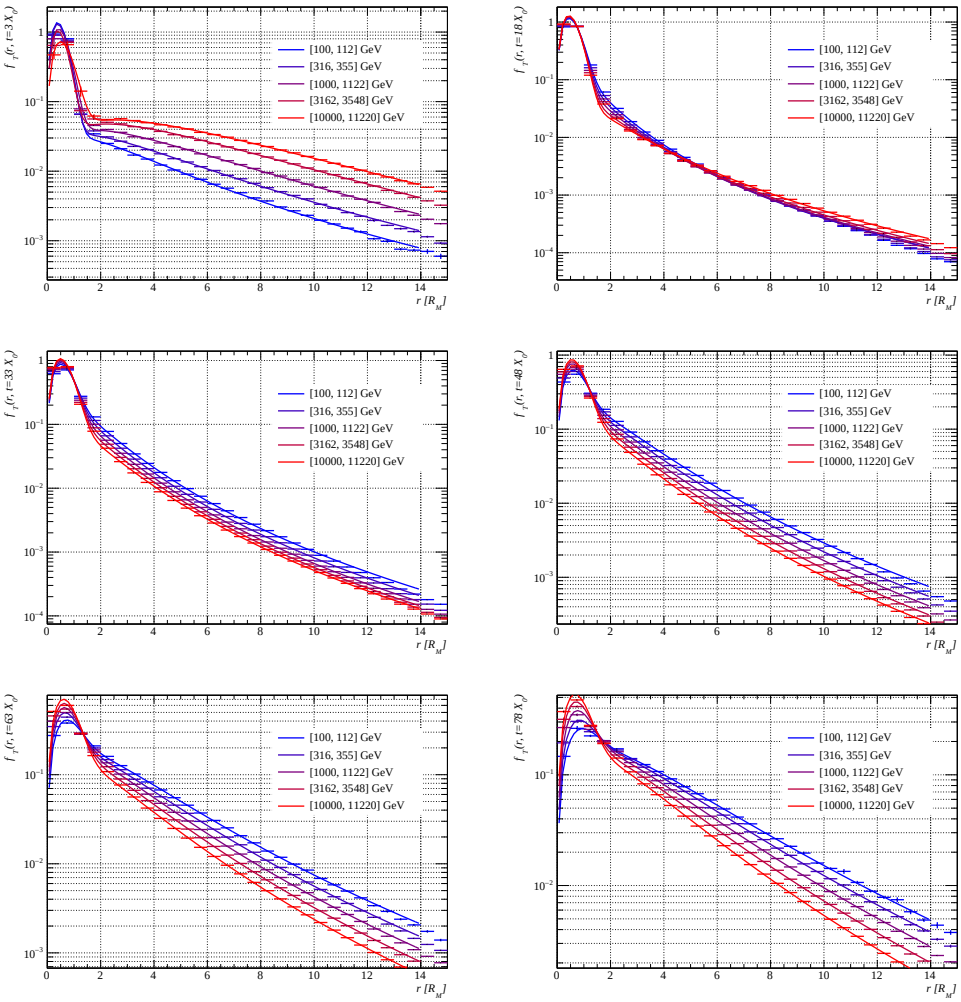

Figure 5.15: Transversal profiles of the average square energy deposit of electromagnetic events at different depths and different energy fitted using Eq. 5.40.

5.6 Hadronic shower modeling

When we proceed to model the hadronic shower statistical behaviour we face much bigger difficulties compared to electromagnetic events because of the different kind of interactions generated during the shower development.

To start, since the hadronic interaction length is larger than the EM radiation length, the showers extend on longer distances and therefore the showers itself are generally much less contained in the calorimeter volume.

Moreover, there's a much greater fluctuation in the depth of the first interaction, meaning that it's common to see the primary proton traverse many cubes, interacting only through ionization, before it start producing secondary particles.

At last, π^0 produced in the shower decay in γ-photons that start EM showers within the hadronic shower adding further irregularities to the statistical behavior of the showers. Fig. 5.16 shows a comparison of the longitudinal development of 100 electron showers and 100 proton showers produced between 100 GeV and 1 TeV in order to highlight the difference in regularity of the development.

Because of the aforementioned differences in the development of the hadronic showers, producing an analytical model of the shower development using the same approach as that for EM showers requires additional investigations that are beyond the scope of this work, so we didn't produce an analytical model of the development, but only relied on the binned mapping of the average energy deposit density and the other raw moments.

5.6.1 Shower regularization

In order to obtain a more refined description of the hadronic shower behaviour we explored some regularization adjustments on the showers through renormalization of specific shower observables. The idea is based on theoretical studies[98, 125] predicting that for both electromagnetic and hadronic showers it exist a universality in the development of the profiles. This universality is valid, in particular when the showers are described in terms of the so-called *age*, a longitudinal parameter that accounts for the rate of growth of the shower itself and can be approximated as

$$s \simeq \frac{3t}{t + 2t_{max}}. \tag{5.42}$$

To approach this regualrization we also need to take into account the different starting points of each shower first and then scale the longitudinal development according to the new longidutinal coordinate. This produce much more regular showers that always start at $s = 0$, peak at $s = 1$ and end around $s = 3$.

As we found out this is actually detrimental for particle ID because we are removing from the models most of the information that distinguish the two particle species. For this reason we kept the models for both EM and hadronic showers in the (t, r) reference frame without further regularizations.

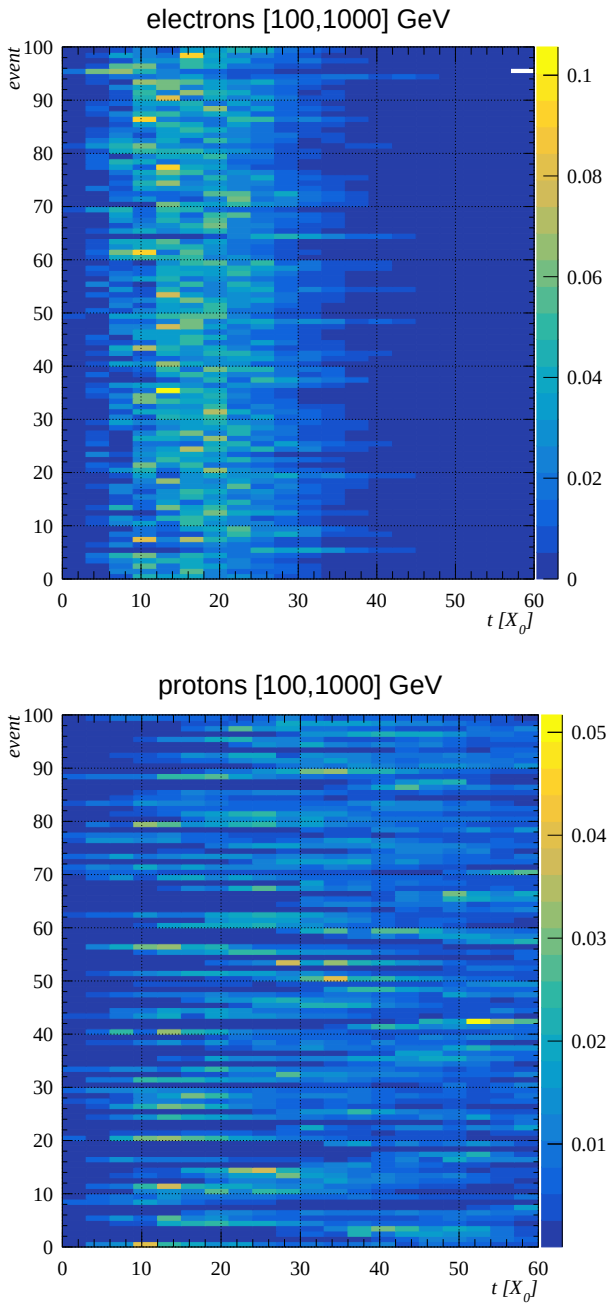

Figure 5.16: Comparison of the longitudinal development of 100 electron showers (top picture) and 100 proton showers (bottom) produced between 100 GeV and 1 TeV. The color scale represents the deposited energy at the corresponding longitudinal coordinate t. While the showers generated by electrons produce very regular and similar showers, those produced by protons appear much more irregular.

5.7 Likelihood evaluation

To apply the likelihood test that we described is Sec. 5.1.1 we take the values of reconstructed energy deposit in every cube of the calorimeter, we convert the value in a radial deposited energy density as per Eq. 5.11, and we evaluate the Likelihood as the product, over all cubes, of the approximated PDF evaluated on the measured values as per Eq. 5.2.

The longitudinal and radial coordinates are determined through a Principal Component Analysis on the 3D shower: the longitudinal direction is identified as the main component, i.e. the direction on which the shower deposits show the largest spatial variance.

In order to avoid computational problem due to the large numbers involved (i.e. Γ-function), instead of the actual probability $p(\varepsilon)$ we computed the logarithm of the probabilities and summed the $log_{10}(p(\varepsilon))$ values. This way we obtain immediately the so-called log-Likelihood $logL$. Instead of dealing with the $logL$, it is actually common to deal with its opposite value $-logL$. This way for the very low value of probability usually involved when combining many measurements, $-logL$ is a positive number and the maximum probability is associated with the lowest value.

Once evaluated the metrics, in order not to have distributions biased by the discontinuity in the simulated spectrum, we need to properly weight the contributions from different segments of the spectrum.

The $-logL$ are evaluated for the electron hypothesis and for the proton hypothesis. As described in section 5.1.1 we can also combine these two metrics in a likelihood ratio $\Lambda = L^e/L^p$ or, more conveniently its logarithm

$$\lambda = log(\Lambda) = log(L^e) - log(L^p). \tag{5.43}$$

Dividing this value for the number of cubes with energy deposit above threshold has proved to regularize the performance with respect to reconstructed energy, and in some cases improve the separation of the two species, as we'll see in the next chapter.

5.8 Mean square deviation

Another, easier, way of evaluating the accordance of observed events with the statistical behavior of electrons or protons is measuring the mean square deviation of each energy deposit from the expected one.

For every event we evaluated the value

$$s^\alpha = \frac{1}{N}\sum_{i=1}^{N}\frac{(\varepsilon_i - \mu(\alpha)_i)^2}{\sigma_i^2(\alpha)}, \tag{5.44}$$

where ε_i is the deposited radial energy density measured in the bin i, α represent either electron or proton hypothesis to be tested, $\mu(\alpha)_i$ is the expected energy density measured

in the bin i for a particle of species α, and $\sigma_i^2(\alpha)$ is the estimated variance for such particle in the bin.

Also in this case the figure relative to electron hypothesis and that relative to proton hypothesis can be combined in a synthetic one that evaluates the relative score of the event as a simple ratio or as normalized ratio.

We define these quantities as

$$X = \frac{s^e}{s^p} \tag{5.45}$$

and

$$\chi = \frac{s^e}{s^e + s^p}, \tag{5.46}$$

5.9 Convolutional Neural Network

Beside these approaches that focus on a controlled modelling of the statistical behaviour, it's now more and more common to rely on machine learning solution for the discrimination of events. In particular the problem of shower based discrimination is commonly dealt with Convolutional Neural Networks (CNN)[126, 127].

These tools are particularly powerful in modelling patterns in multidimensional matrix of data. They are widely used for image recognition and are easily employable in the analysis of the particle showers. Thanks to the collaboration with colleagues from Università di Roma Tor Vergata, we developed a convolutional neural network that can work on 2D pictures of the events showers. These pictures used by the CNN are projection of the shower development in the same longitudinal-radial reference frame that we used for our analysis. Fig. 5.17 some examples of events, two electrons on top and two protons on bottom, as they are used by the CNN. The radial binning is coarser to avoid a higher occurence of void bins due to the crystals spatial distribution. This is important because even for the training the CNN process one event at a time, while we built the modelization from a statistical bulk.

The network was trained on the same datasets of events that we used for the modeling, with the same selections through a supervised process that associate to each picture two parameters: an *electroness* λ_e and a *protoness* λ_p. For electron showers $\lambda_e = 1$, while $\lambda_p = 0$ and vice versa.

When tested on new events the CNN will produce a value of λ_e and one of λ_p. The fraction $\lambda_e/(\lambda_e + \lambda_p)$ can then be used a discrimination parameter.

5.10 Conclusion

In this chapter we selected and assembled three families of discriminators that should be able to evaluate how close an event is to the expected EM shower or hadronic shower. In the next chapter we'll describe and gauge the performance that we get when testing these tools on new events.

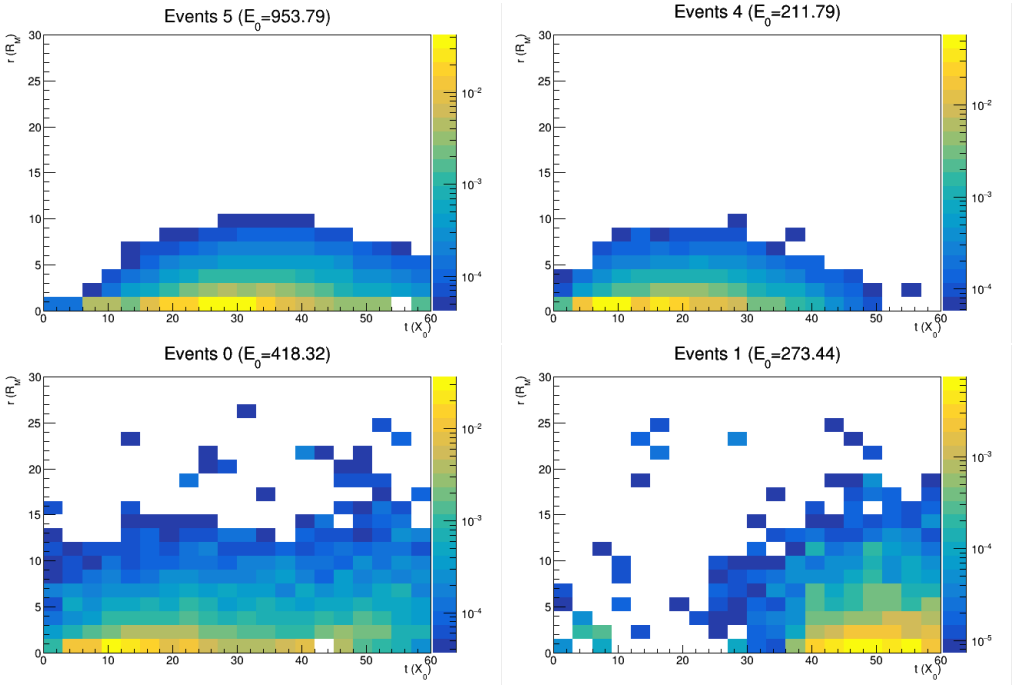

Figure 5.17: Examples of pictures of the showers used for the training of the CNN. On top two electron-generated showers, on the bottom two proton-initiated showers. The color scale represents the average radial deposited energy in a $t-r$ bin for the considered shower.

Chapter 6

Particle identification performances

In chapter 5 we described several metrics that can be used as discriminators to identify the nature of an observed cascade shower on the base of their compatibility with a statistical model of the typical EM or hadronic shower. By applying a simple cut on a certain value of these metrics, we can tag events as the signal of our analysis or discard them as background events. With an ideal discriminator we would have perfectly separated distributions of EM and hadronic events that would allow us to tag any single event as signal or background. In any realistic application, however, these distributions overlap with each other and therefore there's always a tail of events that were misidentified. This means that any cut that we perform on the event will produce a population of protons that end up tagged as electrons (background contamination) and a population of electrons that will end up tagged as protons (signal inefficiency). For every metrics we will need to find an optimal balance between two performance figures that are the signal selection efficiency:

$$\varepsilon_{sig} = \frac{\text{selected signal events}}{\text{total signal events}} \tag{6.1}$$

and the background rejection efficiency

$$1 - \varepsilon_{bkg} = 1 - \frac{\text{selected background events}}{\text{total background events}} \tag{6.2}$$

Fig. 6.1 shows a graphical example of how this works with two distributions of the discriminator λ for signal and a background that overlap. The selection includes some true positives (TP) corresponding to signal events together with some false positives (FP) that represent the background contamination in the measure.

For a given discriminator, choosing different cut values produce different values of ε_{sig} and $1 - \varepsilon_{bkg}$. For a typical discriminator these two figures are generally anti-correlated, i.e. one gets smaller while the other grows and vice-versa, but in order to get the best rejection performances we need to maximize them both.

This kind of relation are commonly represented by mean of a type of graph called ROC (Receiver Operating Characteristic) curve. These curves describe on a Cartesian plot signal efficiency and background rejection for different choices of selection on the

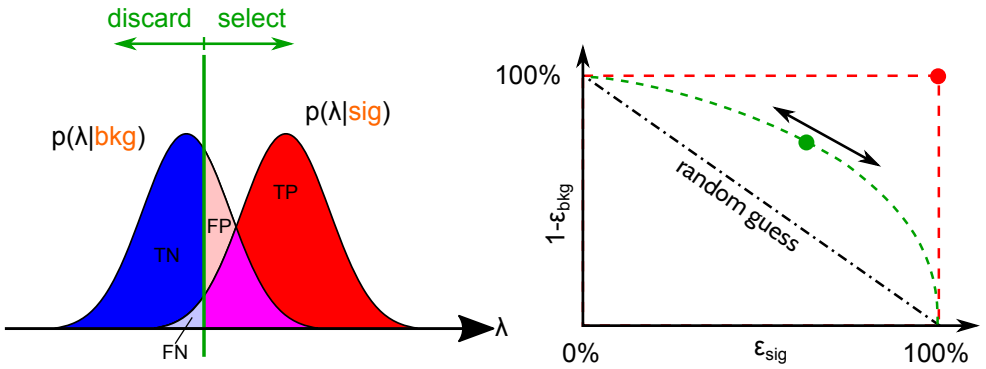

Figure 6.1: On the left an example of cut based selection with signal and background distribution that overlap. On the right ROC curves for a generic discriminator (green), an ideal one (red) or a null one (black). The picture is adapted from [128].

discrimination parameter. Going through any possible cut value we obtain curves like those depicted on the right of Fig. 6.1. In the case of perfect discriminator with no overlap between signal and background, the ROC describe a right angle (see the red line in Fig. 6.1). In this case the optimal choice for the cut is any value that determines the vertex of the curve corresponding to $\varepsilon_{sig} = 1$ and $1 - \varepsilon_{bkg} = 1$. On the other hand if the two distribution are perfectly overlapped, the discriminator does not provide any information and the selection is analogous to a random guess (black line in the picture). In most practical applications the curve is somewhere between these two cases (green line).

Since in CRs we have an extremely high rate of protons with respect to electrons ($p/e \simeq \mathcal{O}(10^3)$) we need to be very efficient in the rejection of background. In particular in chapter 4 we discussed the relative uncertainty on the measure of the flux of $e^- + e^+$ and observed that, in order to contain the uncertainty deriving from the residual background contamination ε_{bkg} to a negligible level in the 100 GeV-10 TeV range, we need to reduce it to less than 10^{-3}. For convinience we will quantify this quantity in terms of the background suppression $1/\varepsilon_{bkg}$.

The next sections of this chapter will describe the distributions of the discriminators described in the last chapter when evaluated on the datasets of electrons and protons that we simulated. These distributions are used to evaluate the discrimination performance of each parameter in the reconstructed energy range from 100 GeV to 10 TeV.

To make graphs easier to read we'll use the nomenclature described in table 6.1 for the studied discriminators. The details relative to the different properties will be exlpained in the following sections.

Discriminator	Type	PDF approximation	Modeling	Hypothesis
$nLogL$	Likelihood	Modified Poisson	Fit	Electromagnetic
$nLogL^{EM}_{pois}$	Likelihood	Modified Poisson	Map	Electromagnetic
$nLogL^{H}_{pois}$	Likelihood	Modified Poisson	Map	Hadronic
Λ_{pois}	Likelihood	Modified Poisson	Map	Ratio
Λ_{pois}/N	Likelihood	Modified Poisson	Map	Normalized ratio
$nLogL^{EM}_{lag}$	Likelihood	Laguerre pol. sum	Map	Electromagnetic
$nLogL^{H}_{lag}$	Likelihood	Laguerre pol. sum	Map	Hadronic
Λ_{lag}	Likelihood	Laguerre pol. sum	Map	Ratio
Λ_{lag}/N	Likelihood	Laguerre pol. sum	Map	Normalized ratio
s^{EM}	Mean square dev.	None	Map	Electromagnetic
s^{H}	Mean square dev.	None	Map	Hadronic
χ	Mean square dev.	None	Map	Ratio

Table 6.1

6.1 Fitted EM model

Using the parametrization of the average electromagnetic shower deposits and of their variance described in chapter 5, we can build a PDF for the radial deposited energy based on the modified Poisson function. This PDF can be used to evaluate a likelihood associated to the hypothesis of electromagnetic shower for each tested event.

Figure 6.2 shows the distribution of the negative log-likelihood ($nLogL$) obtained when testing electrons (in red) and protons (in blue) with respect to the total deposited energy ($totDep$) of the events in the range 100 GeV to 10 TeV. The two populations of particles clearly gather around separated values of the discriminator, however some overlapping still exists. The middle picture in Fig. 6.2 show more clearly how the distributions intersect for the specific bin $[1, 1.12]$ TeV. It's apparent that it doesn't exist a cut that can completely remove all background without strongly compromise signal efficiency. The bottom picture of Fig. 6.2 show the ROC curves that we obtain using $nLogL$ to discriminate electrons from protons at different $totDep$. For a 90% signal efficiency the background suppression is about 10^3 for all the shown energies, while it rises between 2×10^3 and 5×10^3 for an 80% signal efficiency.

It's interesting to examinate how this parameter changes for different arrival directions of the primary particle. We expect the 3D segmentation of the CALO to provide isotropic performances in the reconstruction and analysis of the events, we can then try to observe how $nLogL$ changes selecting event with respect to the polar or azimuthl angle of arrival. Fig. 6.3 shows the distribution of the discriminator values at different angles. Except for some slight variations corresponding to the directions perpendicular to a face of the CALO, the distributions appear to be highly independent of the direction of arrival.

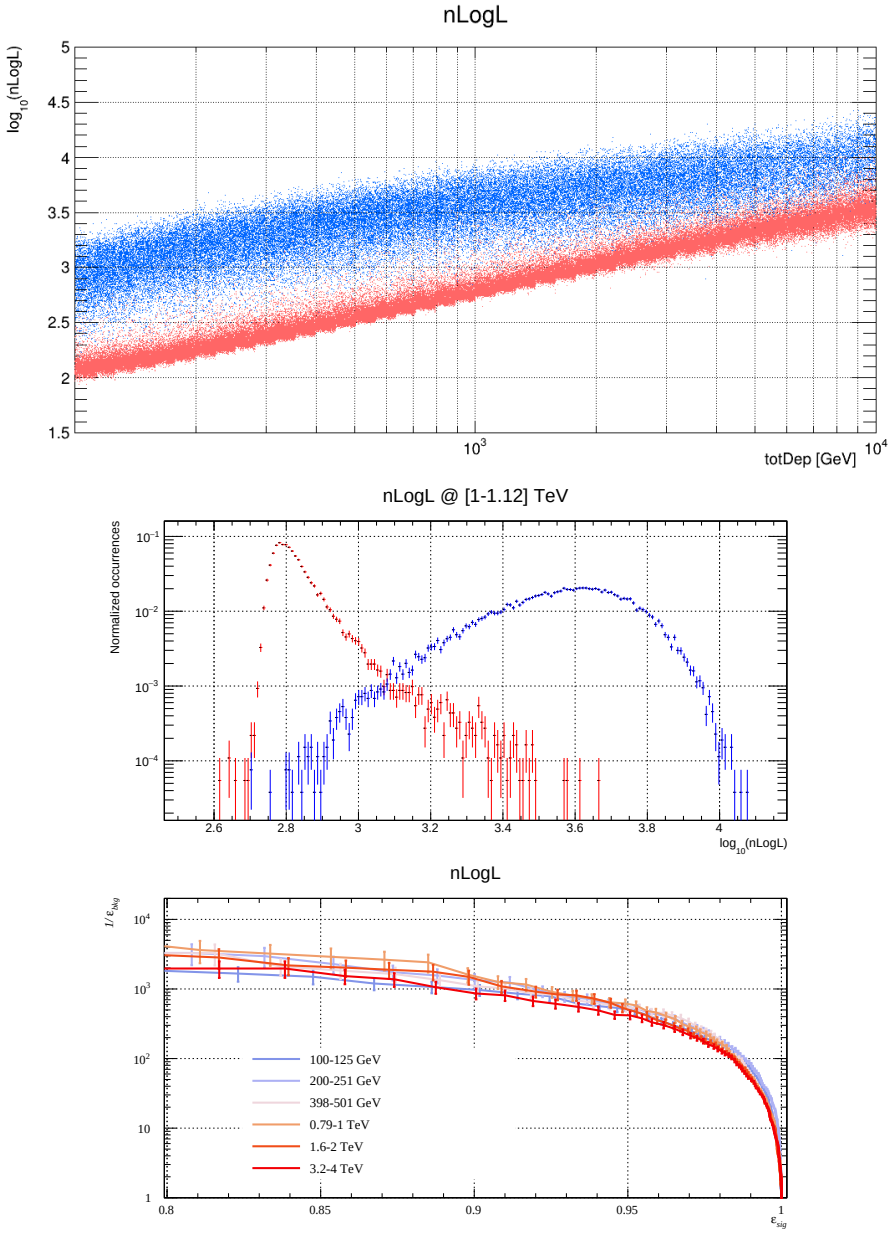

Figure 6.2: On top the distribution of the discrimination parameter *nLogL* for electrons (red) and protons (blue) with respect to the total deposited energy. At the bottom the detail of the same distribution for a specific *totDep* bin (middle) and the ROC curves obtained at some *totDep* bins (bottom).

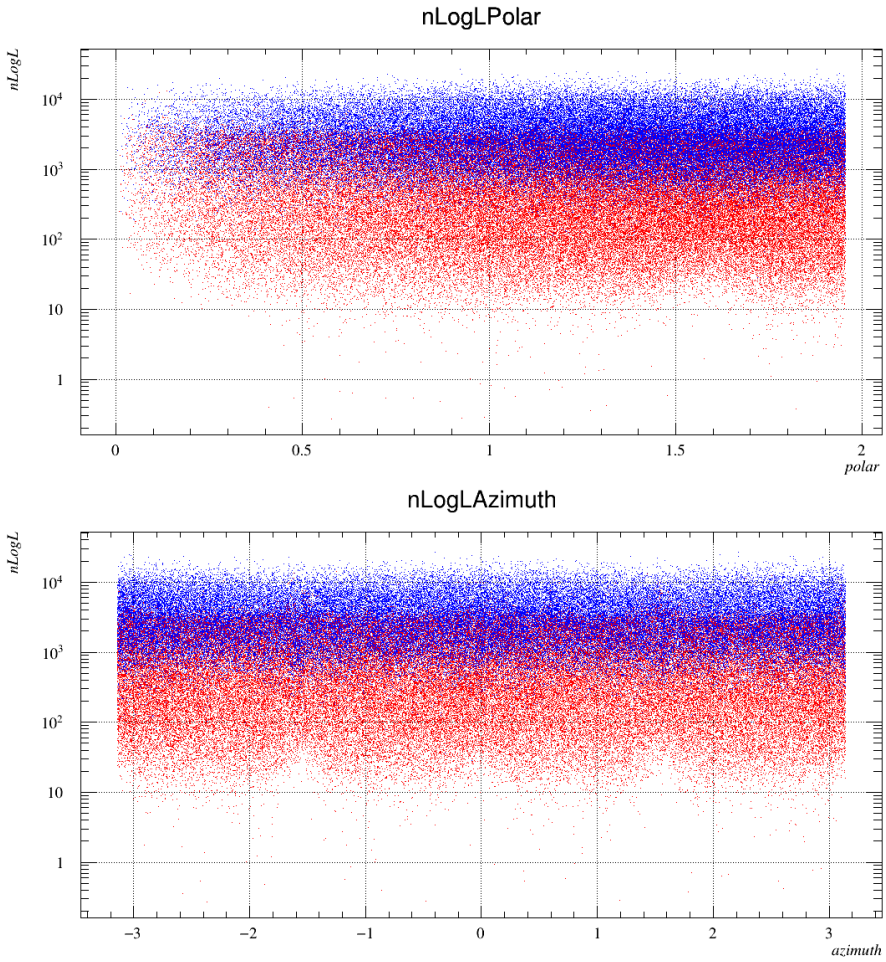

Figure 6.3: Distributions of nLogL for electrons (red) and (protons) with respect to polar angle (top) and azimuth (bottom).

6.2 Mapping of the development

Without relying on the complex parametrization of the development and its fluctuations, we can build a PDF for the radial energy deposits using directly the map that we outlined of the average and higher moments of these deposits. This approach loses any predictivity out of the tested ranges of t, r and $totDep$, but might reduce some systematic uncertainty introduced by the complexity of the model and can be easily extended to the testing of hadronic hypothesis.

6.2.1 Modified Poisson approximation

The average and variance of the energy deposits were combined into a PDF based on the modified Poisson function (Eq. 5.18) and this was used to evaluate the EM and Hadronic likelihood of the electrons and protons of our dataset. Fig. 6.4 show the distributions that we obtain for the EM likelihood and that obtained for the hadronic one.

The hadronic likelihood doesn't seem to provide any useful separation per se, but can be used to evaluate a likelihood ratio that, according to Neyman-Pearson lemma should produce the most powerful discrimination between the two hypotheses [112]. Fig. 6.5 shows the distributions that we obtain for the ratio of likelihoods that, in terms of log-likelihood becomes the difference

$$\Lambda_{pois} = nLogL^{EM}_{pois} - nLogL^{H}_{pois}. \tag{6.3}$$

In Fig. 6.5 is also reported an example of the distributions of electrons and protons values of Λ_{pois} for the specific $totDep$ bin $[1, 1.12]$ TeV and the ROC curves for this discriminator applied in different bins of reconstructed energy.

The distributions populate two well-defined regions divided by the $\Lambda_{pois} = 0$ value. The higher the total energy of the event the larger the absolute value of the discriminator is. This is because the more energetic showers extend on a larger portion of the CALO and therefore have more terms in the calculation of the likelihood. Normalizing Λ_{pois} could regularize the distribution of the resulting likelihood. Fig. 6.6 shows the distributions for Λ_{pois} divided by the number of above the threshold deposits in the calorimeter for each event.

The background suppression that we obtain from Λ_{pois} and Λ_{pois}/N are very similar, but the normalized ratio appear to perform a bit better. For 90% signal efficiency Λ_{pois} have a background suppression just below 10^3, while that produced by Λ_{pois}/N is just above. For both metrics, $1/\varepsilon_{bkg}$ slowly grows as ε_{sig} approaches 80%.

6.2.2 Sum of Laguerre polynomials approximation

As we saw in the previous chapter, the PDF of the energy deposits can also be approximated as a sum of generalized Laguerre polynomials. Also in this case we can evaluate both an EM hypothesis and a hadronic one. Figure 6.7 shows the distributions that we obtain evaluating the negative log-likelihood assciated with the two hypotheses. The

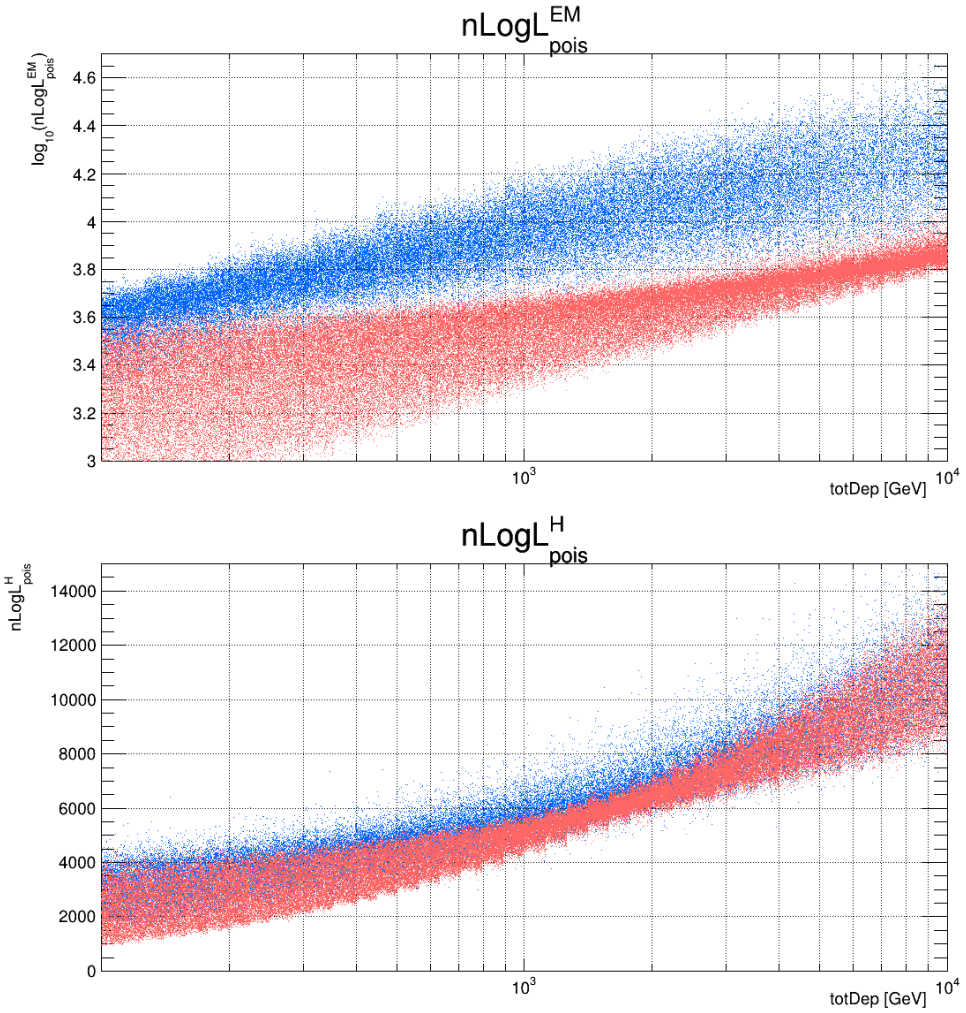

Figure 6.4: The distributions of the discrimination parameter $nLogL^{EM}_{pois}$ (top) and $nLogL^{H}_{pois}$ (bottom) for electrons (red) and protons (blue) with respect to the total deposited energy.

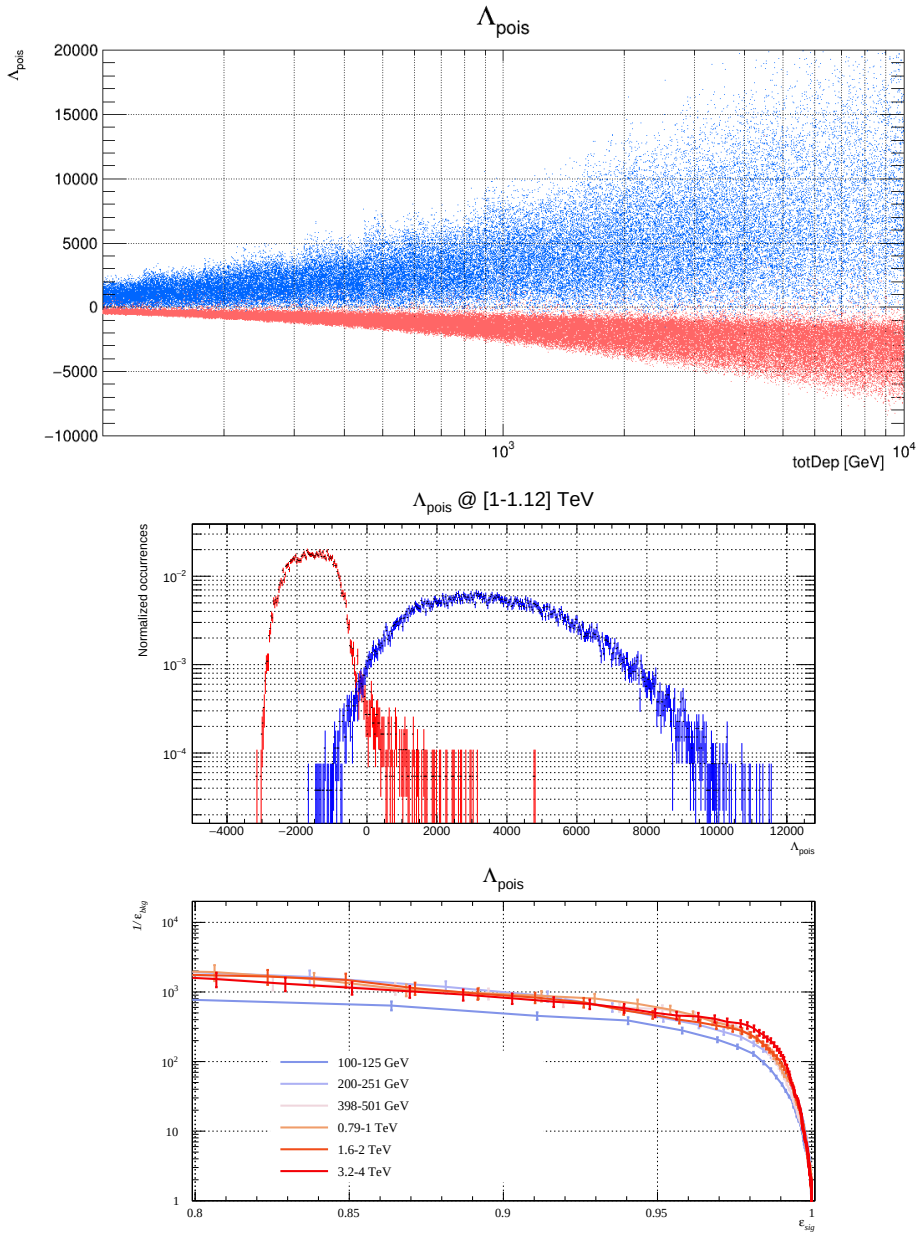

Figure 6.5: On top the distributions of the discrimination parameter Λ_{pois} for electrons (red) and protons (blue) with respect to the total deposited energy. In the middle the detail of these distributions for the reconstructed energy bin $[1, 1.12]$ TeV. At the bottom the ROC curves from some value of *totDep*.

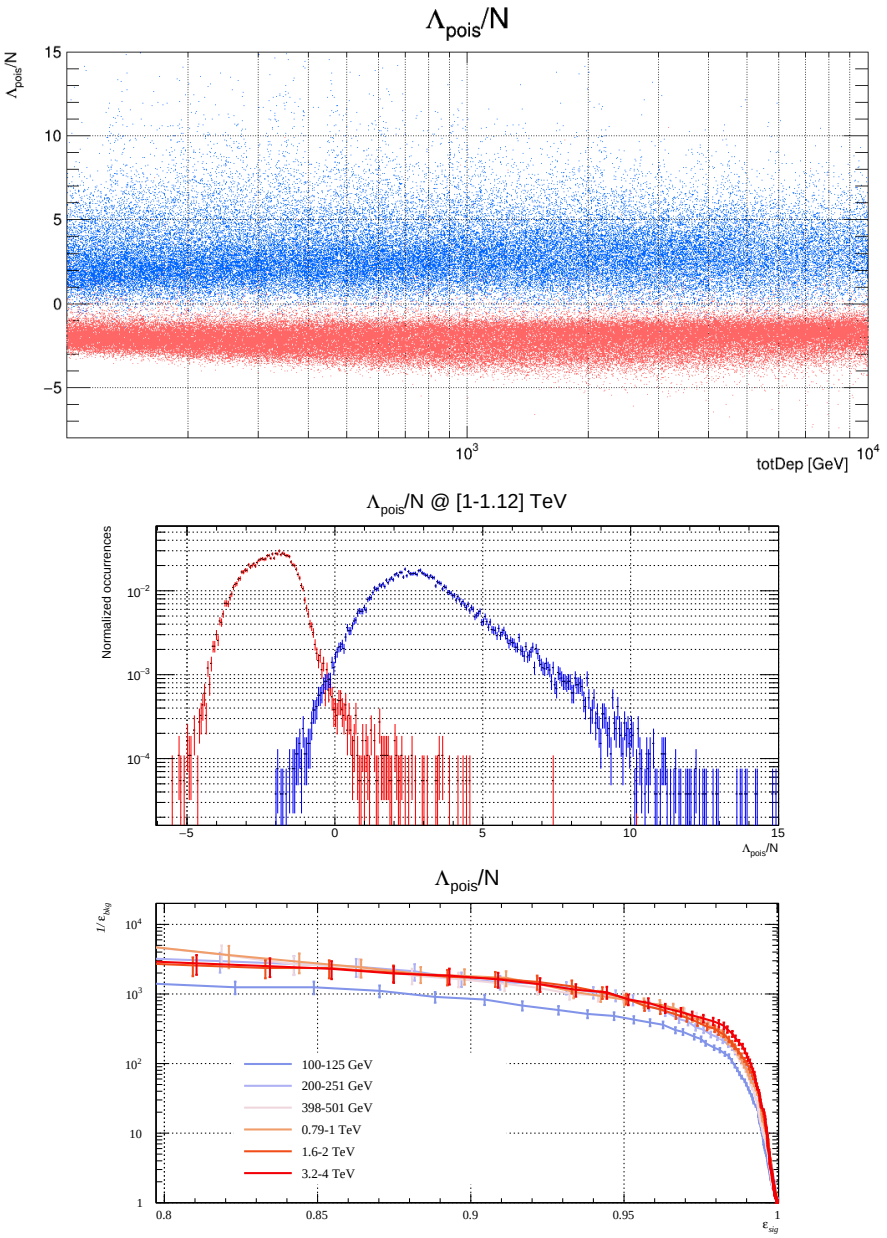

Figure 6.6: On top the distributions of the discrimination parameter Λ_{pois}/N for electrons (red) and protons (blue) with respect to the total deposited energy. In the middle the detail of these distributions for the reconstructed energy bin $[1, 1.12]$ TeV. At the bottom the ROC curves from some value of $totDep$.

distributions appear to be more irregualr than those produced by the modified Poisson approximation, showing stronger bin-to-bin fluctuations. The hadronic likelihood, however, seems to produce better separation, especially at higher energy.

For this approximation too we can evaluate a likelihood ratio Λ_{lag} that could improve the separation of electrons and protons. Fig. 6.8 shows the distributions that we obtain, together with the detail of the distributions at $totDep = [1, 1.12]$ TeV, and the ROC curves produced by the discriminator.

Fig. 6.9 shows the distributions for the normalized likelihood ratio Λ_{lag}/N and the relative detail of the distributions and ROC curves.

The background suppresion produced by Λ_{lag} is consistently below 10^3 for any signal efficiency greater than 80%, while for Λ_{lag}/N the suppression oscillates between 10^3 and 6×10^3 for ε_{sig} between 80% and 90%.

6.2.3 Mixed likelihood ratio

Since we observed that the Poisson approximation works better with the EM hypothesis, while the Laguerre polynomials approximation seems to describe better the hadronic showers fluctuation, at least at higher energies, we can try combining the likelihood that we get from these two different approximations in a single mixed parameter Λ_{pl}. Figure 6.10 show the distributions and ROC curves that we get for this metric, while figure 6.11 shows what we obtain for the same ratio divided by the number of above threshold deposits.

6.3 Mean square deviation

Another way to compare an event to the expected behavior associated to the EM or hadronic is evaluating a mean square deviation of the measured deposits from our models. We defined the quantities

$$s^{\alpha} = \frac{1}{N} \sum_{i=1}^{N} \frac{(\varepsilon_i - \mu(\alpha)_i)^2}{\sigma_i^2(\alpha)}, \tag{6.4}$$

where ε_i is the deposited radial energy density measured in the bin i, α represent either the electromagnetic (EM) or hadronic (H) hypothesis to be tested, $\mu(\alpha)_i$ is the expected energy density measured in the bin i for a shower of type α, and $\sigma_i^2(\alpha)$ is the estimated variance for such event in the corresponding bin.

Fig. 6.12 shows the distributions that we obtain evaluating such metric on the electrons (red) and protons (blue) datasets with respect to the EM hypothesis (top) and hadronic hypothesis (bottom).

The mean square deviation from the EM model seems to produce a very neat and stable separation. Fig. 6.13 shows in detail the distributions for electrons and protons in the *totDep* bin $[1, 1.12]$ TeV and the ROC curves for some examples of reconstructed energy bin. The background suppression is consistently above 10^3 for any signal efficiency $\leq$95% for all tested energies. The suppression grows to about 10^4 for $\varepsilon_{sig} < 85\%$, even if with large uncertainty due to low statistics.

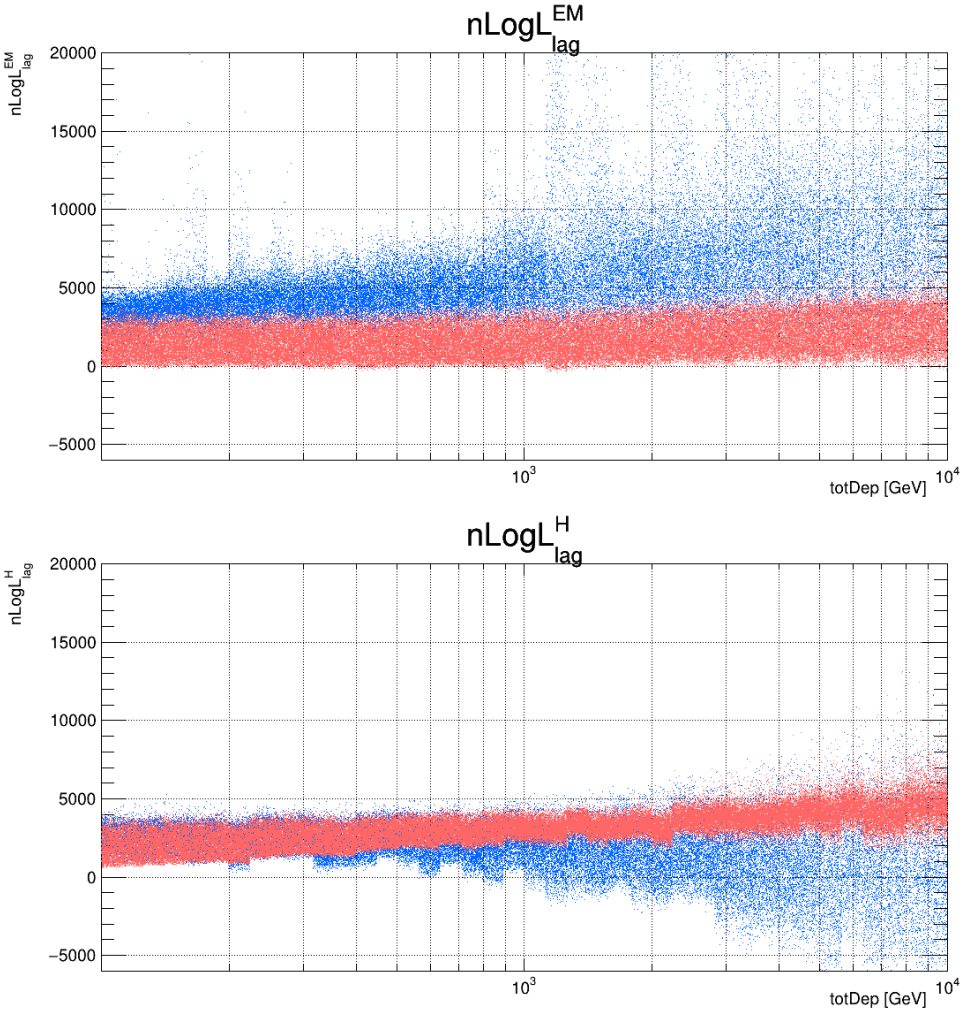

Figure 6.7: The distributions of the discrimination parameter $nLogL_{lag}^{EM}$ (top) and $nLogL_{lag}^{H}$ (bottom) for electrons (red) and protons (blue) with respect to the total deposited energy.

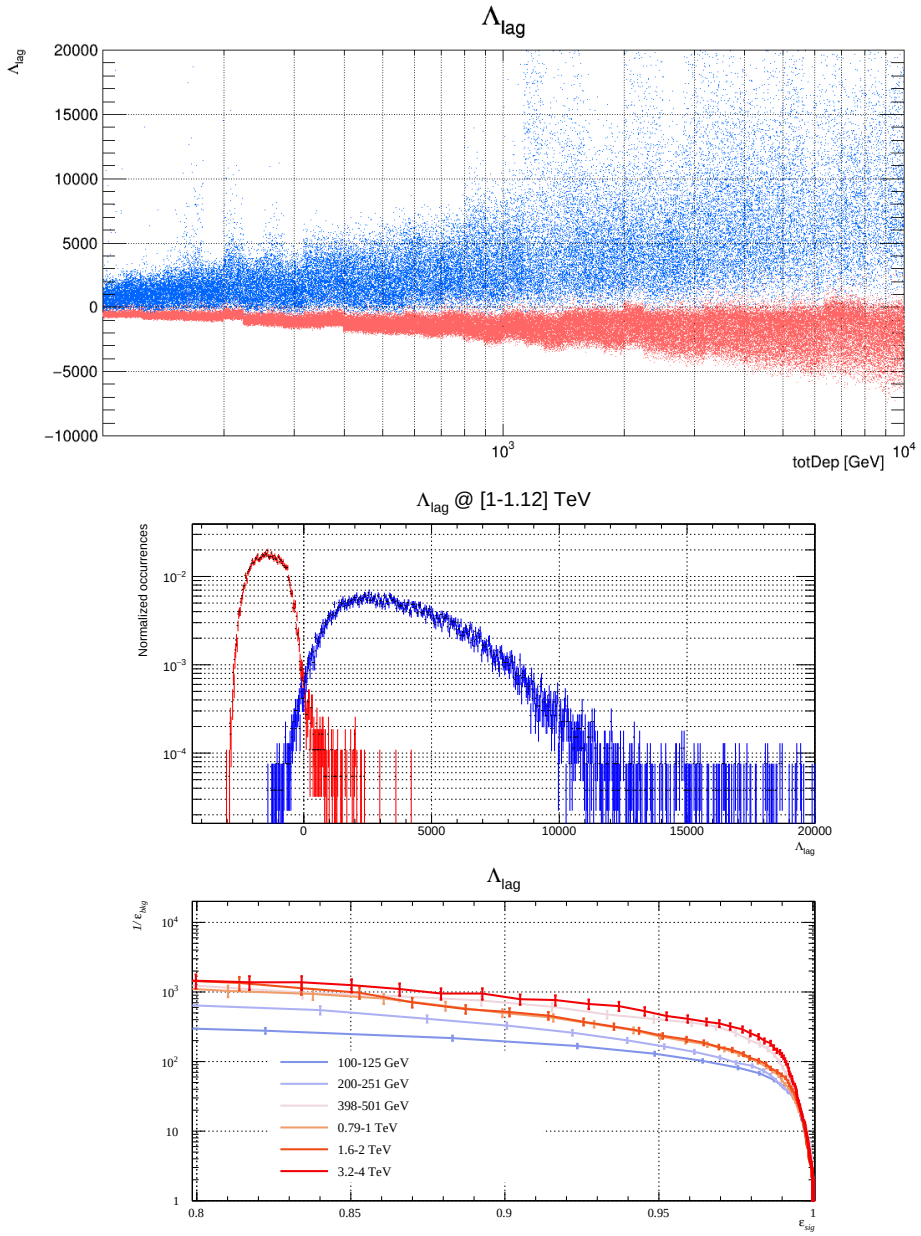

Figure 6.8: On top the distributions of the discrimination parameter Λ_{lag} for electrons (red) and protons (blue) with respect to the total deposited energy. In the middle the detail of these distributions for the reconstructed energy bin $[1, 1.12]$ TeV. At the bottom the ROC curves from some value of *totDep*.

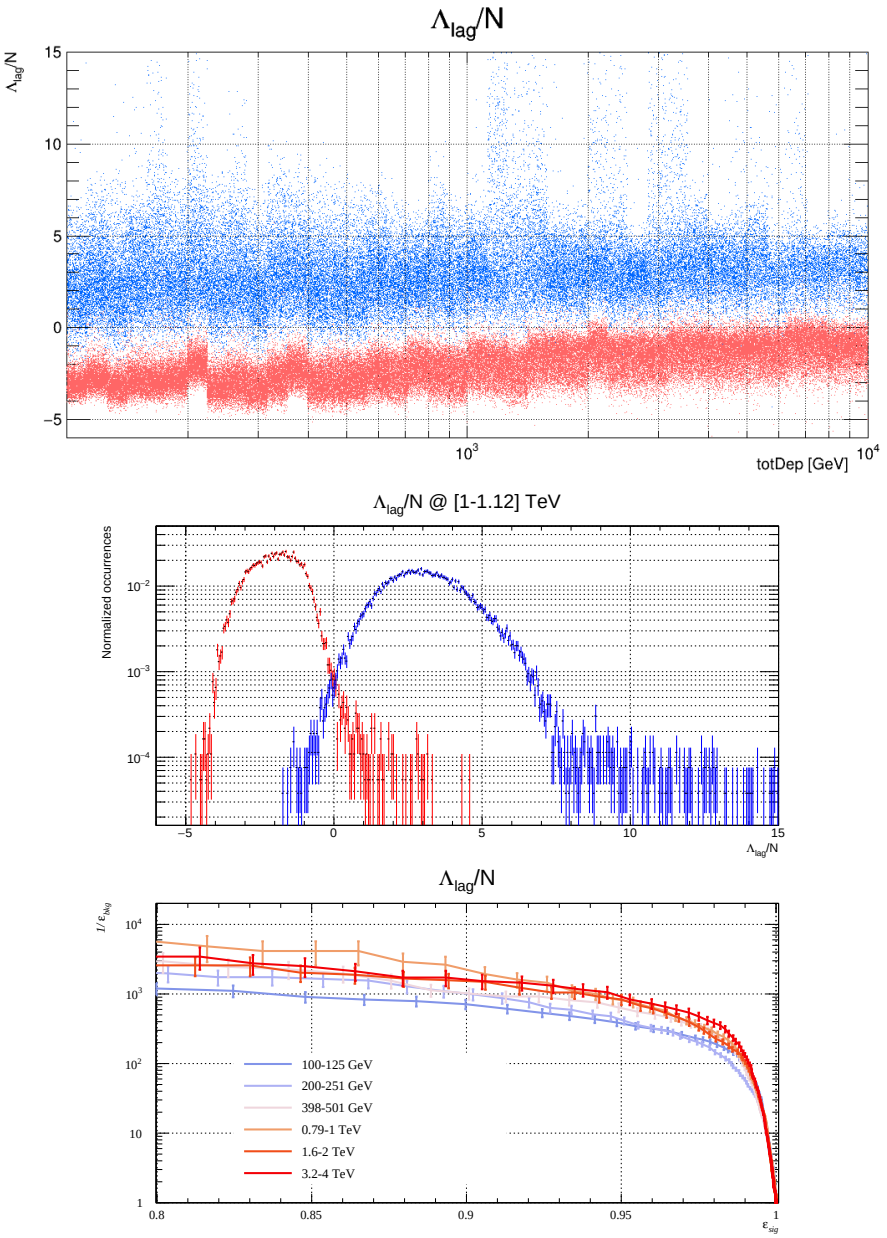

Figure 6.9: On top the distributions of the discrimination parameter Λ_{lag}/N for electrons (red) and protons (blue) with respect to the total deposited energy. In the middle the detail of these distributions for the reconstructed energy bin $[1, 1.12]$ TeV. At the bottom the ROC curves from some value of *totDep*.

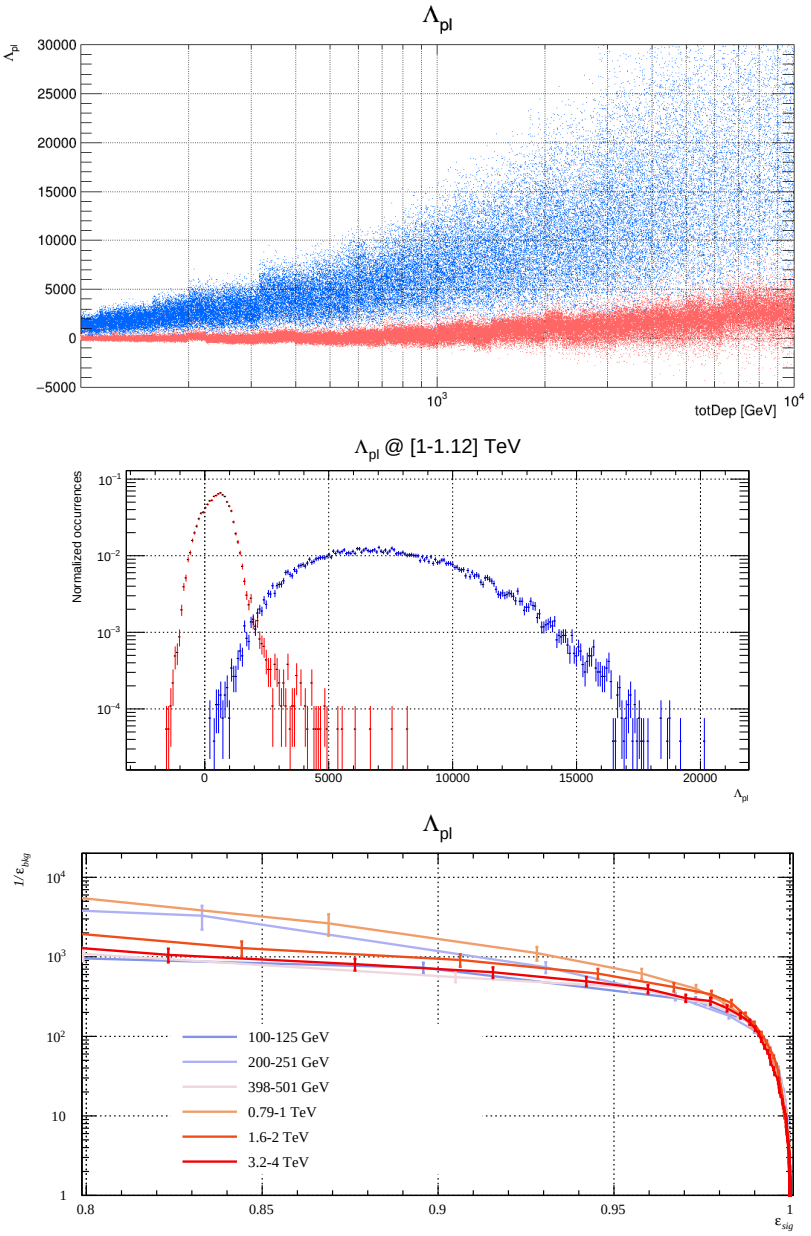

Figure 6.10: On top the distributions of the discrimination parameter Λ_{pl} for electrons (red) and protons (blue) with respect to the total deposited energy. In the middle the detail of these distributions for the reconstructed energy bin $[1, 1.12]$ TeV. At the bottom the ROC curves from some value of *totDep*.

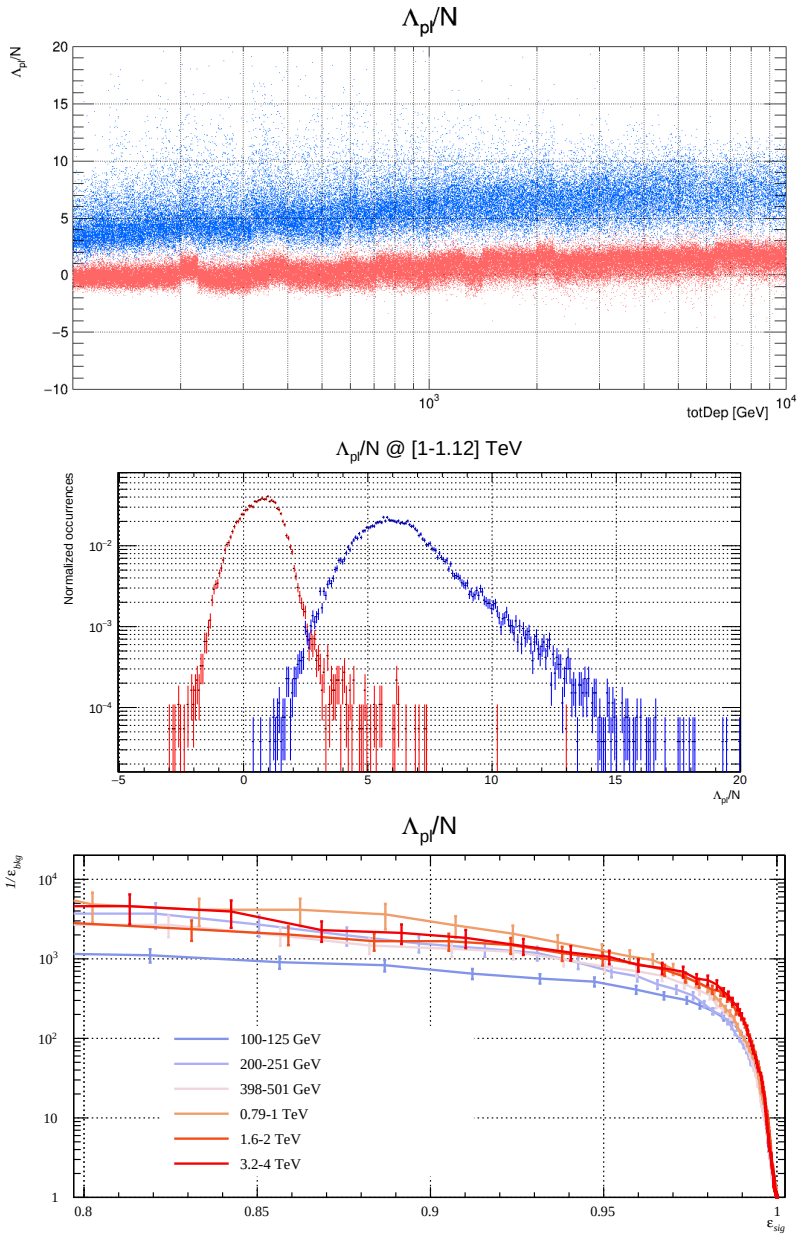

Figure 6.11: On top the distributions of the discrimination parameter Λ_{pl}/N for electrons (red) and protons (blue) with respect to the total deposited energy. In the middle the detail of these distributions for the reconstructed energy bin $[1, 1.12]$ TeV. At the bottom the ROC curves from some value of *totDep*.

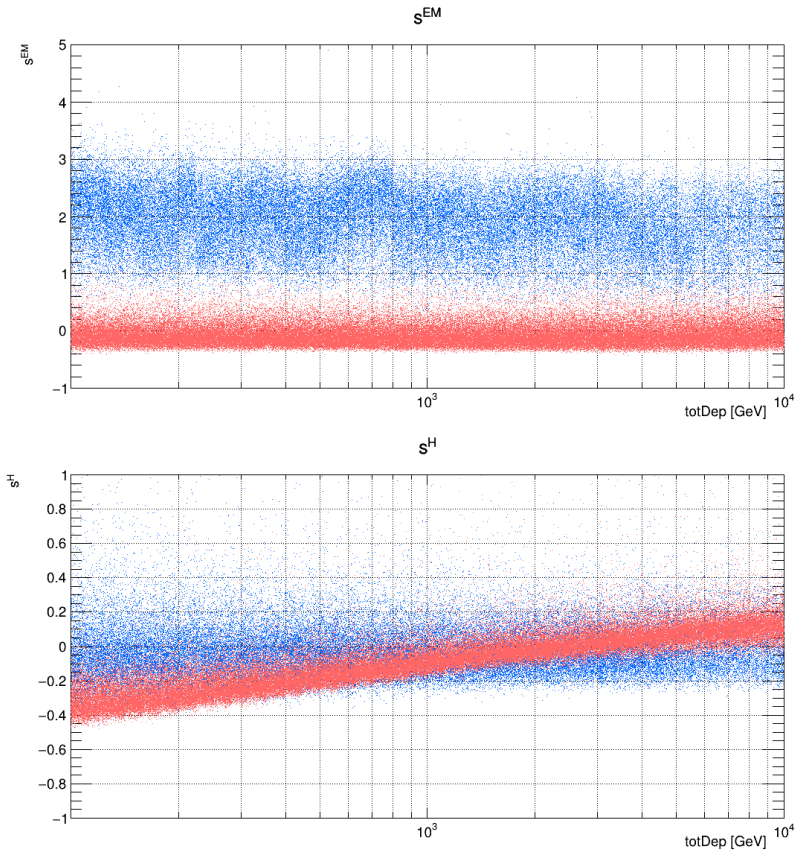

Figure 6.12: The distributions of the discrimination parameter s^{EM} (top) and s^{H} (bottom) for electrons (red) and protons (blue) with respect to the total deposited energy.

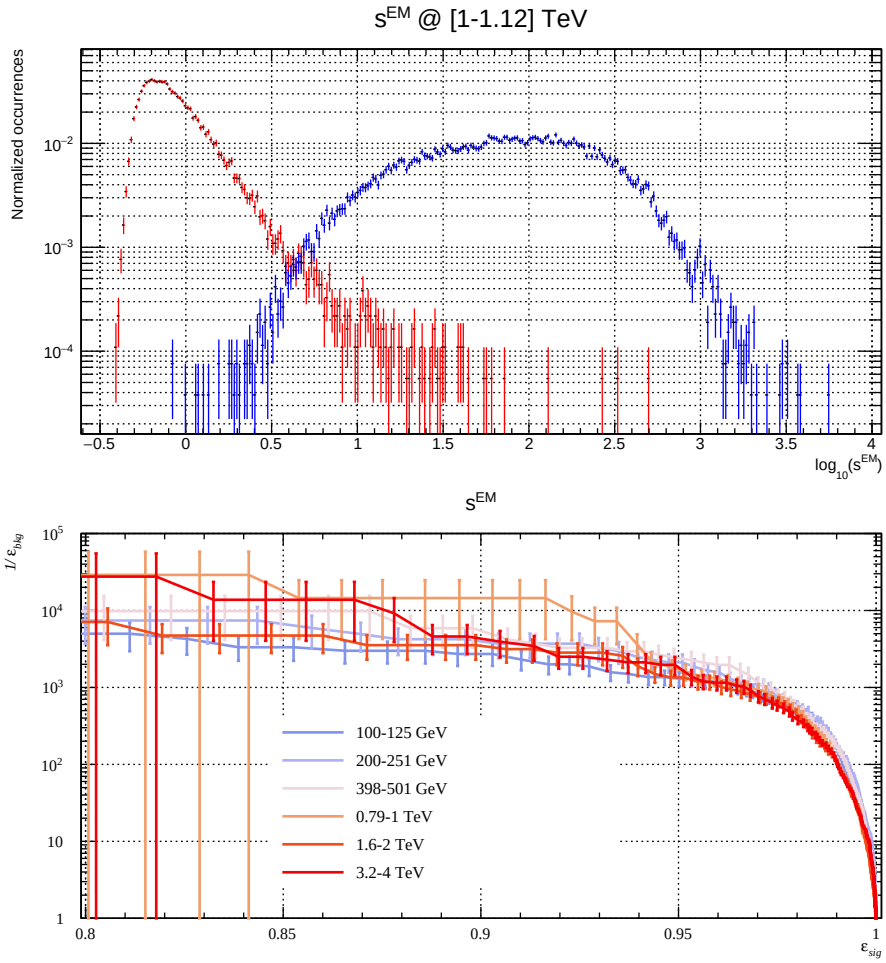

Figure 6.13: On top the distributions of the discrimination parameter s^{EM} for electrons (red) and protons (blue) at the reconstructed energy bin $[1, 1.12]$ TeV. The plot at the bottom show the ROC curves for some *totDep* bins.

Also in this case we can combine the EM hypothesis and the hadronic one into a synthetic parameter defined as

$$\chi = \frac{s^e}{s^e + s^p}, \tag{6.5}$$

Fig. 6.14 show the distributions obtained for this parameter and the ROC curves that we get using χ as a discriminator.

This parameter too produce a very strong suppression, $1/\varepsilon_{bkg} > 10^3$ for $\varepsilon_{sig} \leq 95\%$, but doesn't seem to grow as fast as s^{EM} at lower signal efficiency.

6.4 Summary

Comparing the series of discrimination parameters that we examinated we can make some observations. The parameters testing the EM hypothesis always outperform those based on the hadronic hypothesis. While combining both metrics often improves overall separation, the EM component remains the primary driver of this performance. In some case, the EM discriminator alone even surpasses the combined likelihood ratio.

This performance gap highlights the inherent difficulties in modeling hadronic events. The model's accuracy is fundamentally limited by the complexity of hadronic interactions—specifically their high variability and the presence of "contaminating" EM subshowers produced by neutral pion decays within the larger hadronic shower.

The fitted version shows a clear improvement over simpler mapping-based approximations. However, it still falls short of the performance achieved by the likelihood ratio discriminators. Interestingly, despite its mathematical simplicity, the mean square deviation remains the most effective discriminator in this study.

6.5 Comparison with CNN

We can now compare the best performance that we were able to obtain with those reached by the convolutional neural network. Figure 6.15 shows the ROC curve of s^{EM} at different energy bin compared to the ROC produced by the CNN. The background suppression of the CNN is slightly less than 10^4 at 90% signal efficiency, the suppression reached by our analysis for the same ε_{sig} oscillates between 10^3 and 10^4 just below the CNN suppresion except for some high uncertainty *totDep* bin. The bottom picture in Fig. 6.15 shows tìin detail the comparison of background suppression at different values of *totDep* for $\varepsilon_{sig} = 90\%$.

The CNN appears capable of achieving better signal efficiency for the same background suppresion, and also produce performances more stable with the energy, but its discrimination power is highly comparable with that achieved by our analysis.

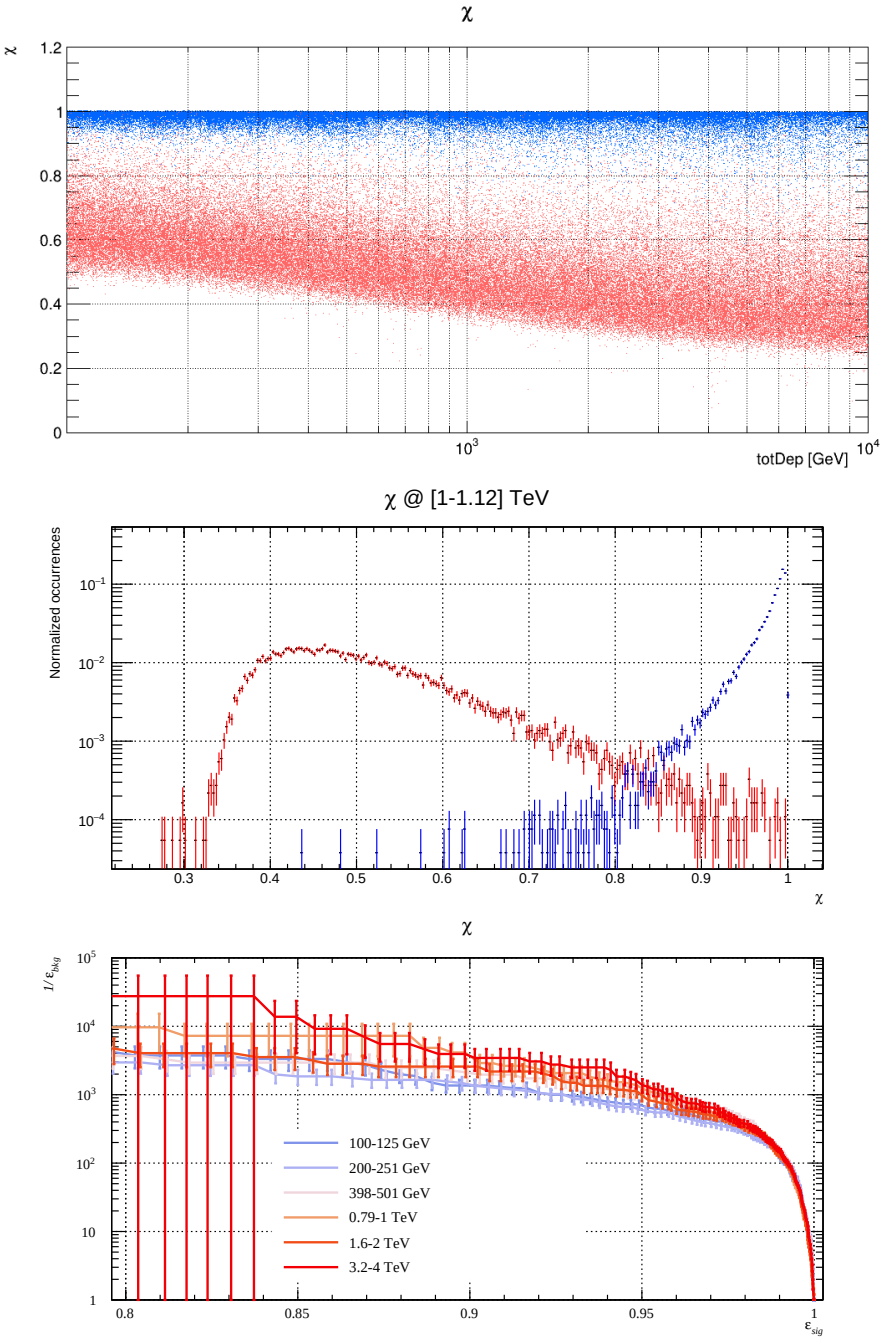

Figure 6.14: On top the distributions of the discrimination parameter χ for electrons (red) and protons (blue) with respect to the total deposited energy. In the middle the detail of these distributions for the reconstructed energy bin $[1, 1.12]$ TeV. At the bottom the ROC curves from some value of *totDep*.

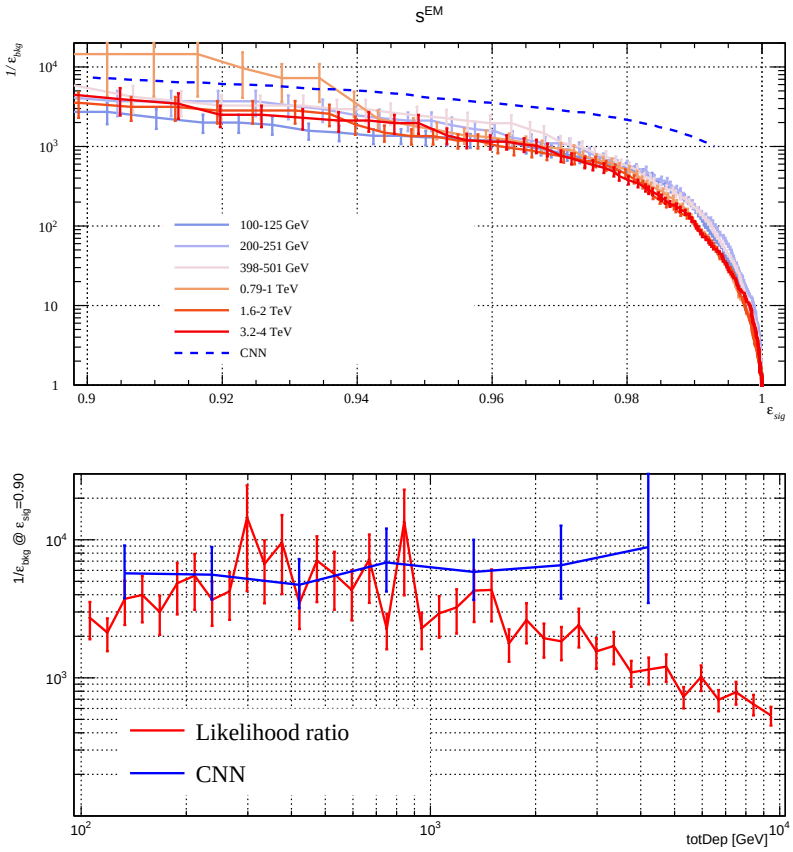

Figure 6.15: Comparison of the performance of the best discriminator obtained from our modeling and those of the convolutional neural network. The top plot shows the ROC curves. The CNN represented by the dark blue line, while the other lines represent different *totDep* bin of our model. The plot at the bottom shows the background suppression at different *totDep* for 90% signal efficiency. Blue line is the CNN, while the red line is our model.

Conclusion

The current generation of CR experiments has been providing unprecedented high precision measurement of the spectra and composition of cosmic rays that have highlighted unexpected features and properties. These have shown the limits of current CR origin, acceleration and propagation models, and have indicated that a physically motivated model to consistently describe all observed properties of cosmic rays must be developed. Current measurements, however, are limited in energy reach to hundreds of TeV for protons, and to few TeVs for electrons as consequence of the finite gathering power of operating instruments. These energy scales are however very peculiar, as they coincide for protons and nuclei to the boundary of the so-called "knee" region, actually investigated only through indirect ground-based measurements, and for which that direct space-borne measurements could possibly reveal components and spectral features to identify the nature of the structure. For electrons, instead, it coincides with a break in the maximum observed energies, possibly correlated to the maximum energy of galactic electron accelerators, although higher energy population are expected by acceleration in nearby sources. A new generation of space-borne experimental facilities will be able to access these unexplored energy regions implementing novel designs and technological solutions.

The HERD (High Energy cosmic Radiation Detector) experiment is about to inaugurate this new generation of CR detectors employing an extremely wide field of view that enables an unprecedented acceptance using a calorimetric particle detection approach. This is achieved by exploiting an innovative design of a deep 3D imaging calorimeter, that will be able to reconstruct accurately particle showers for events impinging from any direction. The calorimeter is then surrounded by other detectors for tracking and charge measurement that hermetically enclose it covering five out of six of the faces of the cubic facility.

This novel concept of 3D calorimeters will unlock new possibilities for particle identification based on the analysis of the shapes of the cascade showers generated by particles interacting in the calorimeter materials. The goal of this thesis was indeed to develop a particle identification technique employing these innovative 3D capabilities for electron/proton discrimination. This task in particular is crucial for the analysis of the electrons+positrons flux in cosmic rays because protons represent an extremely abundant background that cannot be otherwise removed through charge measurement. The approach we explored in this work was based on the construction of some models of the statistical behavior of typical EM and hadronic showers and the definition of discrimi-

nation parameters that encode the compatibility of a particular shower measured by the imaging elements of the calorimeter with the expected behavior of electromagnetic and hadronic showers.

The design of the HERD calorimeter has been used in this work as a benchmark for designing and testing a family of electron/proton discrimination tools that exploit the 3D-imaging isotropic reconstruction capabilities of next-generation CR instruments. The results produced in this work are easily extended to any other future implementations a similar calorimeter design, like those of the ALADInO and AMS-100 proposed missions.

To achieve this goal we had to simulate millions of electrons and protons and map the topological development of the average energy deposit of these showers. In order to correct for direction effects in the wide quasi-4π calorimeter acceptance, the whole shower footprint analysis has been conducted in the reference frame defined by the main shower longitudinal axis and the radial direction corresponding to the distance from such axis. In addition to the average, we mapped the further moments of the deposited energy density in order to have more information about the typical fluctuation of these deposits.

These mapped developments were used to approximate the fluctuations in the deposited energy density of the showers. We based the approximation of such functions on two methods: a modified Poisson function that can fit the expected mean and variance, and a sum of generalized Laguerre polynomials that fit an arbitrary number of moments of the distribution to approximate.

In the case of the modified Poisson approximation we also explored an attempt of modeling the average deposits through longitudinal and radial fits of the development. We employed a combination of standard models and custom parametrizations to implement a continuous function fitting the topological development of the showers. Fitting also the topological development of the fluctuation variance, we combined these function into a probability density function (PDF) of the deposited energy.

We used these approximated PDFs to evaluate the compatibility of an event with the expected electromagnetic or hadronic shower with a likelihood-based approach. We also evaluated the likelihood ratio between the electron and proton hypothesis to further improve the discrimination performances. Moreover, as another figure of accordance between tested shower and expected behavior we computed the mean square deviation of the observed energy deposit from the modeled deposits.

All these metrics were tested as discrimination parameters, and we used the background suppression at 90% signal efficiency as a figure to evaluate the performance of the metric. The comparison with electron behavior are consistently more performant than that coming from testing the proton accordance. In particular the modified Poisson approximation with the fitted model is the likelihood-based metric that produces the best separation. The likelihood ratio further improves the background rejection and, when normalized by the number of above the threshold signals produce a stable separation that ensures $> 10^3$ background suppression in the whole tested energy range.

The most performant approach in terms of proton rejection capabilities is the mean square deviation s^{EM} of the shower deposits from those expected for an electromagnetic shower. With this metric we reached a background suppression consistently $> 10^3$ for

signal efficiency $< 95\%$ and that grows to about 10^4 for 85% signal efficiency.

These performances were also compared with the rejection reached by a convolutional neural network (CNN) trained on the same dataset for the discrimination of electrons from protons. The CNN, in general, manages to achieve better signal efficiency for the same background suppression and proves to be more stable at higher energies. Nonetheless, the background suppression at 90% signal efficiency is highly compatible with our best performances.

The work showed here lays the foundations for an $e^- + e^+$ flux measurement with HERD, or a similar instrument, but also proofs the relevance of 3D imaging calorimeters as the pivot of a new generation of direct cosmic rays detectors that will focus on large acceptance telescopes. The work focused on a calorimeter-only approach, testing in depth the performances that a 3D segmented calorimeter can provide by itself in electron/proton discrimination. The performances reached were only based on the energy deposits in the calorimeter crystals, but for a complete analysis we expect to exploit also additional information from outer detectors. For instance the incoming direction of particles as measured by the external tracking system, that would improve the longitudinal shower projection; or the energy deposits in the external detectors due to shower back-splash or off-track secondaries, that would expand the available topology to study; but also other properties of the showers such as the starting point the cascade. All these different data might be studied together in a multivariate analysis that we expect to produce even higher background suppression, further improving the particle identification capabilities of the whole instrument.

Bibliography

[1] M. Amenomori et al. "Anisotropy and Corotation of Galactic Cosmic Rays". In: *Science* 314.5798 (2006), pp. 439–443. DOI: 10.1126/science.1131702. eprint: https://www.science.org/doi/pdf/10.1126/science.1131702. URL: https://www.science.org/doi/abs/10.1126/science.1131702.

[2] M Amenomori et al. "Northern sky galactic cosmic ray anisotropy between 10 and 1000 TeV with the Tibet air shower array". In: *The Astrophysical Journal* 836.2 (2017), p. 153.

[3] B Bartoli et al. "Galactic cosmic-ray anisotropy in the northern hemisphere from the ARGO-YBJ experiment during 2008–2012". In: *The Astrophysical Journal* 861.2 (2018), p. 93.

[4] AA Abdo et al. "The large-scale cosmic-ray anisotropy as observed with Milagro". In: *The Astrophysical Journal* 698.2 (2009), p. 2121.

[5] AU Abeysekara et al. "All-sky measurement of the anisotropy of cosmic rays at 10 TeV and mapping of the local interstellar magnetic field". In: *The Astrophysical Journal* 871.1 (2019), p. 96.

[6] MG Aartsen et al. "Anisotropy in cosmic-ray arrival directions in the southern hemisphere based on six years of data from the IceCube detector". In: *The Astrophysical Journal* 826.2 (2016), p. 220.

[7] Alexander Aab et al. "Large-scale cosmic-ray anisotropies above 4 EeV measured by the Pierre Auger Observatory". In: *The Astrophysical Journal* 868.1 (2018), p. 4.

[8] AA Abdo et al. "Discovery of localized regions of excess 10-TeV cosmic rays". In: *Physical Review Letters* 101.22 (2008), p. 221101.

[9] Bruno Bartoli et al. "Medium scale anisotropy in the TeV cosmic ray flux observed by ARGO-YBJ". In: *Physical Review D—Particles, Fields, Gravitation, and Cosmology* 88.8 (2013), p. 082001.

[10] AU Abeysekara et al. "Observation of small-scale anisotropy in the arrival direction distribution of TeV cosmic rays with HAWC". In: *The Astrophysical Journal* 796.2 (2014), p. 108.

[11] David Maurin et al. "A cosmic-ray database update: CRDB v4.1". In: *The European Physical Journal C* 83.10 (Oct. 2023). ISSN: 1434-6052. DOI: 10.1140/epjc/s10052-023-12092-8. URL: http://dx.doi.org/10.1140/epjc/s10052-023-12092-8.

[12] M. Ackermann et al. "Detection of the Characteristic Pion-Decay Signature in Supernova Remnants". In: *Science* 339.6121 (2013), pp. 807–811. DOI: 10.1126/science.1231160. eprint: https://www.science.org/doi/pdf/10.1126/science.1231160. URL: https://www.science.org/doi/abs/10.1126/science.1231160.

[13] Duncan R. Lorimer and Michael Kramer. "Handbook of Pulsar Astronomy". In: 2004. URL: https://api.semanticscholar.org/CorpusID:116894520.

[14] D. Schuckardt. "Limits on the dipole anisotropy in the flux of cosmic ray leptons with ams-02". PhD thesis. Institute for Experimental Nuclear Physics (IEKP), 2014.

[15] F. A. Aharonian, S. V. Bogovalov, and D. Khangulyan. "Abrupt acceleration of a cold ultrarelativistic wind from the Crab pulsar". In: *Nature* 482.7386 (2012), pp. 507–509. ISSN: 1476-4687. DOI: 10.1038/nature10793. URL: https://doi.org/10.1038/nature10793.

[16] Pasquale Blasi and Elena Amato. "Positrons from pulsar winds". In: *High-Energy Emission from Pulsars and their Systems: Proceedings of the First Session of the Sant Cugat Forum on Astrophysics*. Springer. 2010, pp. 623–641.

[17] FA Aharonian, SV Bogovalov, and Dmitry Khangulyan. "Abrupt acceleration of a cold ultra-relativistic wind from the Crab pulsar". In: *Nature* 482.7386 (2012), pp. 507–509.

[18] Duncan Ross Lorimer and Michael Kramer. *Handbook of pulsar astronomy*. Vol. 4. Cambridge university press, 2005.

[19] Rainer Beck. "Galactic and extragalactic magnetic fields". In: *AIP Conference Proceedings*. Vol. 1085. 1. American Institute of Physics. 2008, pp. 83–96.

[20] D Breitschwerdt, JF McKenzie, and HJ Voelk. "Galactic winds. I-Cosmic ray and wave-driven winds from the Galaxy". In: *Astronomy and Astrophysics (ISSN 0004-6361), vol. 245, no. 1, May 1991, p. 79-98.* 245 (1991), pp. 79–98.

[21] Sarah Recchia. "Cosmic ray driven galactic winds". In: *International Journal of Modern Physics D* 29.07 (2020), p. 2030006.

[22] R Cowsik et al. "Steady State of Cosmic-Ray Nuclei—Their Spectral Shape and Path Length at Low Energies". In: *Physical Review* 167.5 (1968), p. 1545.

[23] Putze, A., Derome, L., and Maurin, D. "A Markov Chain Monte Carlo technique to sample transport and source parameters of Galactic cosmic rays - II. Results for the diffusion model combining B/C and radioactive nuclei". In: *AA* 516 (2010), A66. DOI: 10.1051/0004-6361/201014010. URL: https://doi.org/10.1051/0004-6361/201014010.

[24] A.E. Vladimirov et al. "GALPROP WebRun: An internet-based service for calculating galactic cosmic ray propagation and associated photon emissions". In: *Computer Physics Communications* 182.5 (2011), pp. 1156–1161. ISSN: 0010-4655. DOI: https://doi.org/10.1016/j.cpc.2011.01.017. URL: https://www.sciencedirect.com/science/article/pii/S0010465511000373.

[25] Carmelo Evoli et al. "Cosmic-ray propagation with DRAGON2: I. numerical solver and astrophysical ingredients". In: *Journal of Cosmology and Astroparticle Physics* 2017.02 (Feb. 2017), p. 015. DOI: 10.1088/1475-7516/2017/02/015. URL: https://doi.org/10.1088/1475-7516/2017/02/015.

[26] Iris Gebauer. "An anisotropic model for galactic cosmic ray transport and its implications for indirect dark matter searches". Dissertation. Karlsruhe, Germany: Karlsruher Institut für Technologie, 2010.

[27] F. Zwicky. "On the Masses of Nebulae and of Clusters of Nebulae". In: *ApJ* 86 (Oct. 1937), p. 217. DOI: 10.1086/143864.

[28] Fritz Zwicky. "Die rotverschiebung von extragalaktischen nebeln". In: *Helvetica Physica Acta, Vol. 6, p. 110-127* 6 (1933), pp. 110–127.

[29] Yoshiaki Sofue and Vera Rubin. "Rotation curves of spiral galaxies". In: *Annual Review of Astronomy and Astrophysics* 39.1 (2001), pp. 137–174.

[30] Vera C Rubin and W Kent Ford Jr. "Rotation of the Andromeda nebula from a spectroscopic survey of emission regions". In: *Astrophysical Journal, vol. 159, p. 379* 159 (1970), p. 379.

[31] Peter W Graham et al. "Towards a Bullet-proof test for indirect signals of dark matter". In: *Physical Review D* 91.10 (2015), p. 103524.

[32] Mordehai Milgrom. "A modification of the Newtonian dynamics as a possible alternative to the hidden mass hypothesis". In: *Astrophysical Journal, Part 1 (ISSN 0004-637X), vol. 270, July 15, 1983, p. 365-370. Research supported by the US-Israel Binational Science Foundation.* 270 (1983), pp. 365–370.

[33] Naoshi Sugiyama. "Introduction to temperature anisotropies of Cosmic Microwave Background radiation". In: *Progress of Theoretical and Experimental Physics* 2014.6 (2014), 06B101.

[34] Rachel S Somerville and Greg L Bryan. "Large-scale structure with cold dark matter". In: *Nature Astronomy* 3.12 (2019), pp. 1058–1059.

[35] Diego Blas et al. "Large scale structure from viscous dark matter". In: *Journal of Cosmology and Astroparticle Physics* 2015.11 (2015), p. 049.

[36] Stefano Scopel. "Particle dark matter candidates". In: *Journal of Physics: Conference Series*. Vol. 120. 4. IOP Publishing. 2008, p. 042003.

[37] Alessandro Bottino et al. "Neutralino as a candidate for cold dark matter". In: *Nuclear Physics B-Proceedings Supplements* 31 (1993), pp. 359–364.

[38] Giorgio Arcadi et al. "The waning of the WIMP: endgame?" In: *The European Physical Journal C* 85.2 (2025), p. 152.

[39] Daniel Abercrombie, Annapaola de Cosa, et al. "Dark Matter benchmark models for early LHC Run-2 Searches: Report of the ATLAS/CMS Dark Matter". In: ().

[40] Adhikari Collaboration et al. "Three-year annual modulation search with COSINE-100". In: *Physical Review D* 106 (2022).

[41] Farinaldo S Queiroz and Clarissa Siqueira. "Search for semi-annihilating dark matter with Fermi-LAT, HESS, Planck, and the Cherenkov Telescope Array". In: *Journal of Cosmology and Astroparticle Physics* 2019.04 (2019), p. 048.

[42] Ralph Bird. "The GAPS experiment to search for dark matter using low-energy antimatter". In: *42nd COSPAR Scientific Assembly* 42 (2018), E1–5.

[43] Andrea Albert et al. "Searching for dark matter annihilation in recently discovered Milky Way satellites with Fermi-LAT". In: *The Astrophysical Journal* 834.2 (2017), p. 110.

[44] Jin Chang et al. "The dark matter particle explorer mission". In: *Astroparticle Physics* 95 (2017), pp. 6–24.

[45] Pierre Salati. "Indirect Dark Matter searches in the light of the recent AMS-02 observations". In: *Particle Physics at the Year of Light: Proceedings of the Seventeenth Lomonosov Conference on Elementary Particle Physics*. World Scientific. 2017, pp. 305–311.

[46] K Scholberg. "Indirect dark matter searches with AMS-02". In: *Nuclear Physics B Proceedings Supplements* 138 (2005), pp. 35–37.

[47] Carlos Pérez de los Heros. "Status, challenges and directions in indirect dark matter searches". In: *Symmetry* 12.10 (2020), p. 1648.

[48] Fiorenza Donato. "Indirect searches for dark matter". In: *Physics of the Dark Universe* 4 (2014), pp. 41–43.

[49] M Aguilar et al. "Antiproton flux, antiproton-to-proton flux ratio, and properties of elementary particle fluxes in primary cosmic rays measured with the alpha magnetic spectrometer on the international space station". In: *Physical Review Letters* 117.9 (2016), p. 091103.

[50] Ilias Cholis, Tim Linden, and Dan Hooper. "A robust excess in the cosmic-ray antiproton spectrum: Implications for annihilating dark matter". In: *Physical Review D* 99.10 (2019), p. 103026.

[51] Alessandro Cuoco et al. "Scrutinizing the evidence for dark matter in cosmic-ray antiprotons". In: *Physical Review D* 99.10 (2019), p. 103014.

[52] Gaëlle Giesen et al. "AMS-02 antiprotons, at last! Secondary astrophysical component and immediate implications for Dark Matter". In: *Journal of Cosmology and Astroparticle Physics* 2015.09 (Sept. 2015), p. 023. DOI: 10.1088/1475-7516/2015/09/023. URL: https://doi.org/10.1088/1475-7516/2015/09/023.

[53] Zhi-Cheng Tang et al. "On the detectability of Galactic dark matter annihilation into monochromatic gamma-rays". In: *Chinese Physics C* 35.8 (2011), p. 725.

[54] Michele Doro. "A review of the past and present MAGIC dark matter search program and a glimpse at the future". In: *arXiv preprint arXiv:1701.05702* (2017).

[55] Chiara Giuri. "VERITAS Dark Matter search in dwarf spheroidal galaxies: an extended analysis". In: *arXiv preprint arXiv:2108.06083* (2021).

[56] Lucia Rinchiuso. "Latest results on dark matter searches with HESS". In: *EPJ Web of Conferences*. Vol. 209. EDP Sciences. 2019, p. 01023.

[57] Matthew Wood et al. "Dark matter searches with the Fermi-LAT in the direction of dwarf spheroidals". In: *arXiv preprint arXiv:1507.03530* (2015).

[58] Hasan Yüksel et al. "Neutrino constraints on the dark matter total annihilation cross section". In: *Physical Review D—Particles, Fields, Gravitation, and Cosmology* 76.12 (2007), p. 123506.

[59] John F Beacom, Nicole F Bell, and Gregory D Mack. "Upper bound on the dark matter total annihilation cross section". In: *Physical Review Letters* 99.23 (2007), p. 231301.

[60] A M Galper et al. "The PAMELA experiment: a decade of Cosmic Ray Physics in space". In: *Journal of Physics: Conference Series* 798.1 (Jan. 2017), p. 012033. DOI: 10.1088/1742-6596/798/1/012033. URL: https://doi.org/10.1088/1742-6596/798/1/012033.

[61] Jorge Casaus. "The AMS-02 experiment on the ISS". In: *Journal of Physics: Conference Series* 171.1 (June 2009), p. 012045. DOI: 10.1088/1742-6596/171/1/012045. URL: https://doi.org/10.1088/1742-6596/171/1/012045.

[62] W. B. Atwood et al. "THE LARGE AREA TELESCOPE ON THE FERMI GAMMA-RAY SPACE TELESCOPE MISSION". In: *The Astrophysical Journal* 697.2 (May 2009), p. 1071. DOI: 10.1088/0004-637X/697/2/1071. URL: https://doi.org/10.1088/0004-637X/697/2/1071.

[63] Markus Ackermann et al. "Measurement of Separate Cosmic-Ray Electron and Positron Spectra with the Fermi Large Area Telescope". In: *Physical review letters* 108.1 (2012), p. 011103.

[64] O Adriani et al. "The CALorimetric Electron Telescope (CALET) for high-energy astroparticle physics on the International Space Station". In: *Journal of Physics: Conference Series* 632.1 (July 2015), p. 012023. DOI: 10.1088/1742-6596/632/1/012023. URL: https://doi.org/10.1088/1742-6596/632/1/012023.

[65] J. Chang et al. "The DArk Matter Particle Explorer mission". In: *Astroparticle Physics* 95 (2017), pp. 6–24. ISSN: 0927-6505. DOI: https://doi.org/10.1016/j.astropartphys.2017.08.005. URL: https://www.sciencedirect.com/science/article/pii/S0927650517300841.

[66] T Kobayashi et al. "The most likely sources of high-energy cosmic-ray electrons in supernova remnants". In: *The Astrophysical Journal* 601.1 (2004), p. 340.

[67] Michael S Turner and Frank Wilczek. "Positron line radiation as a signature of particle dark matter in the halo". In: *Physical Review D* 42.4 (1990), p. 1001.

[68] M. Aguilar et al. "Towards Understanding the Origin of Cosmic-Ray Positrons". In: *Phys. Rev. Lett.* 122 (4 Jan. 2019), p. 041102. DOI: 10.1103/PhysRevLett.122.041102. URL: https://link.aps.org/doi/10.1103/PhysRevLett.122.041102.

[69] "The Pierre Auger Cosmic Ray Observatory". In: *Nuclear Instruments and Methods in Physics Research Section A: Accelerators, Spectrometers, Detectors and Associated Equipment* 798 (2015), pp. 172–213. ISSN: 0168-9002. DOI: https://doi.org/10.1016/j.nima.2015.06.058. URL: https://www.sciencedirect.com/science/article/pii/S0168900215008086.

[70] H. Kawai et al. "Telescope Array Experiment". In: *Nuclear Physics B - Proceedings Supplements* 175-176 (2008). Proceedings of the XIV International Symposium on Very High Energy Cosmic Ray Interactions, pp. 221–226. ISSN: 0920-5632. DOI: https://doi.org/10.1016/j.nuclphysbps.2007.11.002. URL: https://www.sciencedirect.com/science/article/pii/S0920563207007992.

[71] Carmen Baixeras, Magic Collaboration, et al. "The MAGIC telescope". In: *Nuclear Physics B-Proceedings Supplements* 114 (2003), pp. 247–252.

[72] Stefan Ohm, Stefan Wagner, HESS Collaboration, et al. "Current status and operation of the HESS array of imaging atmospheric Cherenkov telescopes". In: *Nuclear Instruments and Methods in Physics Research Section A: Accelerators, Spectrometers, Detectors and Associated Equipment* 1055 (2023), p. 168442.

[73] Jamie Holder et al. "The first VERITAS telescope". In: *Astroparticle Physics* 25.6 (2006), pp. 391–401.

[74] Oscar Adriani et al. "Design of an Antimatter Large Acceptance Detector In Orbit (ALADInO)". In: *Instruments* 6.2 (2022). ISSN: 2410-390X. DOI: 10.3390/instruments6020019. URL: https://www.mdpi.com/2410-390X/6/2/19.

[75] P.S. Marrocchesi. "MOONRAY: A permanent high-energy cosmic-ray observatory on the surface of the Moon". In: *Astroparticle Physics* 152 (2023), p. 102879. ISSN: 0927-6505. DOI: https://doi.org/10.1016/j.astropartphys.2023.102879. URL: https://www.sciencedirect.com/science/article/pii/S0927650523000658.

[76] TG Guzik et al. "The ATIC long duration balloon project". In: *Advances in Space Research* 33.10 (2004), pp. 1763–1770.

[77] JW Mitchell et al. "The BESS program". In: *Nuclear Physics B-Proceedings Supplements* 134 (2004), pp. 31–38.

[78] ES Seo et al. "Cosmic-ray energetics and mass (CREAM) balloon project". In: *Advances in Space Research* 33.10 (2004), pp. 1777–1785.

[79] W. R. Binns et al. "THE SuperTIGER INSTRUMENT: MEASUREMENT OF ELEMENTAL ABUNDANCES OF ULTRA-HEAVY GALACTIC COSMIC RAYS". In: *The Astrophysical Journal* 788.1 (2014), p. 18. DOI: 10.1088/0004-637X/788/1/18. URL: https://doi.org/10.1088/0004-637X/788/1/18.

[80] K McBride et al. "Towards Isotopic Composition of Cosmic Rays with the HELIX Balloon Project". In: *39th International Cosmic Ray Conference*. 2026, p. 85.

[81] G. Osteria. "GAPS: A balloon-borne cosmic-ray antimatter experiment". In: *Nuclear Instruments and Methods in Physics Research Section A: Accelerators, Spectrometers, Detectors and Associated Equipment* 958 (2020). Proceedings of the Vienna Conference on Instrumentation 2019, p. 162201. ISSN: 0168-9002. DOI: https://doi.org/10.1016/j.nima.2019.05.042. URL: https://www.sciencedirect.com/science/article/pii/S0168900219306746.

[82] B. Alpat et al. "The internal alignment and position resolution of the AMS-02 silicon tracker determined with cosmic-ray muons". In: *Nuclear Instruments and Methods in Physics Research Section A: Accelerators, Spectrometers, Detectors and Associated Equipment* 613.2 (2010), pp. 207–217. ISSN: 0168-9002. DOI: https://doi.org/10.1016/j.nima.2009.11.065. URL: https://www.sciencedirect.com/science/article/pii/S0168900209022803.

[83] Paolo W. Cattaneo. "The space station based detector HERD: precise high energy cosmic rays physics and multimessenger astronomy". In: *Nuclear and Particle Physics Proceedings* 306-308 (2019). CRIS 2018 "Entering the Era of Multi-Messenger Astronomy", pp. 85–91. ISSN: 2405-6014. DOI: https://doi.org/10.1016/j.nuclphysbps.2019.07.013. URL: https://www.sciencedirect.com/science/article/pii/S2405601419300951.

[84] S. Schael et al. "AMS-100: The next generation magnetic spectrometer in space – An international science platform for physics and astrophysics at Lagrange point 2". In: *Nuclear Instruments and Methods in Physics Research Section A: Accelerators, Spectrometers, Detectors and Associated Equipment* 944 (2019), p. 162561. ISSN: 0168-9002. DOI: https://doi.org/10.1016/j.nima.2019.162561. URL: https://www.sciencedirect.com/science/article/pii/S0168900219310848.

[85] O. Adriani et al. "Performance assessment of the HERD calorimeter with a photodiode read-out system for high-energy electron beams". In: *Journal of Instrumentation* 20.02 (2025), P02015. DOI: 10.1088/1748-0221/20/02/P02015. URL: https://doi.org/10.1088/1748-0221/20/02/P02015.

[86] O. Adriani et al. "The HERD calorimeter: prototype response to high energy nuclei". In: *Journal of Instrumentation* 20.08 (2025), P08034. DOI: 10.1088/1748-0221/20/08/P08034. URL: https://doi.org/10.1088/1748-0221/20/08/P08034.

[87] E Berti et al. "CaloCube: a new concept calorimeter for the detection of high energy cosmic rays in space". In: *Journal of Physics: Conference Series* 1162 (Jan. 2019), p. 012042. DOI: 10.1088/1742-6596/1162/1/012042. URL: https://doi.org/10.1088/1742-6596/1162/1/012042.

[88] G. Silvestre and on behalf of the HERD SCD collaboration. "The Silicon Charge Detector of the High Energy Cosmic Radiation Detection experiment". In: *Journal of Instrumentation* 19.03 (2024), p. C03042. DOI: 10.1088/1748-0221/19/03/C03042. URL: https://doi.org/10.1088/1748-0221/19/03/C03042.

[89] Dimitrios Kyratzis et al. "The Plastic Scintillator Detector of the HERD space mission". In: *POS PROCEEDINGS OF SCIENCE* 395 (2022).

[90] F. Gargano et al. "The Plastic Scintillator Detector for the future High Energy cosmic-Radiation Detection facility on board the Chinese Space Station". In: *Journal of Instrumentation* 20.07 (2025), p. C07014. DOI: 10.1088/1748-0221/20/07/C07014. URL: https://doi.org/10.1088/1748-0221/20/07/C07014.

[91] Liankun Zou et al. "Nuclear fragmentation vertex reconstruction for the HERD experiment". In: *Radiation Detection Technology and Methods* (2026), pp. 1–11.

[92] Bo Huang et al. "Side-On transition radiation detector: A detector prototype for TeV energy scale calibration of calorimeters in space". In: *Nuclear Instruments and Methods in Physics Research Section A: Accelerators, Spectrometers, Detectors and Associated Equipment* 962 (2020), p. 163723. ISSN: 0168-9002. DOI: https://doi.org/10.1016/j.nima.2020.163723. URL: https://www.sciencedirect.com/science/article/pii/S0168900220302758.

[93] Jieyu Zhu et al. "Front-End Electronics Design for the Transition Radiation Detector Prototype in the HERD". In: *IEEE Transactions on Nuclear Science* (2024).

[94] Magnus Dam et al. "Design and Modeling of AMaSED-2: A High Temperature Superconducting Demonstrator Coil for the Space Spectrometer ARCOS". In: *IEEE Transactions on Applied Superconductivity* 32.4 (2022), pp. 1–5. DOI: 10.1109/TASC.2022.3146221.

[95] Javier Berdugo et al. "Determination of the rigidity scale of the Alpha Magnetic Spectrometer". In: *Nuclear Instruments and Methods in Physics Research Section A: Accelerators, Spectrometers, Detectors and Associated Equipment* 869 (2017), pp. 10–14.

[96] Jing-jing Zang, Chuan Yue, and Xiang Li. "Measurement of absolute energy scale of ECAL of DAMPE with geomagnetic rigidity cutoff". In: *Proceedings of the 35th International Cosmic Ray Conference—PoS (ICRC2017), Bexco, Korea*. 2017, pp. 12–20.

[97] O Adriani et al. "Energy spectrum of cosmic-ray electron and positron from 10 GeV to 3 TeV observed with the calorimetric electron telescope on the international space station". In: *Physical review letters* 119.18 (2017), p. 181101.

[98] Bruno Rossi and Kenneth Greisen. "Cosmic-Ray Theory". In: *Rev. Mod. Phys.* 13 (4 Oct. 1941), pp. 240–309. DOI: 10.1103/RevModPhys.13.240. URL: https://link.aps.org/doi/10.1103/RevModPhys.13.240.

[99] Egidio Longo and Ignazio Sestili. "Monte Carlo calculation of photon-initiated electromagnetic showers in lead glass". In: *Nuclear Instruments and Methods* 128.2 (1975), pp. 283–307.

[100] Gert Moliere. In: *Zeitschrift für Naturforschung A* 3.2 (1948), pp. 78–97. DOI: doi:10.1515/zna-1948-0203. URL: https://doi.org/10.1515/zna-1948-0203.

[101] S Iwata. *Calorimeter*. Tech. rep. Nagoya Univ., 1980.

[102] Richard Wigmans. *Calorimetry: Energy measurement in particle physics*. Oxford University Press, 2000.

[103] D. Krasnopevtsev et al. "Identification of positrons and electrons at TeV energy scale using the AMS tracker, time-of-flight counters, and electromagnetic calorimeter". In: *Nuclear Instruments and Methods in Physics Research Section A: Accelerators, Spectrometers, Detectors and Associated Equipment* 1069 (2024), p. 169957. ISSN: 0168-9002. DOI: https://doi.org/10.1016/j.nima.2024.169957. URL: https://www.sciencedirect.com/science/article/pii/S0168900224008830.

[104] L Basara, AMS-02 Collaboration, et al. "Proton-electron discrimination with the ams-02 electromagnetic calorimeter". In: *33rd* (2013).

[105] O. Adriani et al. "The CALOCUBE project for a space based cosmic ray experiment: design, construction, and first performance of a high granularity calorimeter prototype". In: *Journal of Instrumentation* 14.11 (Nov. 2019), P11004. DOI: 10.1088/1748-0221/14/11/P11004. URL: https://doi.org/10.1088/1748-0221/14/11/P11004.

[106] R. D'Alessandro et al. "Calocube - A highly segmented calorimeter for a space based experiment". In: *Nuclear Instruments and Methods in Physics Research Section A: Accelerators, Spectrometers, Detectors and Associated Equipment* 824 (2016). Frontier Detectors for Frontier Physics: Proceedings of the 13th Pisa Meeting on Advanced Detectors, pp. 609–613. ISSN: 0168-9002. DOI: https://doi.org/10.1016/j.nima.2015.09.073. URL: https://www.sciencedirect.com/science/article/pii/S0168900215011286.

[107] JD Sullivan. "Geometric factor and directional response of single and multi-element particle telescopes". In: *Nuclear Instruments and methods* 95.1 (1971), pp. 5–11.

[108] S. Agostinelli et al. "Geant4—a simulation toolkit". In: *Nuclear Instruments and Methods in Physics Research Section A: Accelerators, Spectrometers, Detectors and Associated Equipment* 506.3 (2003), pp. 250–303. ISSN: 0168-9002. DOI: https://doi.org/10.1016/S0168-9002(03)01368-8. URL: https://www.sciencedirect.com/science/article/pii/S0168900203013688.

[109] "Direct detection of a break in the teraelectronvolt cosmic-ray spectrum of electrons and positrons". In: *Nature* 552.7683 (2017), pp. 63–66.

[110] T. Kobayashi et al. "The Most Likely Sources of High-Energy Cosmic-Ray Electrons in Supernova Remnants". In: *The Astrophysical Journal* 601.1 (2004), p. 340. DOI: 10.1086/380431. URL: https://doi.org/10.1086/380431.

[111] Valerio Vagelli. "Measurement of the cosmic (e++ e-) flux from 0.5 GeV to 1 TeV with the Alpha Magnetic Spectrometer (AMS-02) on the International Space Station". PhD thesis. Karlsruhe, Karlsruher Institut für Technologie (KIT), Diss., 2014, 2014.

[112] Jerzy Neyman and Egon Sharpe Pearson. "IX. On the problem of the most efficient tests of statistical hypotheses". In: *Philosophical Transactions of the Royal Society of London, Series A: Containing Papers of a Mathematical or Physical Character* 231.694-706 (Feb. 1933), pp. 289–337. ISSN: 0264-3952. DOI: 10.1098/rsta.1933.0009. eprint: https://royalsocietypublishing.org/rsta/article-pdf/231/694-706/289/240090/rsta.1933.0009.pdf. URL: https://doi.org/10.1098/rsta.1933.0009.

[113] *INFN CNAF*. URL: https://www.cnaf.infn.it/.

[114] *RECAS Bari*. URL: https://www.recas-bari.it/.

[115] E Berti et al. "CaloCube: a new concept calorimeter for the detection of high energy cosmic rays in space". In: *Journal of Physics: Conference Series* 1162 (Jan. 2019), p. 012042. DOI: 10.1088/1742-6596/1162/1/012042. URL: https://doi.org/10.1088/1742-6596/1162/1/012042.

[116] Nicola Mori. "GGS: A Generic Geant4 Simulation package for small- and medium-sized particle detection experiments". In: *Nuclear Instruments and Methods in Physics Research Section A: Accelerators, Spectrometers, Detectors and Associated Equipment* 1002 (2021), p. 165298. ISSN: 0168-9002. DOI: https://doi.org/10.1016/j.nima.2021.165298. URL: https://www.sciencedirect.com/science/article/pii/S0168900221002825.

[117] Nicola Mori. *EventAnalysis code repository*. https://baltig.infn.it/mori/EventAnalysis/.

[118] Rene Brun and Fons Rademakers. "ROOT — An object oriented data analysis framework". In: *Nuclear Instruments and Methods in Physics Research Section A: Accelerators, Spectrometers, Detectors and Associated Equipment* 389.1 (1997). New Computing Techniques in Physics Research V, pp. 81–86. ISSN: 0168-9002. DOI: https://doi.org/10.1016/S0168-9002(97)00048-X. URL: https://root.cern.ch.

[119] W. H. Furry. "On Fluctuation Phenomena in the Passage of High Energy Electrons through Lead". In: *Phys. Rev.* 52 (6 Sept. 1937), pp. 569–581. DOI: 10.1103/PhysRev.52.569. URL: https://link.aps.org/doi/10.1103/PhysRev.52.569.

[120] A. Nordsieck, W.E. Lamb, and G.E. Uhlenbeck. "On the theory of cosmic-ray showers I the furry model and the fluctuation problem". In: *Physica* 7.4 (1940), pp. 344–360. ISSN: 0031-8914. DOI: https://doi.org/10.1016/S0031-8914(40)90102-1. URL: https://www.sciencedirect.com/science/article/pii/S0031891440901021.

[121] Andrii Ilienko. "CONTINUOUS COUNTERPARTS OF POISSON AND BINOMIAL DISTRIBUTIONS AND THEIR PROPERTIES". In: *Annales Univ. Sci. Budapest.* 39.39 (2013), pp. 137–147. DOI: https://doi.org/10.1016/S0031-8914(40)90102-1. URL: https://www.sciencedirect.com/science/article/pii/S0031891440901021.

[122] GA Wilson and A Wragg. "Numerical methods for approximating continuous probability density functions using moments". In: *IMA J Appl Math* 12 (1973), pp. 165–173.

[123] G. Grindhammer and S. Peters. "The Parameterized Simulation of Electromagnetic Showers in Homogeneous and Sampling Calorimeters". In: (2000). arXiv: hep-ex/0001020 [hep-ex]. URL: https://arxiv.org/abs/hep-ex/0001020.

[124] Sergey Bochkanov. *ALGLIB*. URL: https://www.alglib.net.

[125] Paolo Lipari. "Concepts of "age" and "universality" in cosmic ray showers". In: *Phys. Rev. D* 79 (6 Mar. 2009), p. 063001. DOI: 10.1103/PhysRevD.79.063001. URL: https://link.aps.org/doi/10.1103/PhysRevD.79.063001.

[126] Zewen Li et al. "A Survey of Convolutional Neural Networks: Analysis, Applications, and Prospects". In: *IEEE Transactions on Neural Networks and Learning Systems* 33.12 (2022), pp. 6999–7019. DOI: 10.1109/TNNLS.2021.3084827.

[127] Luke de Oliveira, Benjamin Nachman, and Michela Paganini. "Electromagnetic showers beyond shower shapes". In: *Nuclear Instruments and Methods in Physics Research Section A: Accelerators, Spectrometers, Detectors and Associated Equipment* 951 (2020), p. 162879. ISSN: 0168-9002. DOI: https://doi.org/10.1016/j.nima.2019.162879. URL: https://www.sciencedirect.com/science/article/pii/S0168900219312999.

[128] Wikimedia Commons. *File:ROC curves.svg — Wikimedia Commons, the free media repository*. [Online; accessed 27-January-2026]. 2025. URL: https://commons.wikimedia.org/w/index.php?title=File:ROC_curves.svg&oldid=1004154402.